# ENHANCEMENT ON THERMOELECTRIC PROPERTIES OF Ag-DOPED $Sb_2Te_3$ THIN FILMS AS PREPARED BY MAGNETRON SPUTTERING METHOD

DISSERTATION
BY
SOMPORN THAOWANKAEW

A Dissertation Submitted in Partial Fulfillment of the Requirements for
The Doctor of Philosophy in Physics Program
at Sakon Nakhon Rajabhat University
October 2022

# ENHANCEMENT ON THERMOELECTRIC PROPERTIES OF Ag-DOPED $Sb_2Te_3$ THIN FILMS AS PREPARED BY MAGNETRON SPUTTERING METHOD

DISSERTATION

BY

SOMPORN THAOWANKAEW

A Dissertation Submitted in Partial Fulfillment of the Requirements for
The Doctor of Philosophy in Physics Program
at Sakon Nakhon Rajabhat University
October 2022

## DISSERTATION APPROVAL
## SAKON NAKHON RAJABHAT UNIVERSITY
## DOCTOR OF PHILOSOPHY
## PROGRAM IN PHYSICS

Dissertation Title: Development of Thermoelectric Efficiency of Ag Doped $Sb_2Te_3$ Thin Film as Prepared by Magnetron Sputtering Method

Author: Somporn Thaowankaew

**Dissertation Examination Committee**

| | | | |
|---|---|---|---|
| ............................................ | Chairperson | ..........Athorn.......... | Committee |
| (Prof. Dr. Santi Maensiri) | | (Asst. Prof. Dr. Athorn Vora-ud) | and Advisor |
| ............................................ | Committee | ............................................ | Committee |
| (Dr. Mati Horprathum) | and Co-Advisor | (Prof. Dr. Tosawat Seetawan) | |
| ............................................ | Committee | ............................................ | Committee |
| (Assoc. Prof. Dr. Wilawan Kumharn) | | (Asst. Prof. Dr. Hassakorn Wattanasarn) | |

| | |
|---|---|
| Approval by the Curriculum Committee | Approval by Graduate School |
| ..........Athorn.......... | ..........Surasak.......... |
| (Assist. Prof. Dr. Athorn Vora-ud) | (Asst. Prof. Dr.Surasak Santhaveesuk) |
| Chair of the Committee for Curriculum Administration Approval | The Director of Graduate School |
| Sakon Nakhon Rajabhat University | Sakon Nakhon Rajabhat University |

20 October 2022

# ACKNOWLEDGEMENTS

Firstly, I would like to acknowledge the financial support from “The Thailand Center of Excellence in Physics (ThEP) ”. My advisor and co-advisor, Assist. Prof. Dr.Athorn Vora-ud and Dr.Mati Horprathum gave the best advice and guidance for this thesis from start until successful.

I would like to also express high gratitude toward the thin film research laboratory, Center of Excellence on Alternative Energy (CEAE), Research and Development Institution, Sakon Nakhon Rajabhat University, Thailand, Opto-Electrochemical Sensing Research Team and Program of Physics, Faculty of Science and Technology, Sakon Nakhon Rajabhat University for the deposition facilities and the characterization equipment.

I would like to thank the thesis committee such as Prof. Dr.Santi Mansiri, Prof. Dr.Tosawat Seetawan, Assoc. Prof. Dr. Wilawan Kumharn, and Assist. Prof. Dr. Hassakorn Wattanasarn for their kind advice and help. My sincere appreciation to all past and Center of Excellence on Alternative Energy, Research and Development Institution & Program of Physics, Faculty of Science and Technology, Sakon Nakhon Rajabhat University, Sakon Nakhon, Thailand, for suggestions, discussions, support, and friendship. Finally, I want to thank my family support and always encouraging.

Somporn Thaowankaew

**ชื่อเรื่อง** การเพิ่มค่าสมบัติเทอร์โมอิเล็กทริกของฟิล์มบางแอนติโมนีเทลลูไรด์
เจือซิลเวอร์ที่เตรียมด้วยวิธีแมกนิตรอนสปัตเตอริง
**ผู้วิจัย** สมพร เถาวัลแก้ว
**กรรมการที่ปรึกษา** ผู้ช่วยศาสตราจารย์ ดร.อาธรณ์ วรอัด
ดร.มติ ห่อประทุม
**ปริญญา** ปร.ด. (ฟิสิกส์)
**สถาบัน** มหาวิทยาลัยราชภัฏสกลนคร
**ปีที่พิมพ์** 2565

## บทคัดย่อ

การวิจัยครั้งนี้มีวัตถุประสงค์เพื่อศึกษาการเพิ่มค่าสมบัติเทอร์โมอิเล็กทริกของฟิล์มบางแอนติโมนีเทลลูไรด์เจือด้วยซิลเวอร์ (Ag-doped $Sb_2Te_3$; AST) ผ่านการเตรียมด้วยวิธีแมกนิตรอนสปัตเตอริง (Magnetron sputtering) โดยเบื้องต้นได้ทำการเตรียมฟิล์มบางแอนติโมนีเทลลูไรด์เจือด้วยซิลเวอร์บนวัสดุฐานรองซิลิคอนไดออกไซด์ ($SiO_2$; SO) และโพลีไอไมด์ (Polyimide; PI) ด้วยวิธีแมกนิตรอนสปัตเตอริงแบบดีซี (DC magnetron sputtering) แล้วนำไปสู่กระบวนการอบให้ความร้อนอย่างรวดเร็ว (Rapid thermal anealing; RTA) ที่อุณหภูมิ 150 – 300 °C เพื่อทดสอบหาวัสดุฐานรองและอุณหภูมิการอบที่เหมาะสมในการเตรียมฟิล์มบาง การตรวจสอบความเป็นผลึก ลักษณะสัณฐานวิทยา องค์ประกอบเชิงธาตุ และสมบัติทางเทอร์โมอิเล็กทริกของฟิล์มบางที่เตรียมได้ พบว่า ฟิล์มบางที่เตรียมบน $SiO_2$ แสดงค่าความเป็นผลึกที่สูงและมีค่าตัวแปรกำลัง (power factor) สูงกว่าเมื่อเปรียบเทียบกับฟิล์มบางที่เตรียมบนโพลีไอไมด์ โดยที่อุณหภูมิห้องมีค่าตัวแปรกำลังสูงสุดเป็น 3.95 mW $m^{-1}$ $K^{-2}$ และ 0.53 mW $m^{-1}$ $K^{-2}$ สำหรับฟิล์มบางที่เตรียมบน $SiO_2$ และโพลีไอไมด์ตามลำดับที่ผ่านการอบที่อุณหภูมิ 250 °C

จากนั้นจึงได้ใช้วัสดุฐานรอง SO ในการเตรียมฟิล์มบาง AST ด้วยวิธีแมกนิตรอนสปัตเตอริงแบบอาร์เอฟ (RF magnetron sputtering) โดยปรับเปลี่ยนเงื่อนไขกำลังไฟฟ้าของระบบอาร์เอฟสำหรับการพอกพูนฟิล์มบางเป็น 30, 50, 70 และ 90 W ภายใต้การหมุนของวัสดุฐานรองที่ความเร็ว 20, 40, 60 และ 80 rpm นำไปสู่กระบวนการอบให้ความร้อนที่อุณหภูมิ 250 °C ผลการศึกษาสมบัติเทอร์โมอิเล็กทริกของฟิล์มบางที่เตรียมได้ พบว่า ฟิล์มบางที่พอกพูนด้วยเงื่อนไขกำลังกำลังไฟฟ้า 50 W และความเร็วการ

หมุนของวัสดุฐานรอง 60 rpm มีค่าตัวแปรกำลังสูงสุดเป็น 5.93 mW m$^{-1}$K$^{-2}$ และ 12.13 mW m$^{-1}$ K$^{-2}$ สำหรับที่อุณหภูมิห้องและที่ 100 °C ตามลำดับ

ลำดับสุดท้าย การประดิษฐ์เครื่องกำเนิดไฟฟ้าเทอร์โมอิเล็กทริกฟิล์มบางบนวัสดุฐานรอง SO และ PI ขนาด 20 × 20 mm$^2$ โดยใช้วัสดุฟิล์มบางชนิดพีเป็น AST และวัสดุฟิล์มบางชนิดเอ็นเป็น บิสมัทเทลลูไลด์ ($Bi_2Te_3$; BT) จำนวน 5 คู่ ผ่านวิธีแมกนิตรอนสปัตเตอริงแบบอาร์เอฟและอุณหภูมิการอบที่ 250 °C การทดสอบค่าการผลิตไฟฟ้าประกอบด้วย แรงดันไฟฟ้าวงจรเปิด กระแสไฟฟ้า และกำลังไฟฟ้าที่อุณหภูมิห้องถึง 100°C พบว่า เครื่องกำเนิดไฟฟ้าเทอร์โมอิเล็กทริกฟิล์มบางบนวัสดุฐานรอง SO มีค่ากำลังไฟฟ้าสุดเป็น 1.9 μW ที่ผลต่างอุณหภูมิสูงสุด 19.99°C มี ขณะที่เครื่องกำเนิดไฟฟ้าเทอร์โมอิเล็กทริกฟิล์มบางบนวัสดุฐานรอง PI มีค่ากำลังไฟฟ้าสุดเป็น 23.06 μW ที่ผลต่างอุณหภูมิสูงสุด 80.05°C

**คำสำคัญ:** เทอร์โมอิเล็กทริกฟิล์มบาง ฟิล์มบางแอนติโมนีเทลลูไลด์เจือด้วยซิลเวอร์ แมกนิตรอนสปัตเตอริง การอบให้ความร้อนอย่างรวดเร็ว

**TITLE** Enhancement on Thermoelectric Properties of Ag-doped $Sb_2Te_3$ Thin Films as Prepared by Magnetron Sputtering Method
**AUTHOR** Somporn Thaowankaew
**ADVISORS** Assist. Prof. Dr.Athorn Vora-ud
Dr.Mati Horprathum
**DEGREE** Ph.D. (Physics)
**INSTITUTION** Sakon Nakhon Rajabhat University
**YEAR** 2022

# ABSTRACT

This research aims to enhance the thermoelectric properties of Ag-doped $Sb_2Te_3$ (AST) thin films as prepared through a magnetron sputtering method. Firstly, AST thin films were synthesized by a direct current (DC) magnetron sputtering method onto $SiO_2$ (SO) and polyimide (PI) substrates into rapid thermal annealing (RTA) process at temperature 150-300°C to be selected the substrate and RTA temperature optimization for thin film preparation. The crystallinity, morphology, composition, and thermoelectric properties of thin films were investigated. It was found that the thin films, as prepared onto SO substrates yielded higher crystallinity and eventually a higher power factor compared to those grown on the PI substrates. At room temperature, the maximum power factor was 3.95 mW $m^{-1}$ $K^{-2}$ and 0.53 mW $m^{-1}$ $K^{-2}$ for the thin films prepared onto SO and PI substrates, respectively, at an annealed temperature of 250°C.

After that, SO substrates were used to prepare AST thin film by radio frequency (RF) magnetron sputtering method. The deposition condition is used for the sputtering RF power variation of 30, 50, 70, and 90 W within the substrate holder rotations speed of 20, 40, 60, and 80 rpm into the RTA process at a temperature of 250°C. As a result, the AST thin film, as prepared by RF power of 50 W and the substrate rotation speed of 60 rpm, has a maximum power factor of 5.93 mW $m^{-1}$ $K^{-2}$ and 12.13 mW $m^{-1}$ $K^{-2}$ for room temperature and 100°C, respectively.

Finally, thin film thermoelectric generators were fabricated onto SO and PI substrates of size 20 x 20 mm$^2$ using the p-type AST thin films and n-type $Bi_2Te_3$ (BT) thin films within five couples through RF magnetron sputtering and annealed at a temperature of 250°C. The electrical generation testing was composed of open circuit voltage, electrical current, and electrical power output as measured at room temperature to 100°C. It was found that the thin film thermoelectric generator onto the SO substrate has a maximum electrical power of 1.9 μW at the maximum temperature difference of 19.99°C. In comparison, the thin film thermoelectric generators onto the PI substrate have a maximum electrical power of 23.06 μW and a maximum temperature difference of 80.05°C.

**Keywords:** Thermoelectric thin film, Ag-doped $Sb_2Te_3$ thin film, magnetron sputtering, rapid thermal annealing

# TABLE OF CONTENTS

**CHAPTER** **Page**

## TABLE OF CONTENTS (continued)

**CHAPTER** **Page**

## TABLE OF CONTENTS (continued)

**CHAPTER** **Page**

# LIST OF TABLES

## LIST OF FIGURES

## LIST OF FIGURES (continued)

## LIST OF FIGURES (continued)

# LIST OF FIGURES (continued)

**Figure** **Page**

## LIST OF FIGURES (continued)

**Figure** **Page**

# CHAPTER 1

# INTRODUCTION

The introduction of this research is composed of the topic of motivation, research objectives, scope, limitations, and finally anticipated outcomes of the dissertation.

## MOTIVATION

Over the past few decades, thermoelectric power materials have been extensively investigated both theoretically and experimentally as a promising technology for resolving contemporary energy and environmental issues (Harman, T.C., et al., 2002; Venkatasubramanian, R., et al., 2001; Huang, B. and Kaviany, M, 2010; Kim, H., et al., 2010; Harman, T. C., et al, 2005; Shakouri, A. 2006). Thermoelectric devices are able to generate electricity from heat, or conversely, generate heat from electricity, and thus have great potential for advancing waste heat recovery and cooling field (Rowe, D. M. 2005; Heremans, J. P., et al., 2008; Price, S. H. 2007). The performance of thermoelectric devices is related to the dimensionless thermoelectric figure of merit, $ZT$ values, determined by the Seebeck coefficient (S), electrical conductivity ( $\sigma$ ), and thermal conductivity ( $\kappa$ ) as

$$ZT = \frac{S^2\sigma}{\kappa} \tag{1}$$

where $S^2\sigma$ is defined as power factor (PF), and $\kappa$ includes electronic thermal conductivity $\kappa_{ele}$ and lattice thermal conductivity $\kappa_{lat}$ $\kappa = \kappa_{ele} + \kappa_{lat}$ (Bell, L. E. (2008; Denmark, T. U. o., 2014)

The growing demand for micro-scale energy harvesting for the power supply or miniaturized sensors has prompted researchers to look into multifunctional flexible thermoelectric devices, which offer numerous benefits such as flexibility, small volume, lightweight, high integration, and enhanced compatibility. ( Kim, S. J., 2017; Energy.com, C., 2013) Flexible materials and their flexible generators, including inorganic and organic based materials, have already been pursued using various methods (Kim, S. J.,2016; Tian, R., 2017)

In accordance with Vieira, (2019) Improved thermoelectric properties of p-$Sb_2Te_3$ and n-$Bi_2Te_3$ films deposited by thermal co-evaporation at 503 K and 543 K, respectively, are reported, by using two types of substrates (borosilicate glass and 25 μm – Kapton® polyimide). Seebeck coefficients of 194 $\mu V\ K^{-1}$ and – 233 $\mu V\ K^{-1}$ and electrical conductivities of $3.2 \times 10^4\ \Omega$ m and $5 \times 10^4 \Omega$ m, lead to optimized power factors of $1.2 \times 10^{-3}\ W\ K^{-2}\ m^{-1}$ and $2.7 \times 10^{-3}\ W\ K^{-2}\ m^{-1}$, measured at 298 K, for flexible $Sb_2Te_3$ and $Bi_2Te_3$ films, respectively. The power factor value increases until a maximum of $2.3 \times 10^{-3}\ W\ m^{-1}\ K^{-2}$ for the p-type film and to 5.9 × 10-3 $W\ m^{-1}\ K^{-2}$ for the n-type film, at 373 K, respectively (Vieira et al., (2019). However Adam et al., (2021) composition-dependent electrical properties of ternary Bi-doped $Sb_2Te_3$ thin films synthesized by vacuum thermal evaporation technique on ceramic substrates, were found to have Seebeck coefficient and power factor equaling 0.32 μV/K and 227.6 $\mu W/m.K^{-2}$ respectively (Adam, A. M. et al., 2019) and has developed thin film thermoelectric module with karthikeyan. et al., (2020) Developing a thermoelectric generator Intact thin films of p-SnTe/n-PbTe deposited on flexible substrate through physical vapor deposition. Thermoelectric performance of the deposited thin film exhibits maximum ZT of ~0.3 (p-type) and ~0.2 (n-type) at 550 K. From the fabricated TEGs, maximum output voltage and power density of 250 mV and 8.4 $mW/cm^2$ at a temperature difference of 120 °C (Karthikeyan, V., et al, 2020).

This research is interesting in the synthesis of Ag-doped $Sb_2Te_3$ thin film coating using DC and RF-magnetron sputtering methods. After that, we investigated the crystal structure, microstructural, composition, and thermoelectric properties of thin films after annealing and fabricating the thin film's thermoelectric generator prototype.

## RESEARCH OBJECTIVES

1. To study Ag-doped $Sb_2Te_3$ (AST) thin films deposition conditions as synthesized onto $SiO_2$ (SO) and Polyimide (PI) substrates by DC magnetron sputtering method to characterizations and thermoelectric properties measurement of thin films.

2. To enhance of thermoelectric properties of AST thin films as synthesized onto SO substrates by RF magnetron sputtering method within the substrate rotations.

3. To fabrication and power generation measurement of thin film thermoelectric (TFTE) modules based on *p*-AST matched with $Bi_2Te_3$ (*n*-BT).

## SCOPE AND LIMITATION OF THE THESIS

1. AST thin films are deposited onto SO and PI substrate by DC magnetron sputtering method from a 99.99% purity of $AgSbTe_2$ target with 76.2 mm of diameters and 3 mm thick. The deposition condition is used for the sputtering DC power variation of 30, 50, 70, and 90 W for 30 min at ambient temperature. As-deposited thin films are annealed by a rapid thermal annealing process at a temperature range of 100-300 °C. After the annealing process, the crystal structure, surface morphology, and chemical composition of the annealed thin film were observed by XRD (XRD-6100, SHIMUDZU), FE-SEM, and EDX, respectively. Thermoelectric properties (Seebeck coefficient and electrical resistivity) of the annealed thin film were measured by using ZEM-3 method to be calculated the power factor.

2. AST thin films are deposited onto SO substrate by RF magnetron sputtering method. The deposition condition is used for the sputtering RF power variation of 30, 50, 70, and 90 W within the substrate holder rotations speed of 20, 40, 60, 80 rpm. After the annealing process, the crystal structure, surface

morphology, chemical composition, and thermoelectric properties of the annealed thin film were observed and measured to be compared with the thin films as synthesized by the DC magnetron sputtering method.

3. TFTE modules are fabricated by RF-magnetron sputtering method using *p*-type AST (*p*-AST) and *n*-type $Bi_2Te_3$ (*n*-BT) targets. Five couples of p-n junction arrays were deposited onto SO and PI substrates size 20 x 20 $mm^2$. The electrical power generations of TFTE modules composed of electrical voltage, electrical current, and electrical power output were measured under the temperature difference of 75°C at the ambient temperature of 100°C.

## ANTICIPATED OUTCOMES OF THE THESIS

1. Thermoelectric properties of Ag-doped $Sb_2Te_3$ Thin Films could be enhanced by the RF magnetron sputtering method within the substrate rotations.
2. New prototypes of thin film thermoelectric modules within *p-n* junctions.
3. International paper publications.

# CHAPTER 2

# THEORY AND LITERATURE REVIEWS

This chapter is overview background of the thermoelectric effect, thermoelectric performance, functions of thermoelectric effects, optimizing the figure of merit (ZT), and thermoelectric parameters presented the three thermoelectric effects which are the Seebeck effect, Peltier effect, and Thomson effect. Section of key differences between nanomaterials and bulk materials and compatibility and efficiency ratio of oxide thermoelectric materials. Section magnetron sputtering and reviews the history and section of current research of thermoelectric of $p$-$Sb_2Te_3$ materials. Lase section of thermoelectric generators presents the energy conversion efficiency of thin film thermoelectric modules and an overview of the thin film thermoelectric generator and their relevant fabrication techniques.

## PRINCIPLE OF THERMOELECTRIC

### Thermoelectric Effects

The thermoelectric effect is the direct conversion of temperature differences to electric voltage and vice versa via a thermocouple. (Price, S. H., 2007) A thermoelectric device creates a voltage when there is a different temperature on each side. Conversely, when a voltage is applied to it, heat is transferred from one side to the other, creating a temperature difference. At the atomic scale, an applied temperature gradient causes charge carriers in the material to diffuse from the hot side to the cold side. The term "thermoelectric effect" encompasses three separately identified effects: the Seebeck effect, the Peltier effect, and the Thomson effect. The Seebeck and Peltier effects are different manifestations of the same physical process;

textbooks may refer to this process as the Peltier–Seebeck effect. The Thomson effect is an extension of the Peltier–Seebeck model and is credited to Lord Kelvin.

### Seebeck Effect

In 1821, Thomas Johann Seebeck, a German–Estonian physicist, found that a voltage existed between two ends of a metal bar when a temperature difference $\Delta T$ existed in the bar (see Figure 1(a)). This effect is the conversion of temperature differences directly into electricity, which is called the Seebeck effect. Seebeck also discovered that a compass needle would be deflected when a closed loop was formed of two metals with a temperature difference between the junctions (see Figure 1(b)). This is because the metals respond differently to the temperature difference, which creates a current loop. When a steady temperature gradient is maintained along the bar of the thermoelectric material, the free charge carriers at the hot end will have high kinetic energy and tend to diffuse to the cold end. The accumulation of the charges at the cold results in a back electromotive force (EMF) which opposes a further flow of charge. The EMF is called the Seebeck emf or Seebeck voltage, which is the open circuit voltage when no current flows (Seetawan, et al., 2006, pp. 314–317; Somkhunthot, et al., 2007, pp. 20–26).

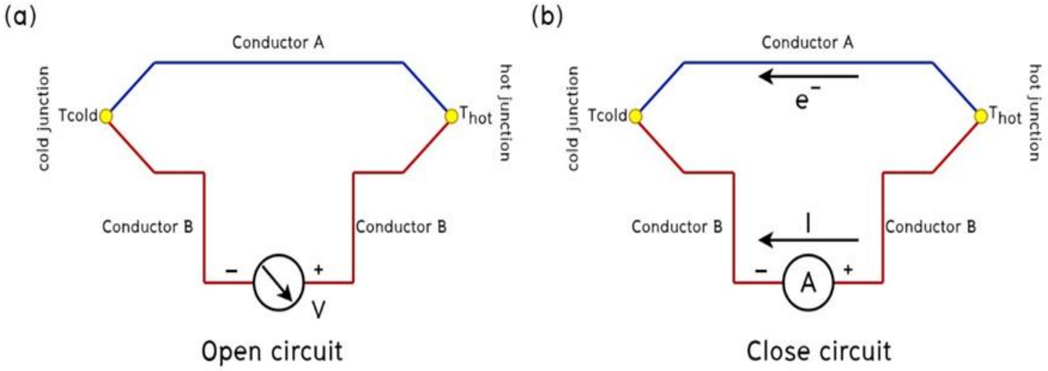

Figure 1 Schematic illustration of the Seebeck effect circuit between two dissimilar materials with junctions held at different temperatures (Rowe, 2005).

From Figure 1, if the temperature difference between the two ends of a material is small, and the thermoelectric voltage is seen at the terminals. Then the

Seebeck coefficient, or thermoelectric power, or thermopower of a material is defined as (Rowe, 2005):

$$S = \frac{\Delta V}{\Delta T} \tag{1}$$

If the junctions of the metals A and B were maintained at two different temperatures $T_H$ and $T_C$ , where $T_H > T_C$ , the potential difference $\Delta V$ developed can be derived from:

$$\Delta V = \int_{T_C}^{T_H} \left[S_B(T) - S_A(T)\right] dT \tag{3}$$

where $S_A$ and $S_B$ are the absolute Seebeck coefficients of the metals A and B, respectively. The Seebeck coefficients are non-linear, and depend on the conductors' absolute temperature, material, and molecular structure. It has a unit of V/K. If the Seebeck coefficients are effectively constant for the measured temperature range, Equation (5) can be approximated as:

$$\Delta V = (S_B - S_A) \cdot (T_H - T_C) \tag{4}$$

### Peltier effect

The Peltier effect was observed in 1834 by Jean Charles Athanase Peltier, 13 years after Seebeck's initial discovery. This effect is the reverse of the Seebeck effect; an electrical current would produce a temperature gradient at the junctions of two dissimilar metals or semiconductors (n-type and p-type).

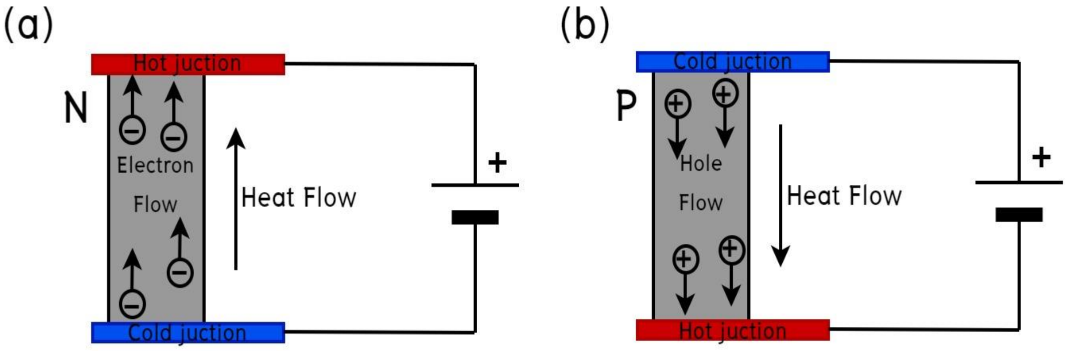

Figure 2 (a) The n-type semiconductor is biased externally creating an electrical current. The negative carriers (electrons) carry heat from bottom to top via the Peltier effect. (b) The positive carriers (holes) within a p-type semiconductor-biased in the same direction as (a) pump heat in the opposite direction, that is, from top to bottom.

Consider the Peltier effect circuit in Figure 2, when applying a voltage, a current *I* will flow through the circuit. In the case of an n-type semiconductor, high-energy electrons moved from the negative end to the positive end as shown in Figure 2(a). As a result, the thermal current and the electric current are in opposite directions. Consequently, the junction connected to the positive terminal of the power supply will be heated up, while that connected to the negative terminal will be cooled down. The situation is opposite in the p-type as shown in Figure 2.2(b), the applied voltage causes holes to move from the positive end to the negative end. The thermal current and electric current are therefore in the same direction. In either case, the thermal current density $Q$ is proportional to the electrical current density field $J$ :

$$Q = \Pi_{ab} \cdot J \tag{5}$$

where $\Pi$ is the Peltier coefficient which represents how much heat current is carried per unit charge through a given material.

### Thomson effect

When the electrical current density passes through a homogeneous conductor having a temperature gradient over its length, heat will be either emitted from or absorbed by the conductor. This phenomenon is well known as the Thomson effect which is dependent on the direction of both the electrical current density and temperature gradient as shown in Figure 3. (Rowe, 2005).

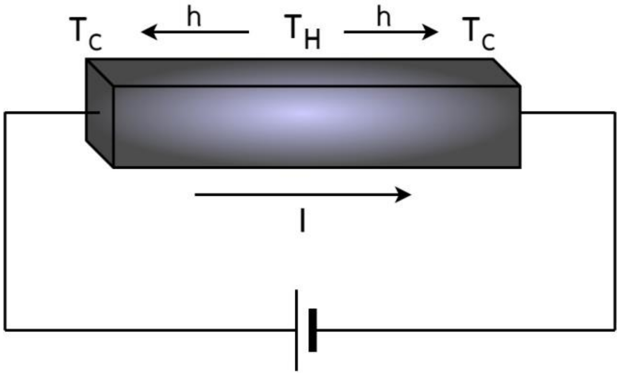

Figure 3 Schematic diagram of Thomson effect (Rowe, 2005).

William Thomson (Lord Kelvin) was a Scottish mathematical physicist and engineer who described the heating or cooling of an electric current-carrying conductor, the ends of which are maintained at different temperatures. He found that an extra amount of heat is evolved at a rate approximately proportional to the product of the current, and a temperature gradient, in addition to the well-known joule heat. This can be given by the relation:

$$q = \rho J^2 - \mu J \frac{dT}{dx} \tag{6}$$

where $q$ is heat production per unit volume, $\rho$ is the resistivity of the material, $J$ is the electric current density, $\mu$ is the Thomson coefficient in volts per Kelvin, and $dT/dx$ is the temperature gradient along the wire. The first term $\rho J^2$ is simply Joule heating which is not reversible. While the second term $\mu J(dT/dx)$ is the Thomson heat which changes sign when changes direction of $J$.

In 1854, Thomson found two relationships called the Thomson and Kelvin relationships. The first Thomson relation is related to the $\Pi$ , $S$ , and $T$ :

$$\Pi = S \cdot T \tag{7}$$

The second Thomson relation is related to the $\mu$ , $S$ and $T$ :

$$\mu = T\frac{dS}{dT} \text{ or } S = \int \frac{\mu}{T} dT \tag{8}$$

## FUNCTIONS OF THERMOELECTRIC EFFECTS

The most popular and classic TE application is a thermocouple. The power generation from the heat of the TE cell is based on the Seebeck phenomenon.
The thermoelectric cell is fabricated from two types of thermoelectric materials (p-type and n-type). In most semiconductor materials as the electrode is connected serially called a p-n junction. In other words when heating at the p-n junction of the thermoelectric cell. The heat that flows through it varies by the type of thermoelectric material, which results in temperature differences and potential voltages between the two electrodes. It is caused by the flow of electrons and holes. And at the same time, it absorbs heat from the other side of the thermoelectric material to cool it to the other end of the thermoelectric material. The hole flow of thermoelectric material is in the opposite direction to the flow of electrons, that is when we heat it to the p-n junction. The flow of electrons and holes from the hot side to the cold side or the thermal absorption of the positive charge of the p-type material and then dissipate of the n-type material as shown in Figure 4.

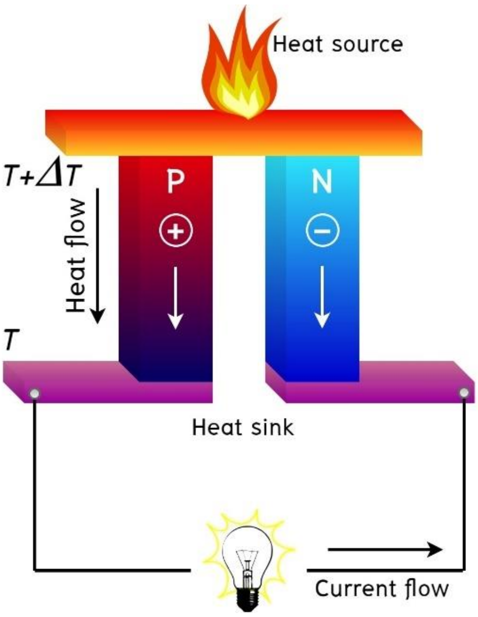

Figure 4 Seebeck effect for the power generation, an applied temperature difference causes charge carriers in the material (electrons or holes) to diffuse from the hot side to the cold side, resulting in current flow through the circuit.

The Peltier coefficients represent how much heat is carried per unit charge. Since charge current must be continuous across a junction, the associated heat flow will develop a discontinuity if $\Pi_A$ and $\Pi_B$ are different. The Peltier effect can be considered as the back-action counterpart to the Seebeck effect (analogous to the back-emf in magnetic induction): if a simple thermoelectric circuit is closed, then the Seebeck effect will drive a current, which in turn (by the Peltier effect) will always transfer heat from the hot to the cold junction (Skripnik & Khimicheva, 1997, pp. 673-677). The close relationship between Peltier and Seebeck effects can be seen in the direct connection between their coefficients: $\Pi = TS$. A typical Peltier heat pump involves multiple junctions in series, through which a current is driven. Some of the junctions lose heat due to the Peltier effect, while others gain heat. Thermoelectric heat pumps exploit this phenomenon, as do thermoelectric cooling devices found in refrigerators as shown in Figure 5.

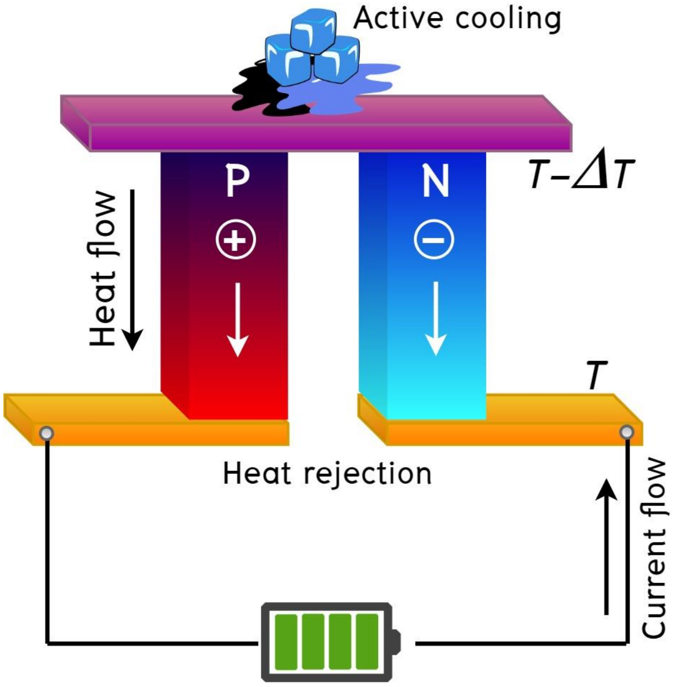

Figure 5 Peltier effect for the active refrigeration, heat evolves at the upper junction and is absorbed in the lower junction when a current is made to flow through the circuit.

## OPTIMIZING THE FIGURE OF MERIT, ZT, AND THERMOELECTRIC PARAMETERS

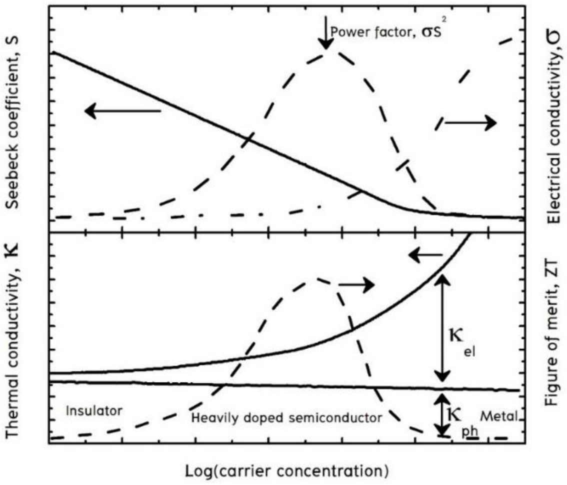

Figure 6 Variation of the transport coefficients as a function of the carrier concentration.

Figure 6 As previously stated optimizing ZT, one of the parameters used in the classification of materials is electrical conductivity. Metals have high electrical conductivity, while insulators have very low conductivity which under normal conditions is taken as zero. Semiconductors occupy an intermediate position between the two. Electrical conductivity reflects the charge carrier concentration. All three parameters which occur in the Figure of merit are functions of carrier concentration (Spies, et al., 2015). Electrical conductivity increases with an increase in carrier concentration, while the Seebeck coefficient decreases, and the electrical power factor maximizes at a carrier concentration of around $10^{25}$ $cm^{-1}$. The electronic contribution to the thermal conductivity field field $\kappa_e$ , which in thermoelectric materials is generally around 1/3 of the total thermal conductivity, also increases with carrier concentration. The Figure of Merit optimizes at carrier concentrations that correspond to semiconductor materials. Consequently, semiconductors are the materials most researched for thermoelectric applications.

## THERMOELECTRIC PARAMETER

Thermoelectric materials harvesting energy by converting waste heat into electricity through different temperatures between thermoelectric devices; this method is an attractive method to reduce greenhouse gas emissions (Enescu, 2019). Thermoelectric devices can convert heat into electricity or transport heat-producing cooling using the Seebeck and Peltier effects. The efficiency of the process typically determines the utility and cost of such devices and even the power density (Snyder, et al., 2017, pp. 2280-2283). This performance of thermoelectric materials can be predicted via consideration of the dimensionless Figure of merit (ZT).

$$ZT = \frac{S^2 T}{\rho\kappa} \tag{2.8}$$

where *S* is the Seebeck coefficient (V/K), *T* is the absolute temperature, $\rho$ is the electrical resistivity ($\Omega$ m) and $\kappa$ is the thermal conductivity (W/mK). The Figure of merit $ZT(T)$ is, in general, a temperature-dependent material property derived from temperature-dependent material properties $S(T), \rho(T)$, and $\kappa(T)$. An efficient thermoelectric generator, however, must operate across a finite temperature difference $\Delta T = T_h - T_c$ so that these material properties will change from the hot to the cold end. The relationships of $S, \rho$ and $\kappa$ are the most important factors leading to high or low ZT values of thermoelectric materials with a drastic dependence on carrier concentration, the electrical and thermal conductivity increase, while the Seebeck coefficient decreases with increasing carrier concentration

### Seebeck coefficient

One way to define the Seebeck coefficient is the voltage built up when a small temperature gradient is applied to a material, and when the material has come to a steady state where the current density is zero everywhere. If the temperature difference $\Delta T$ between the two ends of a material is small, then the Seebeck coefficient of a material is defined as:

$$S = -\frac{\Delta V}{\Delta T} \tag{10}$$

where $\Delta V$ is the thermoelectric voltage seen at the terminals. (See below for more on the signs of $\Delta V$ and $\Delta T$ )

Note that the voltage shift expressed by the Seebeck effect cannot be measured directly, since the measured voltage (by attaching a voltmeter) contains an additional voltage contribution, due to the temperature gradient and Seebeck effect in the measurement leads. The voltmeter voltage is always dependent on relative Seebeck coefficients among the various materials involved. Eq. 13 By utilizing thermodynamics of irreversible processes, the Seebeck coefficient can be expressed as (Hilaal Alama, 2012, pp. 190-212):

$$S = \frac{8\pi^2 k_B^2}{3eh^2} m * T \left(\frac{\pi}{3n}\right)^{\frac{3}{2}} \tag{11}$$

where $k_B$ is the Boltzmann constant, $e$ is the electron charge, $h$ is Planck's constant, $m^*$ is the effective carrier mass, $T$ is the absolute temperature and n is charge carrier concentration. Assuming that $S$ is measured at a constant temperature, the only variable in this equation will be carrier concentration $n$ that can be varied through doping. By looking at the equation we can see that $S$ will decrease when the $n$ increases. The reason for this is the fact that the Seebeck effect is caused by the induced voltage in the material. The higher the carrier concentration to begin with the lower the induced voltage as it takes fewer new electron-hole pairs to induce current flow through the material.

### Electrical resistivity

In general, intrinsic semiconductor resistivity decreases with increasing temperature. The electrons are bumped to the conduction energy band by thermal energy, where they flow freely, and in doing so leave behind holes in the valence band, which also flow freely (Lowrie, & Fichtner, 2020).

The electric resistance of a typical intrinsic (undoped) semiconductor decreases exponentially with temperature:

$$\rho = \rho_0 e^{-aT} \tag{12}$$

An even better approximation of the temperature dependence of the resistivity of a semiconductor is given by the Steinhart–Hart equation (Seymour, 1972, pp. 53–54 34):

$$\frac{1}{T} = A + B\text{In}\rho + C\left(\text{In}\rho\right)^3 \tag{13}$$

where $A, B$ and $C$ are the so-called **Steinhart–Hart coefficients**.

Extrinsic (doped) semiconductors have a far more complicated temperature profile. As temperature increases starting from absolute zero, they first decrease steeply in resistance as the carriers leave the donors or acceptors. After most of the donors or acceptors have lost their carriers, the resistance starts to increase again slightly due to the reduced mobility of carriers (much as in a metal). At higher temperatures, they behave like intrinsic semiconductors as the carriers from the donors/acceptors become insignificant compared to the thermally generated carriers (Smith, 1972, p. 78).

In non-crystalline semiconductors, conduction can occur by charges quantum tunneling from one localized site to another (öer, & Pohl, 2017, pp. 1053-1087; Kabir, et al., 2014, pp. 7522–7528). This is known as variable range hopping and has the characteristic form of

$$\rho = A\exp\left(T^{-\frac{1}{n}}\right), \tag{14}$$

where $n$ = 2, 3, 4, depending on the dimensionality of the system.

A normal of semiconductor exhibits a thermally activated electrical resistivity $(\rho)$ that decreases with increasing temperature. Metals have very low electrical resistivity, typically above 5 × $10^{-4}$ Ωcm which increases as the temperature increases. However, non-degenerate semiconductors exhibit a resistivity that decreases with temperature, but the magnitude is much high than for metal, and typically in the range of $10^{-4}$ to $10^{-5}$ Ωcm depending on the band gap. Insulators have resistivity of less than $10^{7}$ Ωcm.

### Thermal Conductivity

The **thermal conductivity** of a material is a measure of its ability to conduct heat. It is commonly denoted by $k, \lambda,$ or $\kappa$

Heat transfer occurs at a lower rate in materials of low thermal conductivity than in materials of high thermal conductivity. For instance, metals typically have high thermal conductivity and are very efficient at conducting heat, while the opposite is true for insulating materials. Correspondingly, materials of high thermal conductivity are widely used in heat sink applications, and materials of low thermal conductivity are used as thermal insulation. The reciprocal of thermal conductivity is called thermal resistivity. The thermal conductivity of materials is mainly the sum of two components: the lattice (phonon) component, $\kappa_{ph}$ , and the electronic component, $\kappa_e$ . As a result, the total thermal conductivity, $\kappa_{tot}$ is defined as a sum of the electronic and lattice component.

$$\kappa = \kappa_e + \kappa_{ph} \tag{15}$$

Therefore, in semiconducting materials, a finite maximum of the thermoelectric power factor is achieved. As a result, the most effective way to enhance the thermoelectric figure of merit of bulk materials is to decrease the lattice contribution to thermal conductivity . However, thermal conductivity reduction, without decreasing the power factor, was not possible for a long time (in all efforts up to the 1990s), and the ZT values were limited to unity. This translates to low conversion efficiencies and limited applications for thermoelectricity.

The electrical thermal conductivity can be expressed as:

$$\kappa_e = \frac{LT}{\rho} \tag{16}$$

This contribution, due to electrons or holes that carry heat in the system, is insignificant at very low doping levels but becomes more important as the number of charge carriers increases. The electronic participation of the thermal conductivity is given by the Wiedemann–Franz law as a function of the electrical resistivity $\rho$, the absolute temperature, $T$, and the Lorentz number, L = 2.4453 • $10^{-8}$ W$\Omega$/$K^2$. Another illustrative equation is the Wiedemann–Franz relationship s (Bhaskar, A., Liu, C.-J., Yuan, J. J., & Chang, C.-L., 2013, pp. 236–239):

$$\kappa_e = \left(\frac{k_B}{e}\right)^2 \frac{LT}{\rho} \tag{17}$$

where e is a charge of an electron and $k_B$ is Boltzmann's constant.

### The lattice thermal conductivity

Lattice vibrations are independent of the carrier concentration the lattice thermal conductivity increases rapidly and becomes less significant in materials with high carrier concentration because the electronic thermal conductivity is the dominating process (Sootsman, Chung, & Kanatzidis, 2009, pp. 8616–8639).

$$\kappa_{ph} = \frac{1}{3} C_V v l_{ph} \tag{18}$$

where $C_V$ is the heat capacity at constant volume, $V$ is the concentration and velocity of phonons and $l_{ph}$ is the phonon mean free path, which is defined as the average distance a phonon travels before colliding with another particle. The evolution of the $\kappa_{ph}$ with the temperature depends on the dominating interactions occurring in the lattice. At low temperatures those limitations are caused by the grain size and the defect concentration while at high temperatures, collisions between phonons are the dominant factor limiting heat conduction.

## ENHANCEMENT OF ZT WITH NANOMATERIALS

The Nanostructuring of materials is a key topic in many of today's research fields. Popular techniques to produce nanometric structures can be classified as top-down strategies or bottom-up growth mechanisms. Self-assembled and self-organized structures are important owing to the elementary fabrication processes. A special interest exists in the changing properties of the material due to the nanoscopic size compared with bulk materials. Because of these emerging new properties, nanostructured materials and especially semiconductors are of paramount importance.

The idea of nano-engineering the materials to enhance their thermoelectric properties began when scientists predicted that the introduction of defects at the nano level could interrupt the flow of phonons by selective-site scattering i.e. quantum dots and wire, which resulted in a decrease in thermal conductivity and lead to a higher figure of merit (Harman, et al., 2002, pp. 2229-2232). Furthermore, not only dispersed defects but also a layer of thin film or a specific array of nanowires could be coated onto the thermoelectric material which could potentially alter its electronic state e.g. Fermi energy level, etc., and lead to more favorable electrical characteristics (Böttner, Chen, & Venkatasubramanian, 2006, pp. 211-217). Research literature suggests that nanomaterials have increased the figure of merit several folds (Dresselhaus, et al., 2007, 1043-1053; Shakouri & Zebarjadi, 2009, pp. 225-299). The concept of nano-materials has been widely used in thin film thermoelectric materials and some quantum dots (Böttner, et al., 2006; Harman, et al., 2002, pp. 2229-2232) (Minnich, et al., 2009, pp. 466-479; Shakouri & Zebarjadi, 2009, pp. 225-299).

## PHONON SCATTERING

Phonon scattering is a phenomenon where the phonon means the free path through a material has been reduced; several factors can contribute to this effect.

In the development of thermoelectric materials, there is a trade-off between the electrical and thermal conductivity Fields (Chen, 2001, p. 23). Phonon scattering has therefore become four key methods to reduce thermal conductivity without reducing electrical conductivity and increasing phonon scattering in crystalline materials. Doping a material with elements to introduce lattice misfit and strain that increases phonon scattering without significant degradation of electrical conductivity. It also alters the band structure and electron mobility which might be favorable to the thermoelectric properties (Ioffe, 1957). A second method to achieve phonon scattering is via ‘rattling’ crystal structures, where the crystal structure is engineered such that a dopant atom is surrounded by a ‘cage’ of atoms. The dopant-and cage atoms will have different vibrational frequencies at a given temperature leading to the scattering of the phonons (Trigo, Bruchhausen, Fainstein, Jusserand, & Thierry-Mieg, 2002, p. 227402).

## OVERVIEW OF THIN FILM DEPOSITION

Physical deposition methods of thin films are shown in Figure. 7. The deposition methods are composed of the PVD process, the CVD process, and the chemical solvent deposition including sol-gel deposition. The PVD process is divided into two categories: (1) thermal evaporation and (2) sputtering. Several publications have presented a detailed review of thin film deposition processes. (Holland, et al., 1970; Maissel, et al., 1971; H Adachi, et al., 2012; Hass, G., et al., 2013; Bunshah, R. F., et al., 1982; Rossnagel, S. M., et al., 1990; Elshabini, A., et al., 1998) Brief descriptions of the PVD and CVD process are presented in this section.

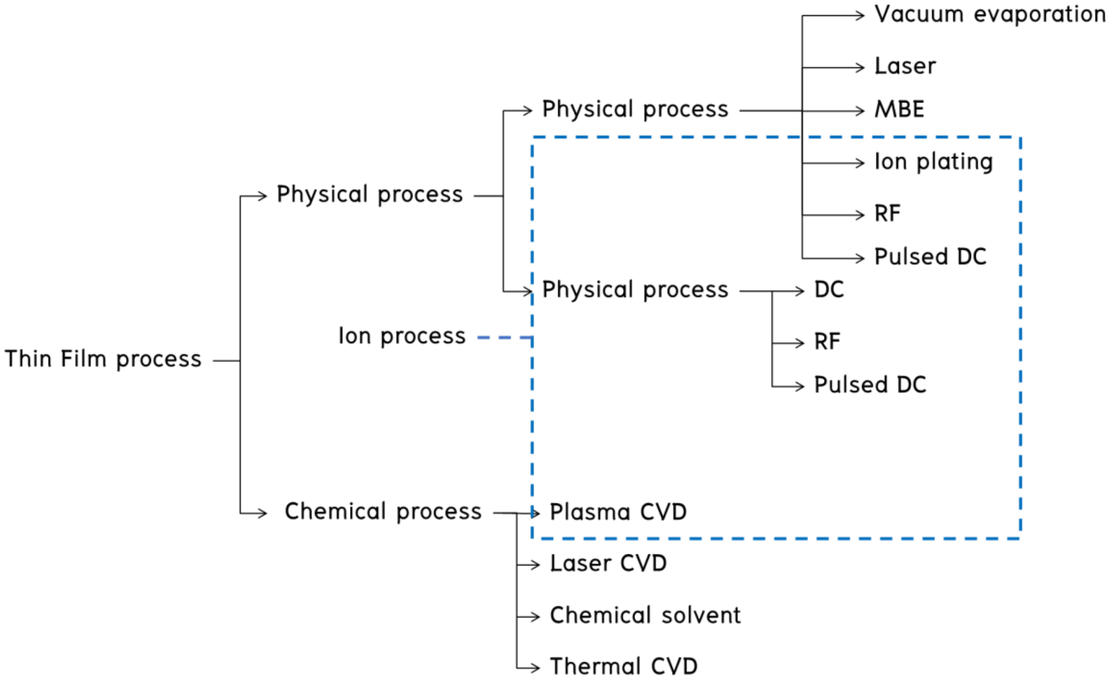

Figure 7 Typical deposition methods of thin films. (Hayakawa, S., 1992)

Nowadays, many methods can be used to deposit films including thermal evaporation (Paine, et al., 1999), sputtering deposition (both diode and magnetron) with dc or rf power (Hoon Yi, et al., 1995; Meng and Dos Santos, 1996), dc support of sputtering (Bender and Trude, 1999), chemical vapor deposition (CVD), and spray pyrolysis (Ramaiah, et al., 2000). The choice of deposition techniques is determined by various factors such as the quality and reproducibility of the films, the cost and complexity of the equipment, and the specific disadvantage of each technique.
The techniques most widely reported in the literature and most widely used in industry are dc magnetron sputtering, dc/rf magnetron sputtering and electron beam evaporation. Of these, dc magnetron sputtering produces both high rates of deposition and good–quality films (McMeeking, 2000).

### Thermal Evaporation

Solid material vaporizes when heated to sufficiently high temperatures. The condensation of the vapor onto a cooler substrate yields thin solid films. Thermal evaporation may be achieved directly or indirectly (via support) by a variety of physical methods (Chopra, 1969). This technique has several advantages: it is capable of yielding films that do not contain a significant amount of uncontrollable contaminations; it is relatively easy to operate; it involves a minimum of critical process parameters; and it does not cause radiation damage to the substrate (Hamberg and Granqvist, 1989; Yao, Hao and Wilkinson, 1990).

### Spray Hydrolysis (Pyrolysis)

The spray hydrolysis method has been used for the preparation of TCO films for many years because it is relatively simple and cheap. The conventional spray hydrolysis technique consists of spraying a dilute solution of appropriate chloride from an atomizer onto a heated substrate under normal atmosphere conditions or a controlled atmosphere. High-pressure argon, nitrogen, or air is usually used as spraying gas (Jarzębski, 1982).

### Chemical Vapor Deposition

Chemical vapor deposition (CVD) is a process in which a chemical reaction involving gaseous reacting species takes place on, or in the vicinity of, a heated substrate surface. The principle of CVD device. The main controlling parameters are the substrate temperature, substrate material, composition of the reaction gas mixture, gas flow, total pressure, and the geometry of the deposition system. The gas flow and the apparatus geometry determine the uniformity of the deposited films over large areas. The substrate temperature and the gas flow control the deposition rate (Bel Hadja Tahar, et al., 1998).

Films with high demands for purity, stoichiometry, and structural perfection could be obtained by CVD method (Jarzębski, 1982). This technique has also the advantage of being cost-effective concerning the apparatus. It enables the production of coatings with good properties even on substrates of complicated shapes without the use of a high vacuum. In particular, atmospheric pressure CVD (APCVD) is attractive in many applications in the sense that it offers a high deposition rate and hence short process time. However, since CVD processes are based on interfacial chemistry, they are sensitive to contamination. The major limitations of the process are the small areas of uniform coatings.

### Magnetron Sputtering

When a solid surface is attacked with energetic ions, collisions between the surface atoms and the energetic particles disperse the solid's surface atoms backward, as illustrated in Figure 2. The phenomenon is called “back-sputtering” or simply “sputtering,” when a thin foil is bombarded with energetic particles some of the majority of the dispersed atoms pass through the foil. “Transmission-sputtering” is another name for the phenomenon. The terms "sputtering" and "sputtering" are interchangeable. The terms "cathode sputtering," "cathode disintegration," and "impact evaporation" are also interchangeable. (K Wasa, S Hayakawa, 1992).

Wehner and Anderson published seminal papers on cathode sputtering. (LI Maissel,1976). Sputtering systems including DC diode, RF diode, magnetron diode, and ion beam sputtering are all utilized in practice. Figures 8 and figures 10 depict typical sputtering systems. A historical overview of sputtering deposition was provided by McClanahan and Laegreid (R Behrisch, 1981). The DC diode sputtering system depicted in Figure 8 is the simplest of these sputtering systems. A pair of planar electrodes make up the DC sputtering apparatus. One electrode is a cold cathode, while the other is an anode. The cathode's front surface is coated in target materials to be deposited. The anode is where the substrates are put. Sputtering gas, generally Argon gas at 1-5 Pa, is fed into the sputtering chamber. Under the application of DC voltage between the electrodes, the glow discharge is maintained. The $Ar^+$ ions generated in the glow discharge are accelerated at the cathode fall (sheath) and sputter the cathode target resulting in the deposition of the thin films of the cathode target on the substrates. In the DC sputtering system, the target is composed of metal, since the glow discharge (i.e., current flow) is maintained between the metallic electrodes.

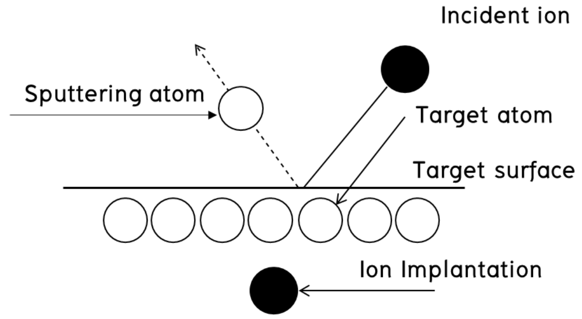

Figure 8 Physical sputtering processes (Maissel, L. I., Glang, R., & Budenstein, P. P., 1971).

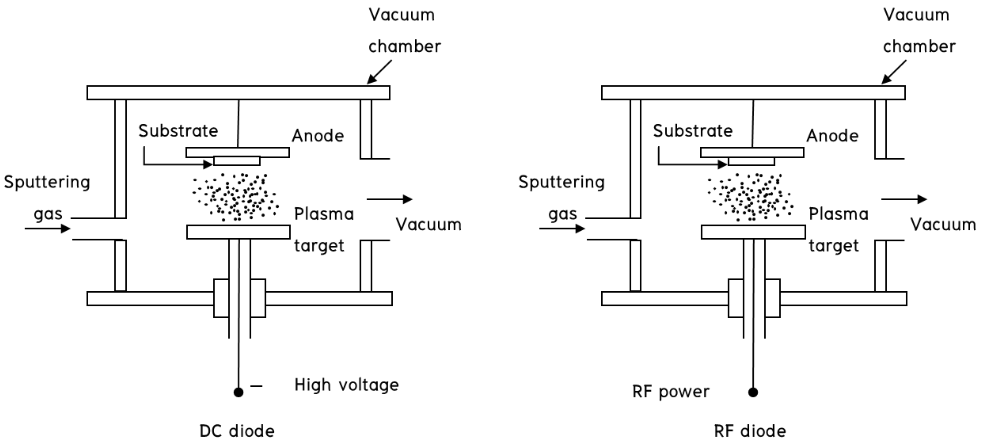

Figure 9 Sputter deposition systems. (Maissel, L. I., Glang, R., & Budenstein, P. P., 1971).

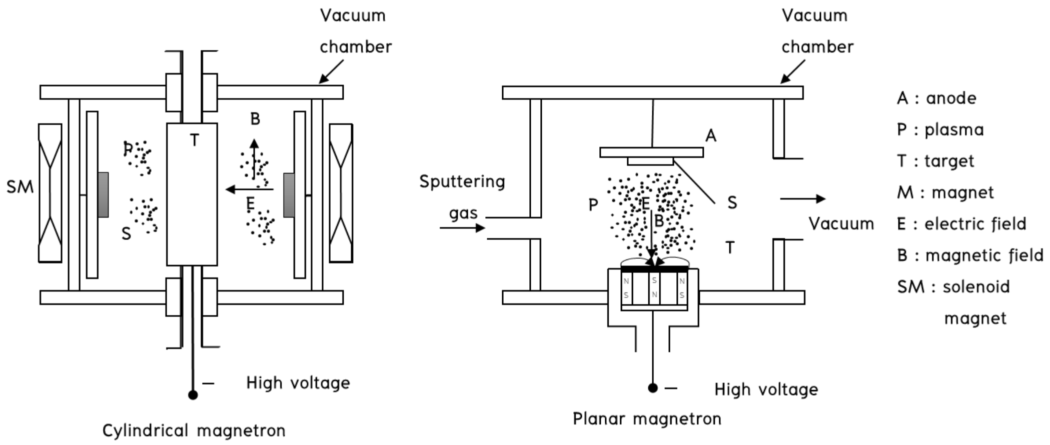

Figure 10 Magnetron sputter deposition systems.

(Maissel, L. I., Glang, R., & Budenstein, P. P., 1971).

Because of the quick development of a surface charge of positive ions on the front side of the insulator when an insulator is substituted for the metal target in a DC sputtering discharge system, the sputtering discharge cannot be sustained. The insulator target is supplied with RF voltage to keep the glow discharge going. As illustrated in Figure 9, this system is known as RF-diode sputtering. The thin insulator coatings are sputtered directly from the insulator target in the RF-sputtering system.

The deposition rates of sputtering systems are lower than those of vacuum deposition. Lowering the sputtering pressure increases the deposition rates. To lower the sputtering pressure, magnetron-type discharge is introduced as shown in Figure 10. Two types of magnetron sputtering system are used in practice. One is a planar magnetron and the other is a coaxial magnetron (cylindrical magnetron).

In the magnetron sputtering system, a magnetic field is superposed on the cathode which is parallel to the cathode surface. The electrons in the glow discharge show cycloid motion and the center of the orbit drifts in a direction of **E** x **B** with the drift velocity of **E/B**, where **E** and **B** denote the electric field in the discharge and the superposed transverse magnetic field, respectively. The magnetic field is oriented such that these drift paths for electrons form a closed loop. This electron trapping effect increases the collision rate between the electrons and the sputtering gas molecules. This enables one to lower the sputtering gas pressure as low as $10^{-1}$ Pa, but more typically 0.5-1 Pa. In the magnetron sputtering system, the magnetic field increases the plasma density, which leads to increases in the current density at the cathode target, effectively increasing the sputtering rate at the target. Due to the low working gas pressure, the sputtered particles traverse the discharge space without collisions, which results in a high deposition rate.

### Direct current (dc) sputtering

Due to a high sputtering rate and good film performances, dc-magnetron sputtering is used widely. The arrangement for our dc sputtering system is shown in Figure 11. The material to be sputtered is used as a cathode (target) of an electrical circuit, and a high negative voltage V(dc) is applied to it. The substrate on which the film is to be deposited is placed on an electrically floating substrate holder (anode) 5 cm away. An inert gas (e.g., Argon) is introduced into the chamber to some specified pressure (~$10^{-3}$ mbar). The action of the electric field is to accelerate electrons which in turn collide with argon atoms, breaking some of them up into argon ions and more electrons to produce the glow discharge. The charged particles thus produced are accelerated by the field, the electrons tending towards the anode and the ions towards the cathode so that a current I flows.

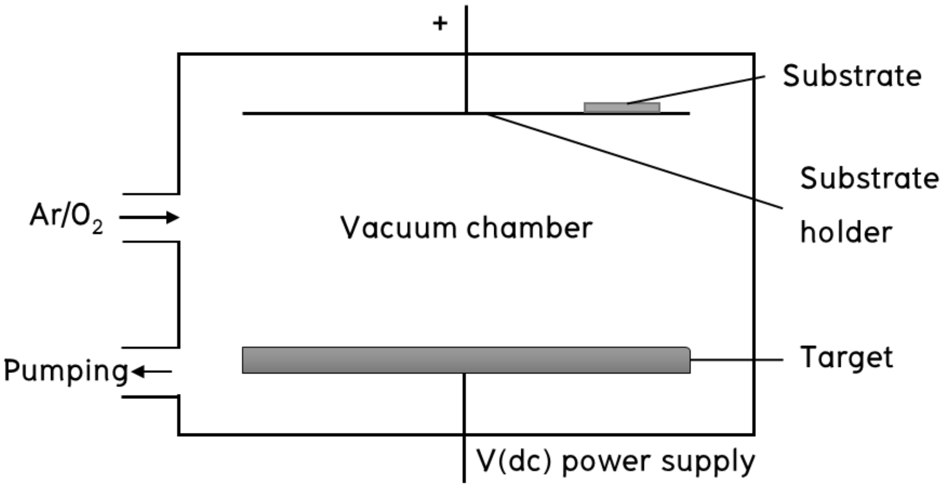

Figure 11 Schematic diagrams of a dc sputtering system (Qiao, Z., 2003).

**Radiofrequency (RF) sputtering**

DC method cannot be used to sputter nonconducting targets because of charge accumulation on the target surface. This difficulty can be overcome by using radio frequency (rf) sputtering. A single RF sputtering apparatus can be used to deposit conducting, semiconducting, and insulating coatings. RF reactive sputtering offers several advantages compared with other techniques such as CVD and PVD: it is possible to predict the layer structure and thickness; compound materials may be sputtered roughly without losing the target stoichiometry; good adherence and high film density can be achieved because of the high kinetic energy of the incident target atoms; and uniform layer thickness is obtained (Carl, Schmitt and Friedrich, 1997).

The technique of rf sputtering uses an alternating voltage power supply at rf frequencies (13.56 MHz), so that the sputtering target is alternately bombarded by ions and then electrons to avoid charge build-up. Hence, the insulators can be deposited by rf sputtering. In the case of rf sputtering, the plasma is mainly driven by ionization due to electrons which perform an oscillating motion in the plasma body. The electrons can follow the rf frequency of 13.56 MHz while the ions are not, due to their large inertia. This kind of excitation is much more effective compared to the ionization by non-oscillating secondary electrons (in the case of dc-sputtering) and leads to lower target voltages in an rf discharge (Ellmer, 2000) and the operating pressure could also be practically extended down to 1 mtorr (Chapman, 1980).

## SUBSTRATE MATERIALS

### $SiO_2$/Si wafer

Silicon dioxide, $SiO_2$, is an amorphous material used in microsystems as a dielectric in capacitors and transistors; as an insulator to isolate various electronic elements, and as a structural or sacrificial layer in many micromachining processes. Thin films of oxide are easily grown or deposited on silicon wafers using a variety of techniques that are reviewed in Section 2.3. High-quality oxide films provide excellent electrical insulation with resistivity values as high as $10^{10}$ $\Omega$-m. Oxide films are also good thermal insulators, with a low thermal conductivity of around 1.4 W/m-K. Phosphorous-doped and boron-doped oxides, known as phosphosilicate glass (PSG) and borosilicate glass (BSG), respectively, will flow at temperatures above approximately 900°C. Reflow of PSG and BSG films is commonly employed for planarization purposes. Heavily doped PSG films are used as a sacrificial material in many surface-micromachining processes because of the rapid etch rate in hydrofluoric acid. (Bao, M. H., 2000).

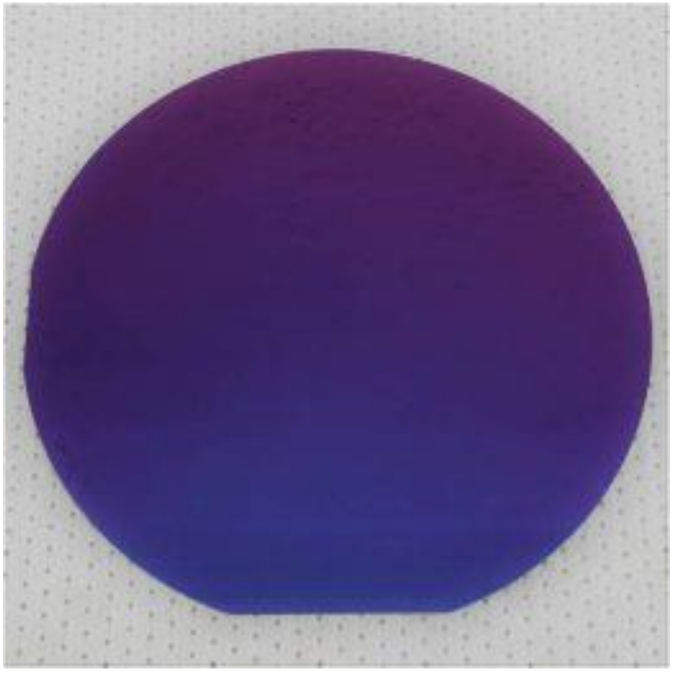

Figure 12 Si-$SiO_2$ (cheaptubes.com/product/cvd-graphene-si-sio2-4inch/).

### Polyimide

Polyimides (PIs) are high-temperature engineering polymers originally developed by the DuPont™ Company. PIs exhibit an exceptional combination of thermal stability (>500°C), mechanical toughness, and chemical resistance. They have excellent dielectric properties and inherently low coefficients of thermal expansion. They are formed from diamines or diisocyanates and dianhydrides such as those shown in Figure 13 (McKeen, L. W., 2017).

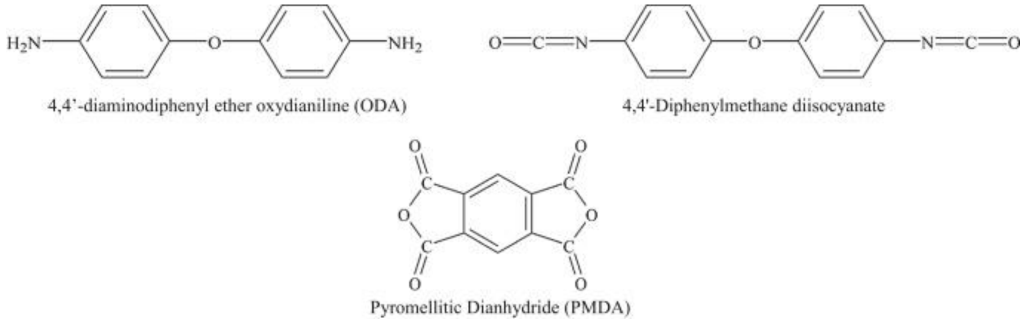

4,4'-diaminodiphenyl ether oxydianiline (ODA)

4,4'-Diphenylmethane diisocyanate

Pyromellitic Dianhydride (PMDA)

Figure 13 Chemical structures of monomer used to make polyimides. (McKeen, L. W., 2017).

- The reaction between a dianhydride and a diamine, which is the most common method and results in the elimination of water molecules during the polymerization to polyimide.
- The reaction between a dianhydride and a diisocyanate, results in the elimination of carbon dioxide molecules during the polymerization to polyimide.

Many other diamines and several other dianhydrides may be chosen to tailor the final properties of a polymer whose structure is like that shown in Figure 14.

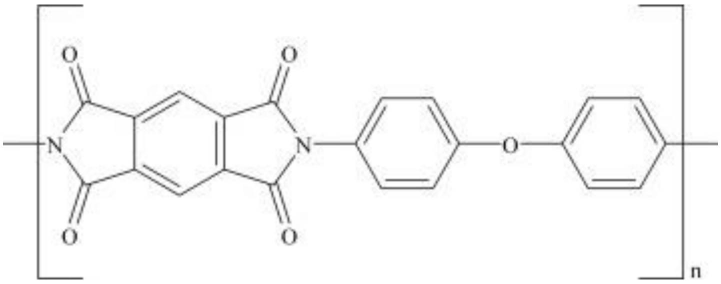

Figure 14 Chemical structure of a typical polyimide. (McKeen, L. W., 2017).

Figure 15 Kapton HN Thermal Insulating Film (https://cipherengineers.com/shop/kapton-film-304x200x0-075mm/).

**Specifications of Kapton HN Thermal Insulating Film**

| Attribute | Value |
|---|---|
| Material | Kapton HN |
| Length | 304mm |
| Width | 200mm |
| Thickness | 0.05mm |
| Density | 1.42g/cm³ |
| Dielectic Strength | 118kV/mm |
| Thermal Conductivity | 0.16W/mK |
| Maximum Operating Temperature | +400°C |

## P-TYPE ALLOY; Ag-Sb-Te MATERIALS

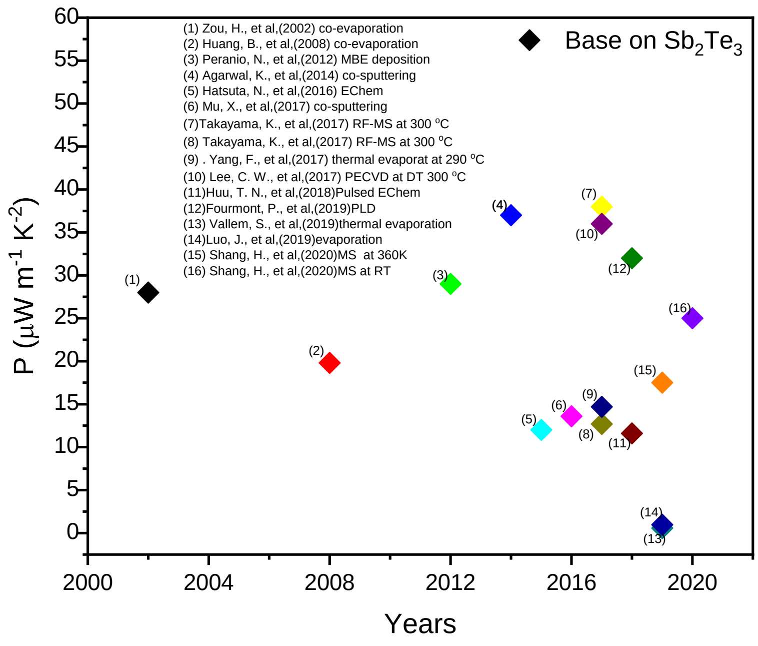

Figure 16 Shows the power factor of $Sb_2Te_3$ from 2002-2020

Figure 16 show review more deposition method for enhancement on power factor of $Sb_2Te_3$ thin film: Zou, H., et al. (2002) report A thin film $Sb_2Te_3$-$Bi_2Te_3$ based thermocouple was fabricated by co-evaporation. The conditions for deposition have been investigated as a function of substrate temperature ($T_S$) and flux ratio [$F_r$=$F$(Te)/$F$(Sb,Bi)] and optimised to achieve a high thermoelectric power factor. It has been observed that the Seebeck coefficient and electrical conductivity of p-type $Sb_2Te_3$ thin films ($\alpha_p$, $\rho_p$) and n-type $Bi_2Te_3$ thin films ($\alpha_n$, $\rho_n$) deposited by co-evaporation were found to be approximately 160 $\mu$V/K, $3.12\times10^{-3}\Omega$cm and -200 $\mu$V/K, $1.29\times10^{-3}\Omega$cm, respectively.

Zheng, et al. (2019) have a news idea of organic-inorganic hybridization was proposed to fabricate flexible p-type – $Sb_2Te_3/CH_3NH_3I$ thin films. High purity $Sb_2Te_3$ alloy target and CH3NH3I powder were placed in a magnetron sputter and thermal evaporator on kapton tape of polyimide with a thickness of 0.15 mm respectively. The annealed hybrid-composite film showed a significant enhancement in thermoelectric performance, with a maximum ZT value of 0.94 at a temperature of 413 K.

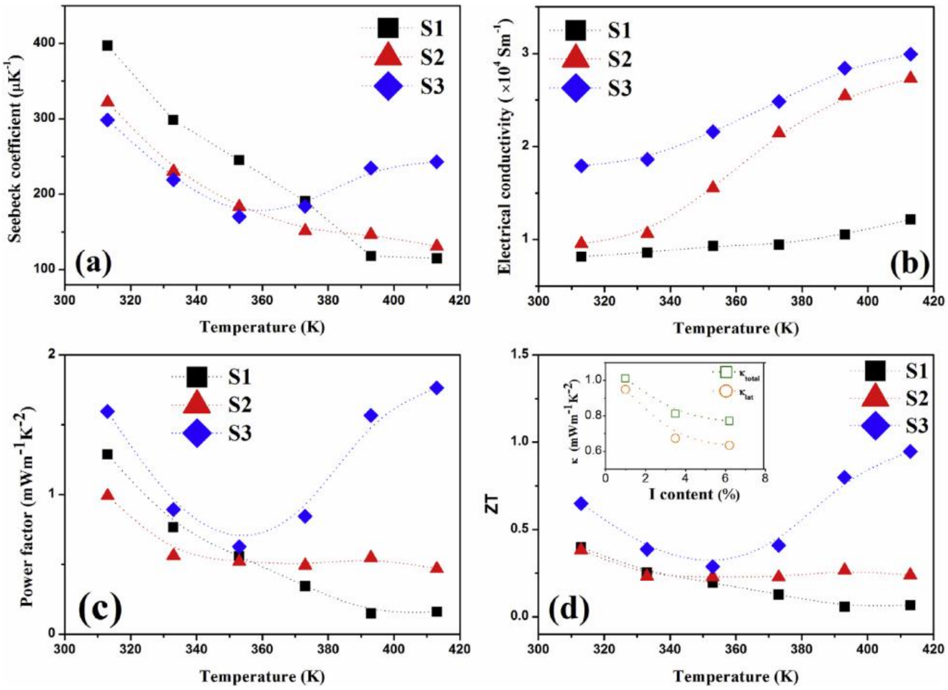

Figure 17 Seebeck coefficient, Electrical conductivity, Power factor and ZT value as the function of temperature: (a) Seebeck coefficient; (b) Electrical conductivity; (c) Power factor; (d) ZT values, including the plot of room-temperature total thermal conductivity and lattice thermal conductivity as illustration.

Khumtong, et al. (2017). In this work, a flexible antimony telluride thin film was deposited by RF magnetron sputtering. The Te content of the thin film was controlled by the Ar gas flow rate and the pre-heat temperature of the substrate. the effect of the Ar gas flow rate and pre-heat temperature on the structural, electrical and thermoelectric properties is The S value remained at 220 mV/K electrical conductivity was approximately 600 S/cm at 250 °C and maximum PF value was similar to this work at 1.87 $10^{-3}$ $Wm^{-1}K^{-2}$.

Song, et al. (2020). This study, a series of Ag-doped $\beta$ -$Cu_2Se$ films were prepared on single crystalline Si (111) substrate by magnetron sputtering and the influence of Ag doping on the phase composition, chemicalcomponent and thermoelectric performance of the deposited $\beta$-$Cu_2Se$ films were studied. showed that the Cu-rich $\beta$ -$Cu_2Se$ films in which the ratio of Cu to Se in $\beta$ -$Cu_2Se$ lattice varied from 3.59 to 4.96 as Ag atomic percent content increased from 0 to 2.97 were obtained. whose the lowest resistivity was in the range from 30 to 100 μΩ.m, in which Seebeck coefficient values were 100~250 μV/K. and power factor of our deposited films reached the order of $mW.m^{-1}K^{-2}$ . As measured temperature varied from 150 to 500 °C.

$Sb_2Te_3$ and $Bi_2Te_3$ thin films showing S of 624 and -78 μV/K respectively were prepared by PLD. ( Fourmont, P., 2018) These films deposited on glass substrates had smooth surfaces with small crystal grains and blurry boundaries. The avg. grain sizes of 9.85 and 29.33 nm were observed for $Sb_2Te_3$ and $Bi_2Te_3$ films, respectively. In this method, films were prepared at different $T_{sub}$ and post-annealing treatment free. Defects formed during the PLD growth enhanced the charge carrier concentration, (1-7) × $10^{21}/cm^3$. TE power generator consisting of four pairs of n-type $Bi_2Te_3$ and p-type $Sb_2Te_3$ legs connected in series generated a maximum voltage of 50 mV and a power density of ~120 $\mu W/cm^2$ at $\Delta T$ of 30 K. Nanostructured Bi2Te3 (n-type) thin films were deposited on $SiO_2$/Si(100) substrates by PLD.
The $Bi_2Te_3$ films with high (001) orientation and a layered structure exhibited PFs of 18.2-24.3 $\mu W/cm\text{-}K^2$ when the substrate temperature (Tsub) was between 220 and

340 °C. (Le, P. H.;2014) Bassi et al., have applied PLD technique to prepare $Bi_2Te_3$ films on Si or cleaved mica with different morphologies at the micrometer/nanometer scale. Films with a layered Bi2Te3 structure showed the best properties, with S ranging from −175 to −250 μV/K, $\sigma$ ~ 714–666/Ω–cm, $\mu$ = 100 $cm^2/V$–s, $\kappa$ ~ 1.6–1.7 W/m–K, and PF in the range of 20–45 μW/cm–$K^2$ with an expected zT > 1.5. Further, it was found that the higher deposition temperatures (> 620 K) favor the hexagonal Bi2Te3(001) formation. Using Bi2Se2Te, a single crystal target, Le et al. prepared n–type nanocrystalline Bi–Se–Te ($Bi_3Se_2Te$) thin films on ($SiO_2$/Si) via PLD and obtained high n of ~1020 $cm^{-3}$ , $\sigma$ of 1747.5/Ω–cm at RT, S of – 68.8 μV/K at RT, and optimal PF of 8.3 μW/cm–K 2 at RT. (Le, P. H, 2016).

## THIN FILM THERMOELECTRIC GENERATOR

In wang et al 2013. Developing packing density micro–thermoelectric power generator base on N–type $Bi_2Te_{2.7}Se_{0.3}$ and p–type $Bi_{0.5}Sb_{1.5}Te_3$ by electrodeposition technology. A micro–thermoelectric power generator (MTEG) module with high packing density of film TE legs was proposed, a MTEG containing 160 film thermocouples was fabricated and its size was 4 mm (height) × 25 mm (width) × 1 mm (thickness). Its open–circuit voltage, maximum output power and corresponding power density under a temperature difference of 20 K at 25 °C are 660 mV, 77 μW and 770 μW $cm^{-3}$, respectively.

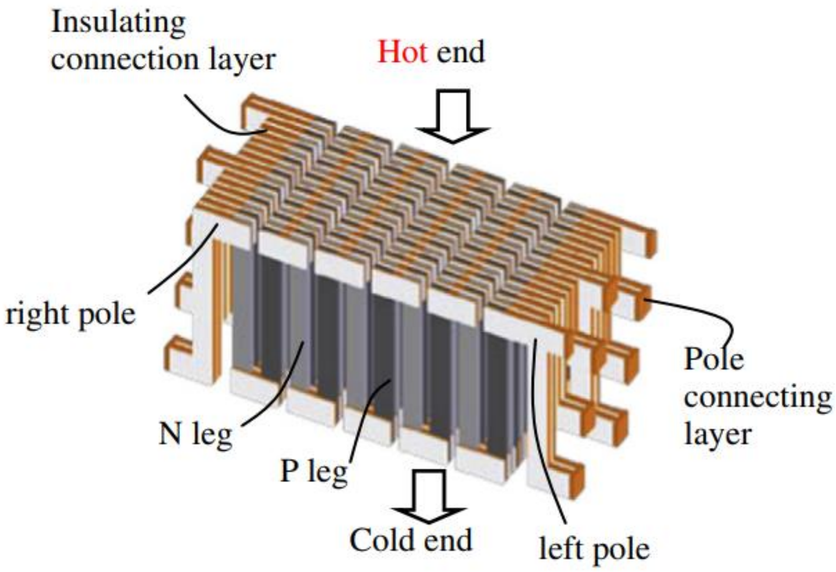

Figure 18 Schematic view of the thermoelectric aggregation. (Wang, et al, 2013).

Mu, et al. (2018). The fabrication of a micro/nano-scale thermoelectric module. The total thickness of the thermoelectric module is about 1 μm. Twenty-one devices are fabricated successfully, of which each is composed of 127 pairs of thermoelectric legs connected in series with an average resistance of 25 Ω. Without a load and at the temperature of 150 °C, the output voltage and output current are 18.5 mV and 671.9 μA, respectively.

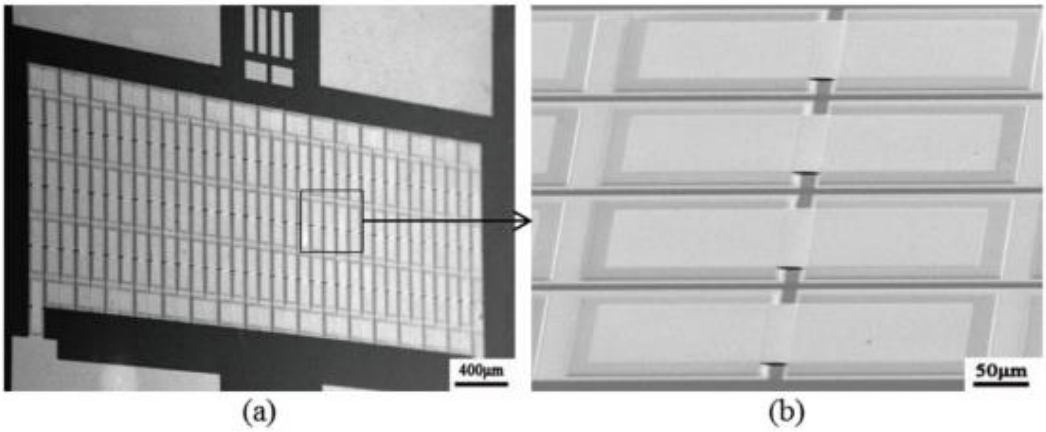

Figure 19 SEM images at the angle of 60° to the plane of the fabricated device. (a) SEM micrograph of the device with 127 TE pairs. (b) Locally enlarged SEM image of the device. (Mu et al, 2018).

Karthikeyan, et al. (2020) Developing a thermoelectric generator for wearable and multi-scale energy harvesting applications. Intact thin films of p-SnTe/n-PbTe are deposited on flexible substrate through physical vapor deposition and a thermoelectric module possessing a maximum output power density of 8.4 mW/cm$^2$ is fabricated. Thermoelectric performance of the deposited thin film exhibits maximum zT of ~0.3 (p-type) and ~0.2 (ntype) at 550 K. From the fabricated TEGs, maximum output voltage and power density of 250 mV and 8.4 mW/cm$^2$ at a temperature difference of 120 $^{o}$C.

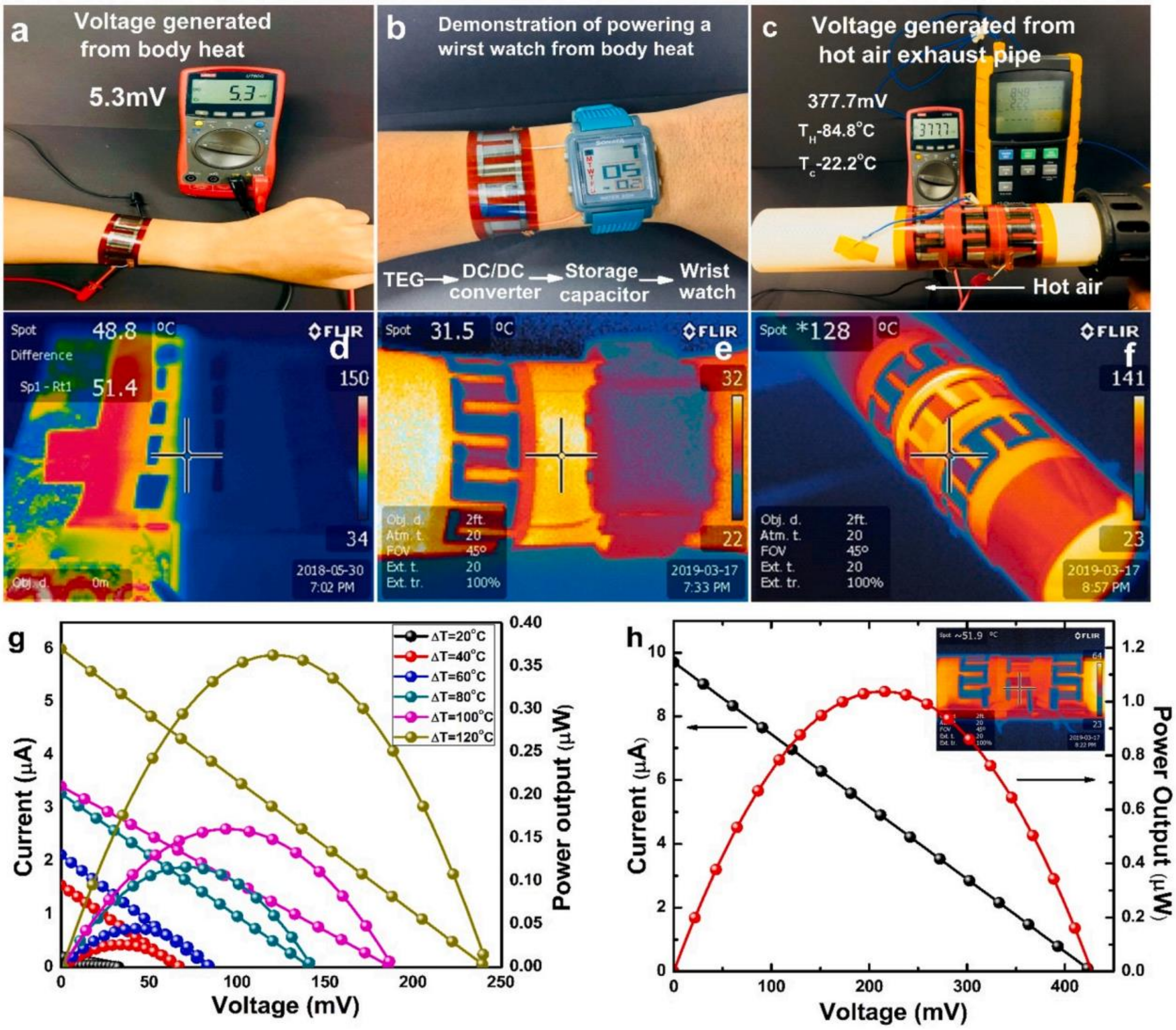

Figure 20 Real-time applications (a) shows the capability of the TEG to generate voltage(mV) from human body heat (b) demonstrates the possibility of fabricated TEG as flexible wearable electronics to replace batteries (c) shows the industrial high temperature power harvesting capability from heat exchangers. (d), (e) and (f) are the infrared images of TEG under various heat sources demonstrating the capacity of TEG to maintain temperature gradient (g) show the load characteristics performance of a single TEG under varied temperature gradients (h) load characteristic performance of serially connected TEGs over an alumina pipe with a temperature gradient of 120 °C. (Karthikeyan, et al, 2020).

# CHAPTER 3

# METHODOLOGY

Chapter 3 is composed of (i) AST thin film deposition method, (ii) AST thin film characterization method, (iii) the thin film thermoelectric properties measurement method and finally, (iv) the thin film thermoelectric module fabrication. The overall methodology was presented with the diagram as shown in Figure 21.

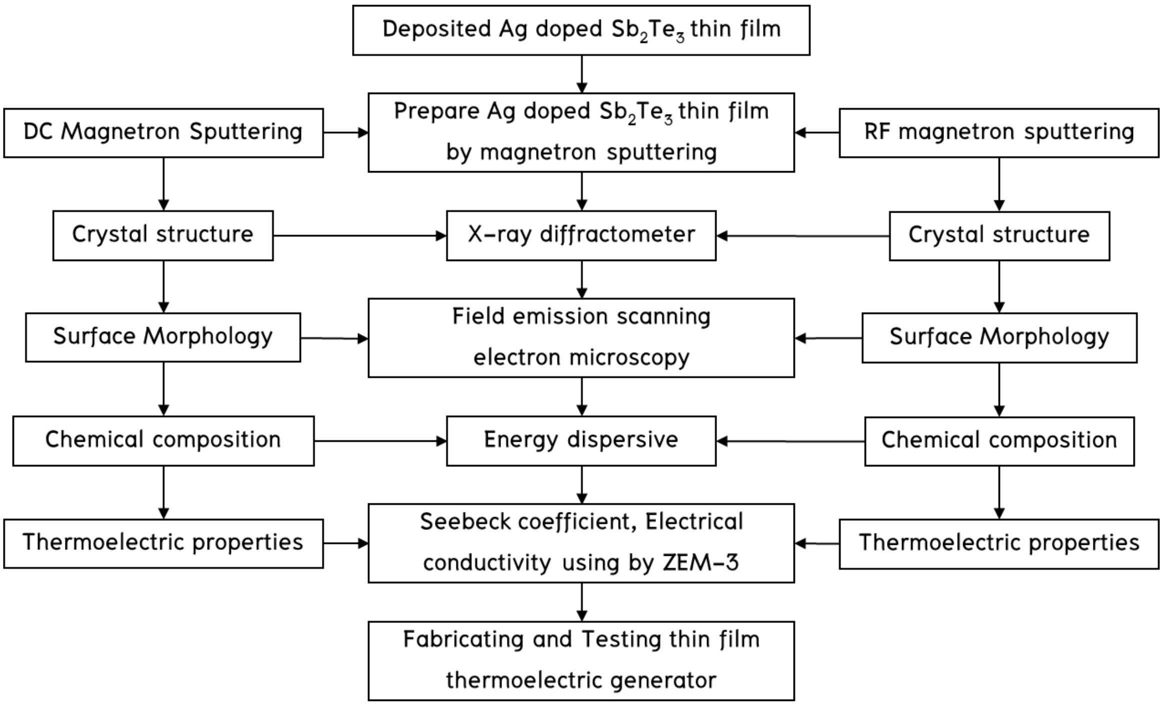

Figure 21 Show the diagram of the research methodology.

## AST THIN FILM DEPOSITION METHOD

In this work, the AST thin film was deposited base on both of DC and RF magnetron sputtering methods. One of the most popular methods for depositing films is the sputtering process. The material and equipment list used on this work are shown in Table 1 and Table 2, respectively.

Table 1 List of materials used for AST thin films deposition process

| Material | Formula | Supplier | Purity (%) | d/quantity |
|---|---|---|---|---|
| Silver antimony telluride | $AgSbTe_2$ | Leadmat Advanced Material Co.Ltd | 99.99% | 3in x 0.125in |
| Bismuth telluride | $Bi_2Te_3$ | Kurt J. Lesker | 99.99% | 3in x 0.125in |
| Argon gas | Ar | Thonburi Wattana Ltd. | 99.999% | 40 liter |
| Acetone | $C_3H_6O$ | QReC | 99.5% | 2.5 Liter |
| Methanol | $CH_3OH$ | Superco | 99.5% | 2.5 Liter |
| Iso Propanol | $C_3H_8O$ | QReC | 99.7% | 2.5 Liter |
| Substrate | $SiO_2$/Si–wafer | Kurt J. Lesker |  | 10 cm. |

Table 2 List of equipment used for the AST thin films deposition process

| Equipment | Model/Band | Application |
|---|---|---|
| Magnetron sputtering system | In house built | Coating conductor, Semiconductor and Oxide Material |
| DC Power supply | GPR-100H05D/GW INSTEK | Maximum Power 500 W (I=500 mA, V=1,000 V) |
| RF-Power supply | RFS-1310N/Ulvac | Maximum Power 1,000 W 13. 56 MHz |
| X-ray diffractometer (XRD) | 6100/LabX SHIMADZU | Crystal structure analysis |
| Seebeck coefficient/electrical resistance measuring system | ZEM-3/ULVAC-RIKO | Measured Seebeck coefficient, electrical resistance, and Power factor of materials |
| Field emission scanning electron microscopy (FE-SEM) | JSM-7610F/JEOL | Microstructure characterization and chemical composition |
| Mini Lamp Annealer | MILA-5000 series/ ULVAC-RIKO | Maximum temperature at 1,200°C and high speed heating maximum 50°C/s. |

## Preparation of AST thin film by DC-Magnetron Sputtering

1. AST thin films were prepared by a DC magnetron sputtering process onto 1-lm $SiO_2$/Si wafer and polyimide substrates at a target ratio of (99.99% purity) Ag:Sb:Te 1:1:2. The base pressure was below $5.5 \times 10^{-4}$ Pa as show in figure 22 (a) and (b), and the working pressure was about 0.93 Pa with Ar gas (99.999% UHP purity) set at a flow rate of 40 sccm. The sputtering power applied to the target was varied from 30 W, 50 W, 70 W, and 90 W, whereas the sputtering time was fixed at 10 min to optimize the atomic composition of the film on the SO substrates. For uniformity, the substrate holder was rotated at 10 rpm. More conditions as shown in Table 3.

Table 3 Deposition condition of AST film.

| | |
|---|---|
| Base pressure (Pa) | $5.5 \times 10^{-4}$ |
| Operating pressure (Pa) | 0.9 |
| Ar flow rate (sccm) | 40 |
| DC power (Watt) | 30 50 70 and 90 |
| Substrate rotation speed (rpm) | 10 |
| Deposition time (min) | 10 |
| Substrates | $SiO_2$/Si wafer and Polyimide |
| Annealing temperature (°C) | 150, 200, 250, and 300 |
| Rapid thermal Annealing (°C/sec) | 5 |
| Annealing time (min) | 8 |

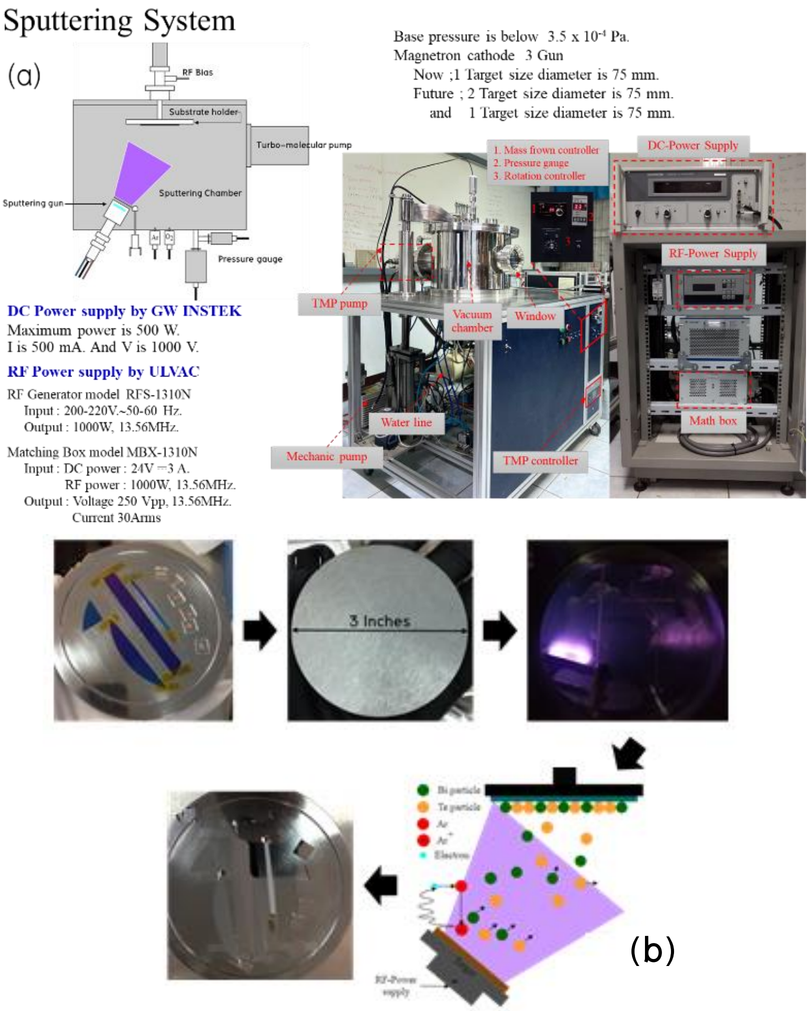

Sputtering System

Base pressure is below 3.5 x $10^{-4}$ Pa.
Magnetron cathode 3 Gun
Now ;1 Target size diameter is 75 mm.
Future ; 2 Target size diameter is 75 mm.
and 1 Target size diameter is 75 mm.

**DC Power supply by GW INSTEK**
Maximum power is 500 W.
I is 500 mA. And V is 1000 V.

**RF Power supply by ULVAC**
RF Generator model RFS-1310N
Input : 200-220V.~50-60 Hz.
Output : 1000W, 13.56MHz.

Matching Box model MBX-1310N
Input : DC power : 24V ⎓3 A.
RF power : 1000W, 13.56MHz.
Output : Voltage 250 Vpp, 13.56MHz.
Current 30Arms

Figure 22 (a) Magnetron sputtering system at Sakon Nakhon Rajabhat University. (b) Schematic presentation of the sputtering process.

2. After the deposition, A-ST thin films grown on both substrates with the sputtering power of 50 W were annealed by an RTA process (under the vacuum state) at temperatures of 150°C, 200°C, 250°C, and 300°C for 8 min (heating step of 5°C/s) show in figure 22 (b).

3. After the RTA process, the samples were analyzed for their microstructure, morphology-thickness, and atomic composition using an x-ray diffractometer (XRD; XRD6100, Shimadzu), field emission scanning electron microscope (FESEM; SU8030, Hitachi), and energy-dispersive x-ray spectroscopy (EDX; SU8030, Hitachi), respectively.

4. At room temperature, TE properties (electrical resistivity q and Seebeck coefficient S) of the annealed thin films were measured by the ZEM-3 apparatus (ZEM-3, Advance Riko) under a helium atmosphere.

### Preparation of AST thin film by RF-Magnetron Sputtering

1. AST thin films were prepared on silicon dioxide substrate by RF magnetron sputtering method using a target AST Purity of 99.99% Diameter of 76.2 cm and thickness of 0.3 cm. AST thin films are deposited onto SO substrate by RF magnetron sputtering method. The deposition condition used the sputtering RF power variation of 30, 50, 70 and 90 W whereas the sputtering time was fixed as 30 min. Thin film deposition was performed under an argon atmosphere with a flow rate of 35 sccm. The power used for depositions is 50W within the substrate holder rotations speed of 20, 40, 60, and 80 rpm.

2. As-deposited thin films were annealed by Rapid thermal annealing technique in a vacuum by using the Mini Lamp Annealer MILA-5000 series from ADVANCE RIKO, Inc. The conditions and scenarios of the thin film preparation method are shown in Table 4.

3. A study of the characterization of Crystal structure, microstructure and chemical composition of Ag-Doped Sb2Te3 thin films was observed by X-ray diffractometer (XRD-6100, SHIMUDZU), field emission scanning electron microscopy (FE-SEM) and High-Resolution Transmission Electron Microscopy (HR-TEM), and Energy Dispersive X-ray spectroscope (EDX), respectively.

4. Finally, thermoelectric efficiency or dimensionless Figure of merit (ZT) was calculated from the Seebeck coefficient, electrical conductivity and thermal conductivity as carried by using the ZEM-3 method.

Table 4 Deposition Condition of Ag doped $Sb_2Te_3$ Film.

| | |
|---|---|
| Base pressure (Pa) | $3.5 \times 10^{-3}$ |
| Operating pressure (Pa) | 3.5 |
| Ar flow rate (sccm) | 35 |
| RF power (Watt) | 30, 50, 70, and 90 |
| Substrate rotation speed (rpm) | 20, 40, 60, and 80 |
| Deposition time (min) | 30 |
| Substrates | SO |
| Annealing temperature (°C) | 250 |
| Rapid thermal Annealing ( °C/sec) | 5 |
| Annealing time (min) | 8 |

## Rapid thermal annealing process

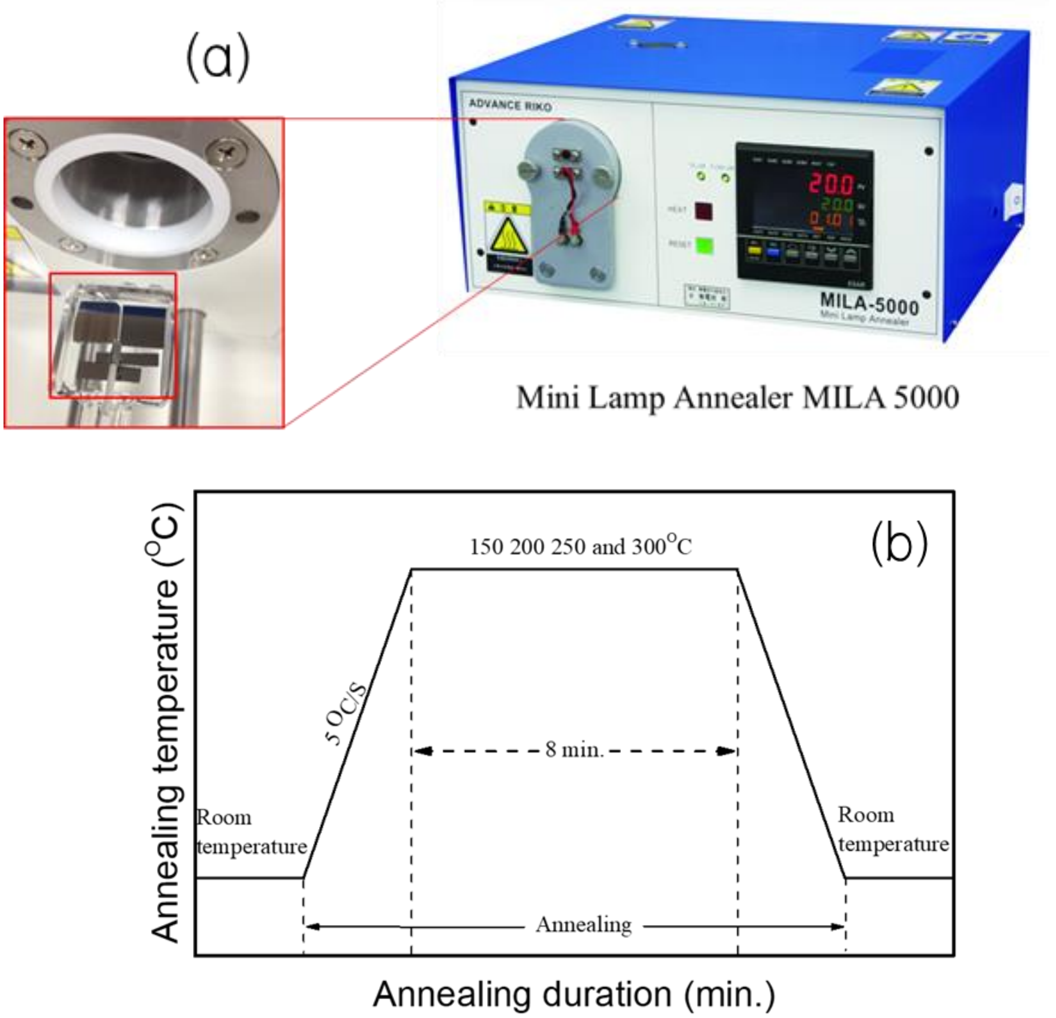

Figure 23 (a) Mini lamp annealer MILA-5000 series at Sakon Nakhon Rajabhat University. and (b) a schematic presentation of the rapid thermal annealing process steps.

## AST THIN FILM CHARACTERIZATION METHOD

After synthesized we can investigate the crystal structure, microstructure and chemical composition of Ag-Doped $Sb_2Te_3$ thin films were observed by X-ray diffractometer (XRD-6100, SHIMUDZU), field emission scanning electron microscopy JSM-7610FPlus, JEOL (FE-SEM):

### X-ray Diffraction Analysis

The characteristic x-ray diffraction pattern generated in a typical XRD analysis provides a unique of the crystals present in the sample. When properly interpreted, by comparison with standard reference patterns and measurements, this fingerprint allows identification of the crystalline form. When a focused X-ray beam interacts with these planes of atoms, part of the beam is transmitted, part is absorbed by the sample, part is refracted and scattered, and part is diffracted. The diffraction of an X-ray beam by a crystalline solid is analogous to the diffraction of light by droplets of water, producing the familiar rainbow. X-rays are diffracted by each mineral differently, depending on what atoms make up the crystal lattice and how these atoms are arranged (Pandian, 2014). These result in diffraction in which X-rays are emitted at characteristic angles based on the spaces between the atomic planes in the crystal structure. Most crystals have many sets of planes passing through their atoms. Each set of planes has a specific interlunar distance and will give rise to a characteristic angle for diffracted X-rays. The basic principle of XRD is Bragg's law, see Figure. 24, given by:

$$2d\_hkl\ \ \sin\boxed{f()}\theta=n\lambda \tag{19}$$

Where $d$, $\theta$, $\lambda$, and $n$ are lattice spacing, diffraction angle, the wavelength of the X-ray, and an integral number respectively. A set of 'd-spaces' obtained from a single compound will represent the set of planes that can pass through the atoms and can be used for comparison with sets of d-spaces obtained from standard compounds (Overview, 2013).

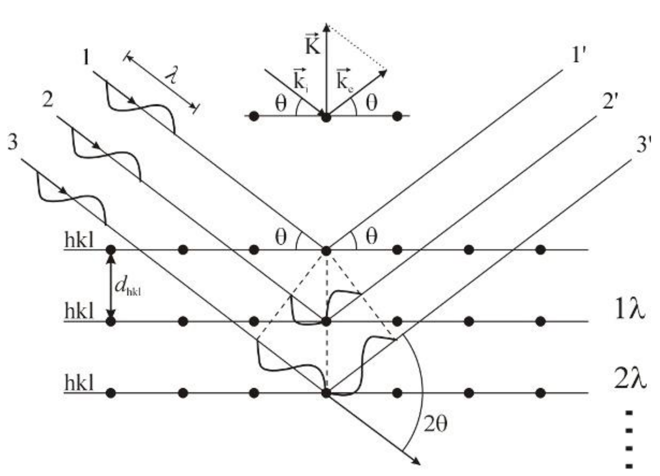

Figure 24 Diffraction (i.e. constructive interference of the scattered X-rays) will occur if the Bragg condition (eq. 19) is fulfilled and if the scattering vector K is parallel to the normal of the hkl-planes. (Meyers, 1997).

### Grain size

The coherence length *D* of the scattering material is determined from the halfwidth w of the reflexes by means of the Scherrer formula:

$$\square = \frac{\square\square}{\square'\square\square\square(\square)} \quad \textbf{(20)}$$

$$\square' = \sqrt{\square^{\square} - \square^{\square}} \quad (21)$$

with δ being the resolution of the spectrometer, here 0.01°, K is a shape factor and assumes a value of 0.9 for spherical particles (Mergel, et al., 2001).

The X-ray diffraction (XRD, Shimadzu, XRD-6100) measurements were performed at the Center of Excellence on Alternative Energy at Sakon Nakhon Rajabhat University, Thailand as shown in Figure 25. The crystal structure was analyzed by Xray diffractometer by using Cu-K$\alpha$1 radiation at room temperature ($\lambda$= 1.5406 Å) in a scan range of 20-80 degrees of 2$\theta$ for 2 deg/min of scan speed with 0.02 of sampling pitch.

Figure 25 X-ray diffractometer of the Center of Excellence on Alternative Energy at Sakon Nakhon Rajabhat University.

### **Field emission scanning electron microscopy (FE-SEM)**

Field emission scanning electron microscopy (FE-SEM) provides topographical and elemental information at magnifications of 10x to 300,000x, with virtually unlimited depth of field. Compared with conventional scanning electron microscopy (SEM), field emission SEM (FE-SEM) produces clearer, less electrostatically distorted images with spatial resolution down to 1 1/2 nanometers – three to six times better.

Preparation of Ag-Doped $Sb_2Te_3$ thin films sample by JSM-7610FPlus, JEOL (FE-SEM) shown in Figure 26 measured of surface morphology and cross-sections cross sections for confirming thickness of the thin film. The time taken to measure is not long because the film conducts electricity well and does not contain moisture.

An FE-SEM is used to visualize very small topographic details on the surface or entire fractioned objects. Researchers in biology, chemistry and physics apply this technique to observe structures that may be as small as 1 nanometer (= billion of a millimetre). The FE-SEM may be employed for example to study organelles and DNA material in cells, synthetical polymeres, and coatings on microchips. The microscope (JANSSEN, G. J., 2015).

Figure 26 Field emission scanning electron microscopy JSM-7610FPlus, JEOL (FE-SEM) of Ubon ratchathani university and preparation of Ag-Doped $Sb_2Te_3$ thin films.

### Energy Dispersive Spectroscopy (EDS)

Energy dispersive spectroscopy (EDS) identifies the elemental composition of materials imaged in a scanning electron microscope for all elements with an atomic number greater than boron. Most elements are detected at concentrations on the order of 0.1 percent. As the electron beam of the SEM is scanned across the sample surface, it generates X-ray fluorescence from the atoms in its path. The energy of each X-ray photon is characteristic of the element that produced it. The EDS microanalysis system collects the X-rays, sorts and plots them by energy, and automatically identifies and labels the elements responsible for the peaks in this energy distribution. Typically, EDS data are compared with either known or computer-generated standards to produce a full quantitative analysis showing the sample composition. Data output includes plots of the original spectrum, showing the number of X-rays collected at each energy. Maps of element distributions over areas of interest and quantitative composition tables can also be produced.

## THIN FILM THERMOELECTRIC PROPERTIES MEASUREMENT METHOD

### Seebeck Coefficient/Electric Resistance Measurement System ZEM-3 series

Figure 27 Seebeck Coefficient/Electric Resistance Measurement System ZEM-3 series at center of excellence on alternative energy sakon nakhon rajabhat university.

The ZEM-3 unit is the worldwide de facto standard for thermoelectric material measurements at temperatures from RT, 50 °C to 1,000°C. Easy to use straightforward operation with great accuracy & repeatability is why the ZEM-3 becomes the favourite instrument in many labs across the globe. The Seebeck Coefficient / Electric Resistance Measurement system is shown in Figure 27. The Seebeck coefficient and electrical resistivity were measured by ZEM-3 (https://showcase.ulvac.co.jp/en/).

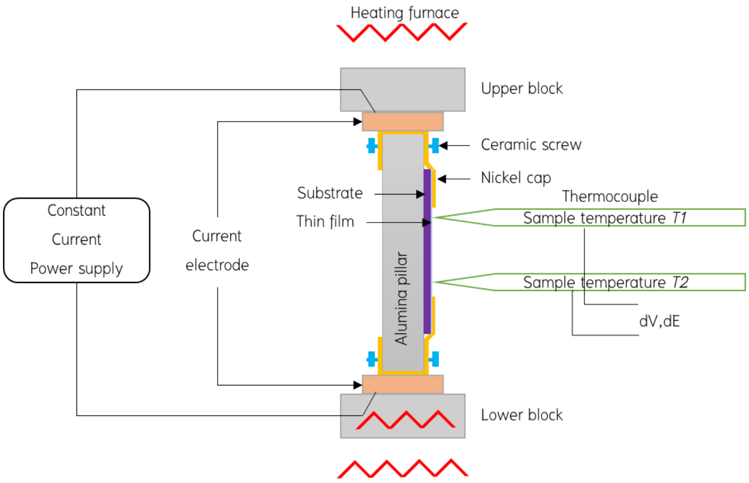

Figure 28 The schematic diagram of Seebeck coefficient and electrical resistivity measurement. (https://showcase.ulvac.co.jp/en/products/ ZEM-3 series).

A prism or cylindrical sample is set in a vertical position between the upper and lower blocks in the heating furnace. While the sample is heated and held at a specified temperature, it is also heated by the heater in the lower block to provide a temperature gradient. The Seebeck coefficient is measured by measuring the upper and lower temperatures $T_1$ and $T_2$ with the thermocouples pressed against the side of the sample, followed by the measurement of the thermal electromotive force dE between the same wires on one side of the thermocouple. Electric resistance is measured by the DC four-terminal method, in which a constant current is applied to both ends of the sample to measure and determine the voltage drop dV between the same wires of the thermocouple by subtracting the thermo-electromotive force between the leads.

## THIN FILM THERMOELECTRIC MODULE AND MEASUREMENT

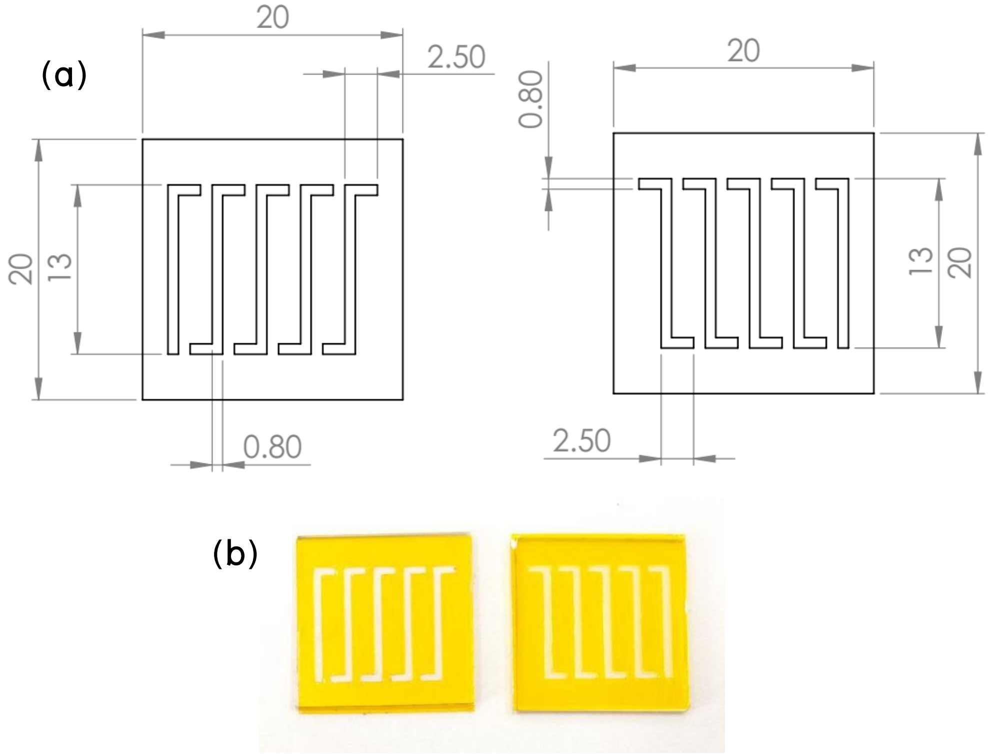

Figure 29 Schematic design of thin film thermoelectric module (b) sticker mask for deposition thin film thermoelectric.

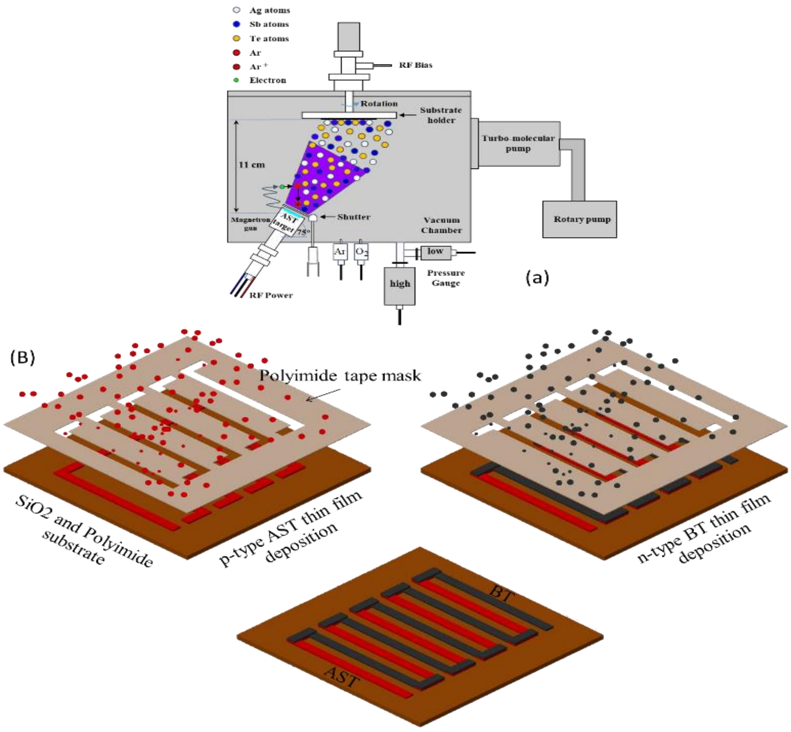

Figure 30 (a) schematic of magnetron sputtering (b) schematic fabrication process of a thermoelectric generator.

First, create a 3D view of the thin film thermoelectric module using the SolidWorks program, then export the 3D file to a line for cutting mask stickers with the Silhouette CAMEO machine V.3 to be deposited thin film thermoelectric.

Fabrication of the device: Figure 30 (b) demonstrates the thin film thermoelectric generator's schematic fabrication procedure. First, *p*-AST and *n*-BT arrays with a thickness of 185 nm were deposited as *p*-*n* leg junctions on harder (SO) and softer (PI) substrates. The deposition process was carried by RF magnetron sputtering of high purity (99.99%) AST and BT target at room temperature. The deposition conditions, operating at pressure were 3.5 Pa and the deposition times of AST and BT were the same at 30 min. All conditions for the thin films of AST and BT are shown in Table 5, which is the invention of this thin film thermoelectric module. The design was made using the 'Solid Work' program (AST-BT in series with 5 pairs). After the design, a sticker cutter was used to cut the polyimide tape as a mask for the fabrication of thin film thermoelectric modules with magnetron sputtering.

Table 5 Conditions for the thin films of AST and BT.

| | |
|---|---|
| Base pressure (Pa) | $3.5 \times 10^{-3}$ |
| Operating pressure (Pa) | 3.5 |
| Ar flow rate (sccm) | 35 |
| RF power (Watt) | 50 |
| Substrate rotation speed (rpm) | 60 |
| Deposition time (min) | 30 |
| Substrates | SO and PI |
| Annealing temperature (°C) | 250 |
| Rapid thermal annealing (°C/sec) | 5 |
| Annealing time (min) | 8 |

Analysis of the thermoelectric performance: testing of power generation of thin film thermoelectric modules at room temperature by heating the temperature $T_H$ electrically series-connected side on the other side, which is connected in parallel. The heat has a $T_C$ temperature as fixed at room temperature and tries to find the relationship between the temperature difference ($\Delta T = T_H - T_C$) and the electric potential difference (V), current (I), and internal resistance (R) using plane heat transmission principle thin films. The hot side is fixed at 100°C, and the cold side is used as a Peltier plate, the cold side is set to 25 °C. The hot side and the cold side have a K-type thermometer connected to a data logger to collect data and confirm the heat flow according to the thermal image system with the IR384P thermal imaging camera. Measure the electric potential difference with the portable digital multimeter model M3500A. To store the current data of the thin film thermoelectric. has been connected to the adjustable load match It has a maximum resistance of 1 M$\Omega$ and then measures electrical current with Keithley Series 6400 Picoammeters Model 6485.

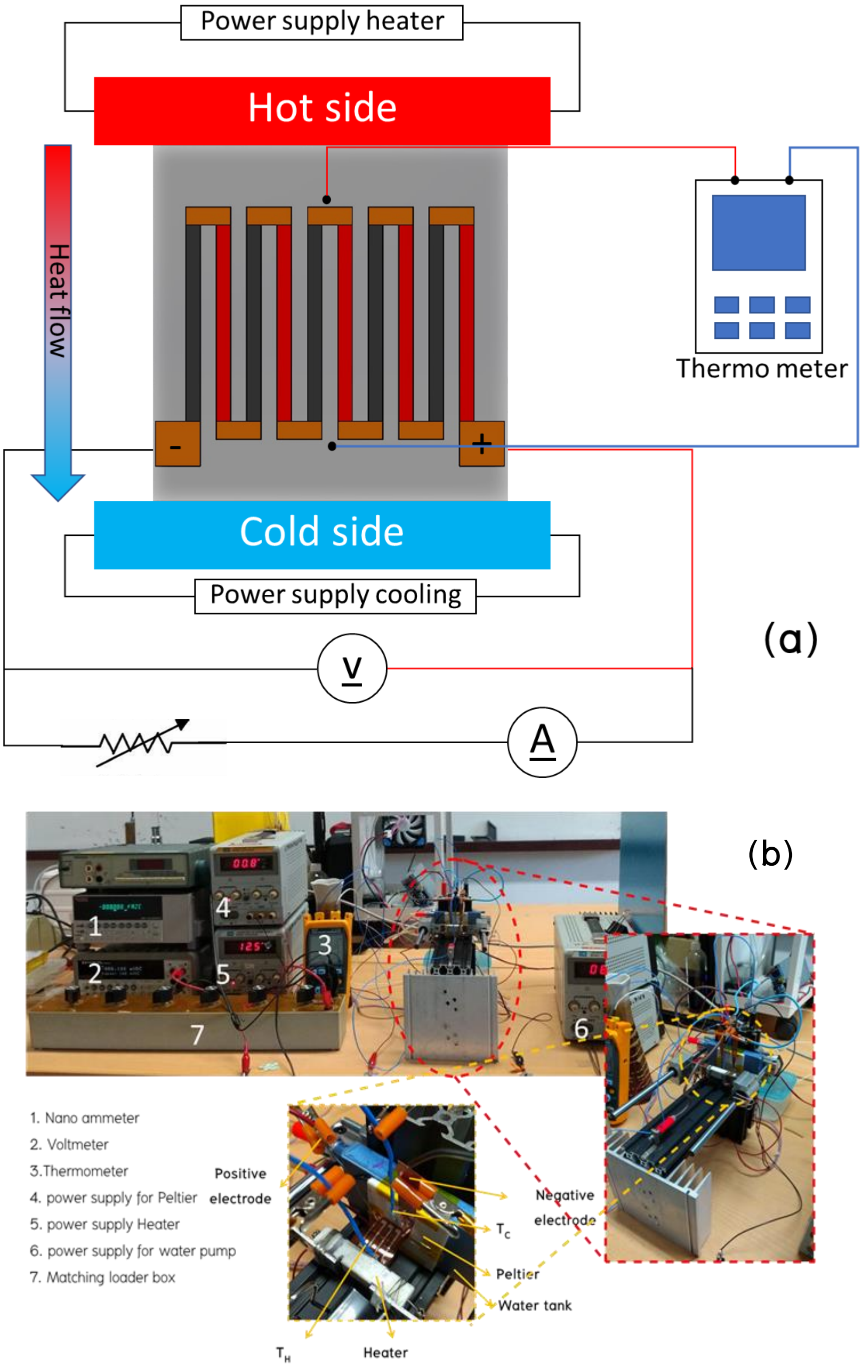

Figure 31 (a) Schematic of thin film thermoelectric power generator

(b) measurement of thin film Thermoelectric power generator.

# CHAPTER 4

# RESULTS AND DISCUSSION

Chapter 4 is the results and discussion of (i) AST thin films deposited by DC magnetron sputtering, (ii) AST thin films deposited by RF magnetron sputtering, and (iii) thin film thermoelectric module.

## AST THIN FILM DEPOSITED BY DC MAGNETRON SPUTTERING

### Crystal structure, morphology, and chemical composition of AST Thin Film

Figure 32 shows the microstructure and atomic composition of the as-deposited film as optimized by varying DC sputtering power to be applied to the target at 30 W, 50 W, 70 W, and 90 W. The microstructure and atomic composition of the as-deposited film were determined by XRD and EDX techniques. Figure 32 a presents the XRD results of as-deposited thin films showing amorphous behaviour, which is a common feature of sputtered material. The EDX results showed that the Ag atoms consisted of the film at a sputtering power of 50 W to be configured to optimize the Ag doping into $Sb_2Te_3$ as shown in Figure 32 (b). Figure 33 shows the XRD patterns of AST thin films grown on SO and PI substrates with a sputtering power of 50 W, as a function of annealing temperature. Figure 32 (a) displays the $Sb_2Te_3$ phase structure of annealed AST thin films on SO by the diffraction peaks of (009), (00 $\underline{13}$), and (00$\underline{16}$) planes, as confirmed with JCPDS 15-0727. Figure 2b displays the phase structure of annealed AST thin films grown on PI substrates. Here, a peak of the (009) plane was observed, assigned as the XRD peaks of the $TeO_2$(LV, Bin, et al. 2010) due to the partially burned surface of the polymer substrate. (SOMDOCK, Nuttakrit, et al. 2019) This small hump due to the $TeO_2$ phase is attributed to the partial surface oxidation of unsaturated Te atoms. It should be noted here that annealing in normal vacuum conditions (as used in the present case) only minimizes the presence of oxygen atoms and does not completely restrain the oxygen atoms and subsequently the chance of surface oxidation. It should be further noted that polymer substrate could also be thermally unstable during vacuum annealing, as reported in an earlier study of Ref. (SOMDOCK, Nuttakrit, et al. 2019). Such conditions might lead to the diffusion of Ti atoms underneath towards the surface and therefore result in partial oxidation of Te. This result shows that in the case of the PI substrate, similar annealing conditions induce oxidation of the thin film surface.

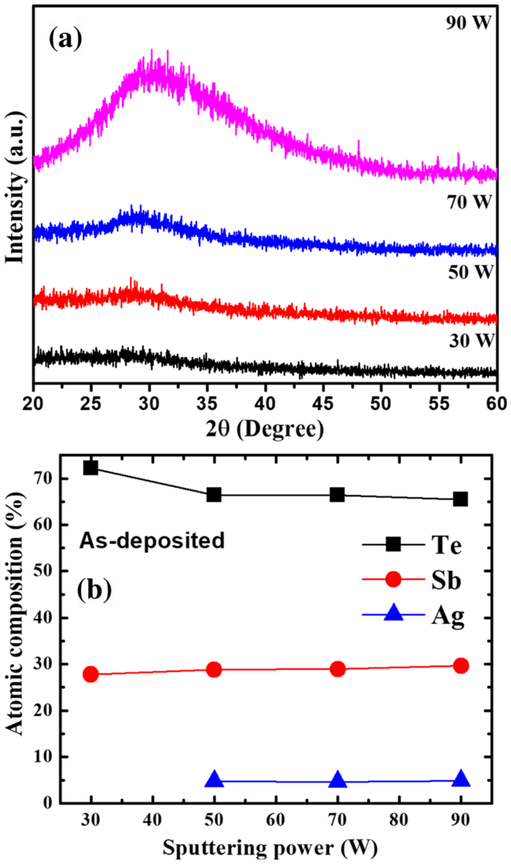

Figure 32 (a) XRD patterns and (b) atomic composition optimization of the as-deposited thin-film samples with varying sputtering power.

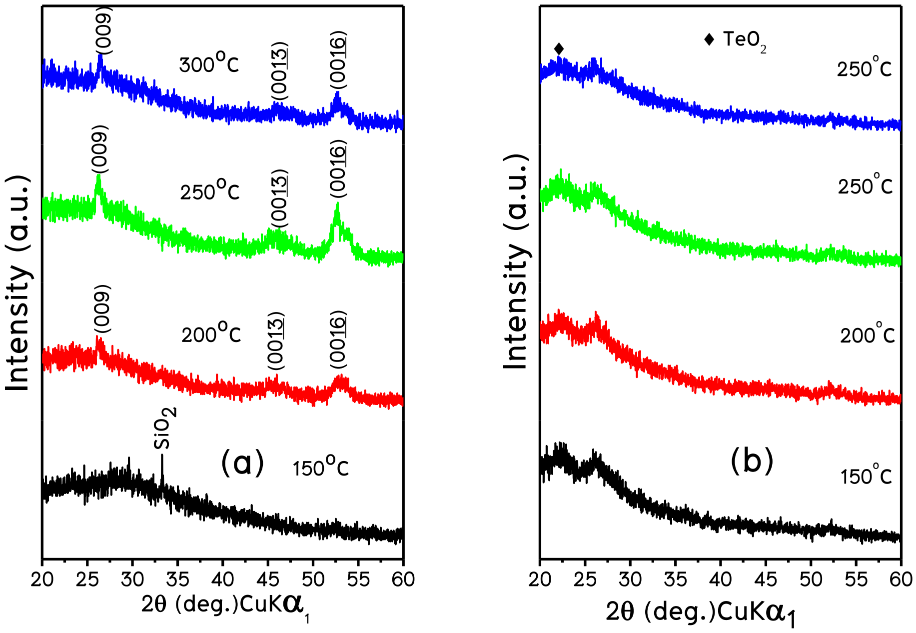

Figure 33 XRD patterns of AST thin films as a function of annealing temperature grew on (a) SO and (b) PI substrates.

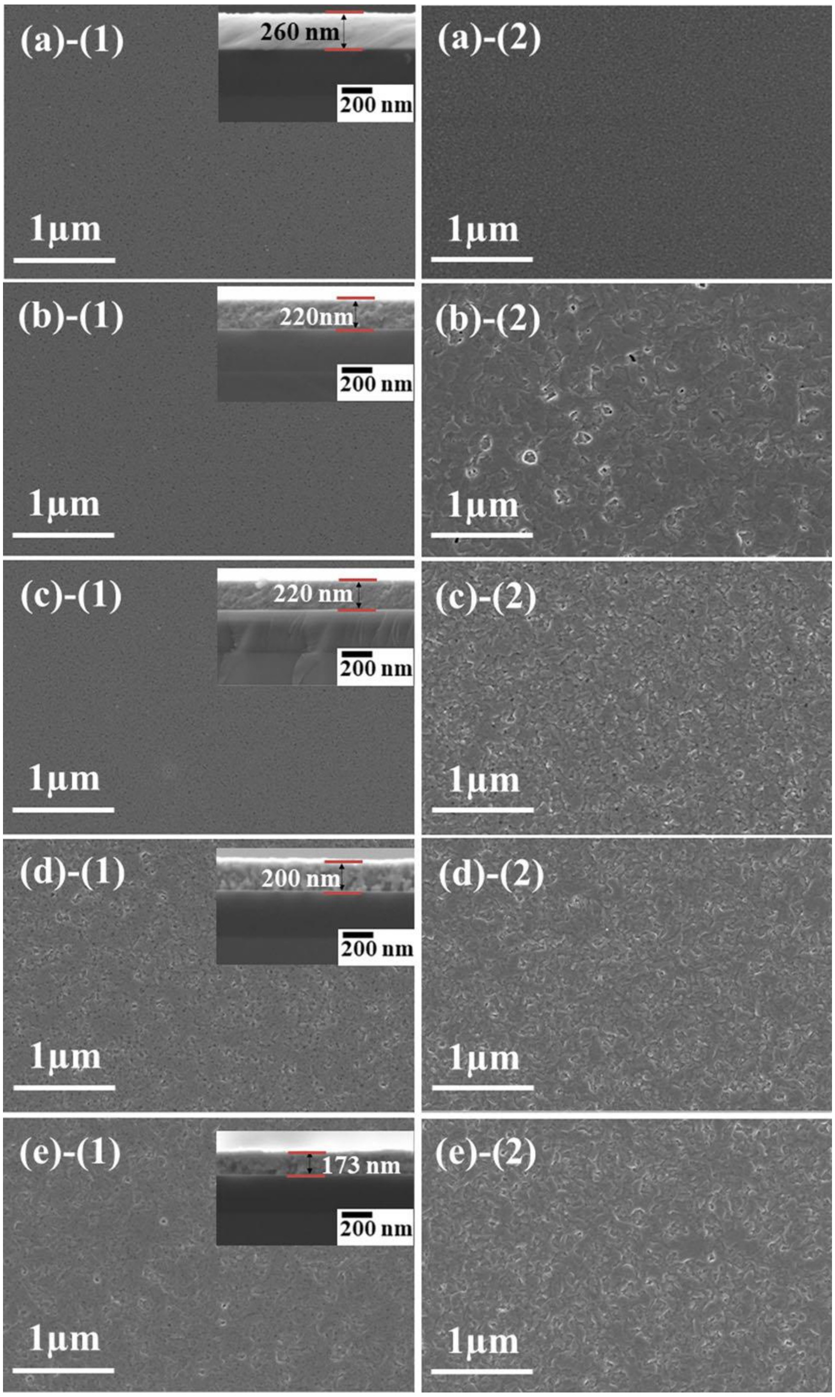

Figure 34 SEM images for surface morphology of AST thin films grown on (1) SO and (2) PI substrates: (a) as-deposited and annealed at (b)150°C, (c) 200°C, (d) 250°C, and (e) 300°C. Cross sections of thin films are inserted in the corresponding SEM images.

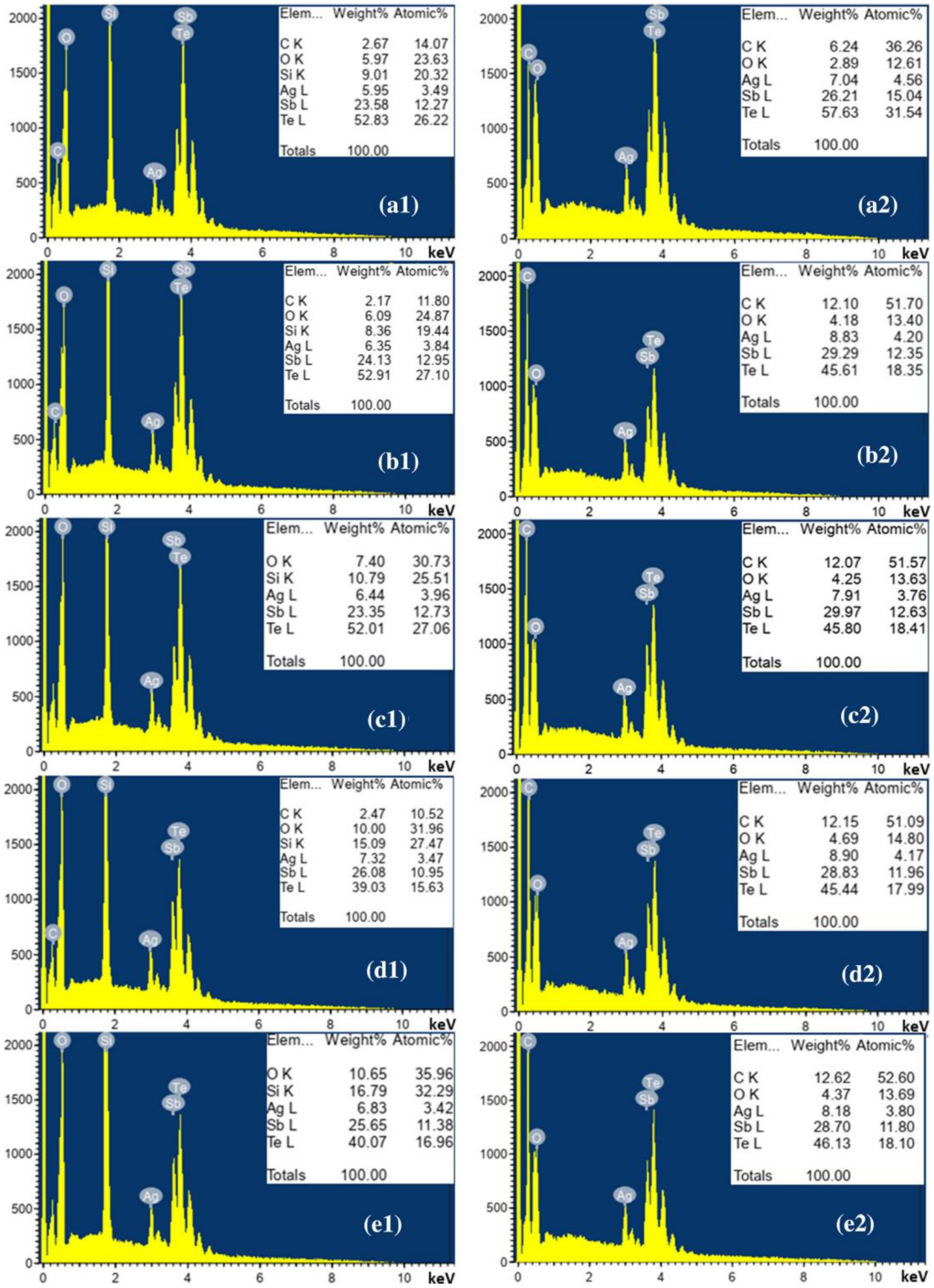

(a1)

| Elem... | Weight% | Atomic% |
|---|---|---|
| C K | 2.67 | 14.07 |
| O K | 5.97 | 23.63 |
| Si K | 9.01 | 20.32 |
| Ag L | 5.95 | 3.49 |
| Sb L | 23.58 | 12.27 |
| Te L | 52.83 | 26.22 |
| Totals | 100.00 | |

(a2)

| Elem... | Weight% | Atomic% |
|---|---|---|
| C K | 6.24 | 36.26 |
| O K | 2.89 | 12.61 |
| Ag L | 7.04 | 4.56 |
| Sb L | 26.21 | 15.04 |
| Te L | 57.63 | 31.54 |
| Totals | 100.00 | |

(b1)

| Elem... | Weight% | Atomic% |
|---|---|---|
| C K | 2.17 | 11.80 |
| O K | 6.09 | 24.87 |
| Si K | 8.36 | 19.44 |
| Ag L | 6.35 | 3.84 |
| Sb L | 24.13 | 12.95 |
| Te L | 52.91 | 27.10 |
| Totals | 100.00 | |

(b2)

| Elem... | Weight% | Atomic% |
|---|---|---|
| C K | 12.10 | 51.70 |
| O K | 4.18 | 13.40 |
| Ag L | 8.83 | 4.20 |
| Sb L | 29.29 | 12.35 |
| Te L | 45.61 | 18.35 |
| Totals | 100.00 | |

(c1)

| Elem... | Weight% | Atomic% |
|---|---|---|
| O K | 7.40 | 30.73 |
| Si K | 10.79 | 25.51 |
| Ag L | 6.44 | 3.96 |
| Sb L | 23.35 | 12.73 |
| Te L | 52.01 | 27.06 |
| Totals | 100.00 | |

(c2)

| Elem... | Weight% | Atomic% |
|---|---|---|
| C K | 12.07 | 51.57 |
| O K | 4.25 | 13.63 |
| Ag L | 7.91 | 3.76 |
| Sb L | 29.97 | 12.63 |
| Te L | 45.80 | 18.41 |
| Totals | 100.00 | |

(d1)

| Elem... | Weight% | Atomic% |
|---|---|---|
| C K | 2.47 | 10.52 |
| O K | 10.00 | 31.96 |
| Si K | 15.09 | 27.47 |
| Ag L | 7.32 | 3.47 |
| Sb L | 26.08 | 10.95 |
| Te L | 39.03 | 15.63 |
| Totals | 100.00 | |

(d2)

| Elem... | Weight% | Atomic% |
|---|---|---|
| C K | 12.15 | 51.09 |
| O K | 4.69 | 14.80 |
| Ag L | 8.90 | 4.17 |
| Sb L | 28.83 | 11.96 |
| Te L | 45.44 | 17.99 |
| Totals | 100.00 | |

(e1)

| Elem... | Weight% | Atomic% |
|---|---|---|
| O K | 10.65 | 35.96 |
| Si K | 16.79 | 32.29 |
| Ag L | 6.83 | 3.42 |
| Sb L | 25.65 | 11.38 |
| Te L | 40.07 | 16.96 |
| Totals | 100.00 | |

(e2)

| Elem... | Weight% | Atomic% |
|---|---|---|
| C K | 12.62 | 52.60 |
| O K | 4.37 | 13.69 |
| Ag L | 8.18 | 3.80 |
| Sb L | 28.70 | 11.80 |
| Te L | 46.13 | 18.10 |
| Totals | 100.00 | |

Figure 35 Atomic compositions of annealed AST thin films grown on (1) SO and (2) PI substrates: (a) as-deposited and annealed at (b) 150°C, (c) 200°C, (d) 250°C, and (e) 300°C.

SEM images show the surface morphology and thickness of the AST thin films grown on SO and PI substrates, as shown in Figure 34. The SEM images of as-deposited and annealed thin films correspond to (1) SO and (2) PI substrates (a) as-deposited, and annealed at (b) 150°C, (c) 200°C, (d) 250°C, and (e) 300°C. Cross-section images of thin films are inserted in corresponding SEM images. The as-deposited films demonstrate an exceptionally smooth and uniform surface morphology. It is observed that the thickness of the films decreased slightly from 260 nm (as deposited) to 173 nm (RTA at 300°C). The thickness of films decreases upon annealing due to the crystallization of material and partial re-evaporation of loosely bonded surface atoms at the high annealing temperature. Also, when the temperature of RTA increases, there is an evolution of flake-like surface morphology. The surface morphology of the as-deposited film illustrated a smooth surface, homogeneous morphology, and perfect adherence to the substrates. After the RTA, the morphologies of the thin films were different from that of the as-deposited sample with the grain growth and surface roughness increasing. These results confirmed that the as-deposited thin films were amorphous and then became crystalline after the temperature annealing, corresponding to the XRD results. The EDX spectra for the composition of AST thin films on both substrates are shown in Figure 35, corresponding to (1) SO and (2) PI substrates (a) as-deposited, and annealed (b) 150°C, (c) 200°C, (d) 250°C and (e) 300°C. EDX results demonstrate significant contributions from the film composed of elements Ag, Sb, and Te, along with minor contributions from C, Si, and O elements for the SO substrate and C and O elements for the PI substrate.

### Thermoelectric properties of AST Thin Film

The room-temperature thermoelectric properties ($S, \rho$ and $P$) of the AST thin films on SO and PI substrates are shown in Figure 36 as a function of RTA temperatures. The annealed AST thin films grown on both substrates exhibited p-type thermoelectricity. The films on SO substrates had higher S values than those of the films on PI substrates at annealing temperatures of 150°C to 250°C and then decreased slightly to exhibit similar values (of corresponding films grown on PI substrate) at an annealing temperature of 300°C. The q values of annealed thin films

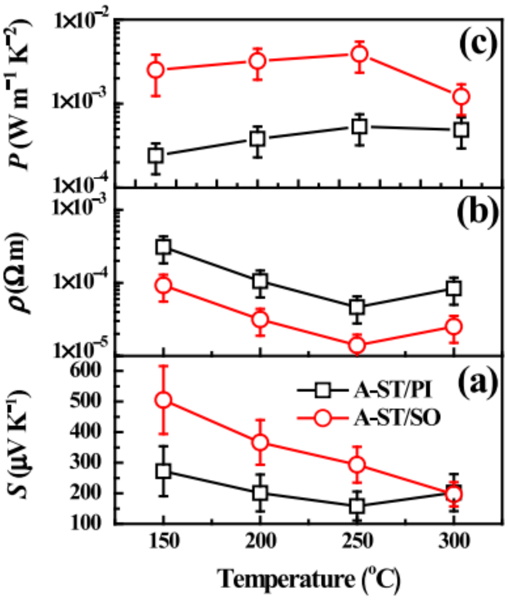

Figure 36 Thermoelectric properties: (a) S, (b) q, and (c) P values of AST thin films on SO and PI substrates as a function of the annealing temperature.

grown on SO substrates were lower than those of films grown on PI substrates for the entire range of annealing temperature. At an annealing temperature of 250°C, the lowest q values obtained for the thin films were $1.40 \times 10^{-5}$ Ω m and $4.65 \times 10^{-5}$ Ω m for the SO and PI substrates, respectively. At the same lowest electrical resistivity and annealing temperature, the AST thin films obtained a maximum power factor of 3.95 mW m$^{-1}$ K$^{-2}$ for the SO substrate and 0.53 mW m$^{-1}$ K$^{-2}$for the PI substrate. The obtained power factor values of the AST thin films grown on the PI substrate are found comparable to the reported power factor of flexible ST thin films.( VIEIRA, Eliana MF, et al. 2019) Moreover, the AST thin film on the SO substrate yielded power factors comparable to those reported for Ag-doped $Ge_2Sb_2Te_5$ thin film.( VORA-UD, Athorn, et al. 2019) Such interesting power factor values suggest that these films may be used in flexible thermoelectric devices. The thermoelectric properties of films deposited on the SO substrate are better than those on the PI substrate because they yield better phase quality (purity) in comparison to the case of the PI substrate, where the thermally unstable substrate induces the surface oxidation of Te atoms.

## AST THIN FILM DEPOSITED BY RF MAGNETRON SPUTTERING

### Crystal structure, morphology, and chemical composition of AST Thin Film

AST alloy thin film thermoelectric was added using a radio frequency magnetron sputtering system for thin film accretion. which consists of the thin film deposition process Characterization of thin films and the study of thermoelectric properties of thin films as follows:

In most of the applications, the substrate was rotational. However, the effect of substrate rotation on microstructure has not been clarified. (Thornton, J. A., 1974; Movchan, B. A., 2006 and Sun, Y., Lin, X., He, X., Zhang, et al., 2009).
The microstructure of inclined columns is generally found in prepared thermal barrier coatings and obliquely deposited or sputtered thin films. It causes anisotropy and strongly influences the crystallography and properties of the deposits. And the orientation of intercolumnar gaps is closely related to column inclination, which is of great concern for fabricating porous materials or thermal barrier coatings.
(Movchan, B. A., & Lemkey, F. D., 2003).

Figure 37 shows the microstructure and atomic composition of the as-deposited film as optimized by varying RF sputtering power to be applied to the target at 30 W, 50 W, 70 W, and 90 W. The microstructure and atomic composition of the as-deposited film were determined by XRD and EDX techniques. Figure 37 a presents the XRD results of as-deposited thin films showing amorphous behaviour, which is a common feature of sputtered material. The EDX results showed that the Ag atoms consisted of the film at a sputtering power of 50 W to be configured to optimize the Ag doping into $Sb_2Te_3$ as shown in Figure 37 b.

The power increase of 30, 50, 70, and 90W is the determination of the energy value that completes the chemical ratio of Ag-Sb-Te on the thin film. and, on the other hand, there may be no crystalline film at all. The results showed that the film obtained after baking was amorphous in phase. If we use it at all, it may cause the properties of TFTE to show unstable properties. because the film has a chance to crystallize at the temperature we use. So, we have to take the film to bake. To determine the temperature range and control the thermoelectric properties to the best of their ability before use.

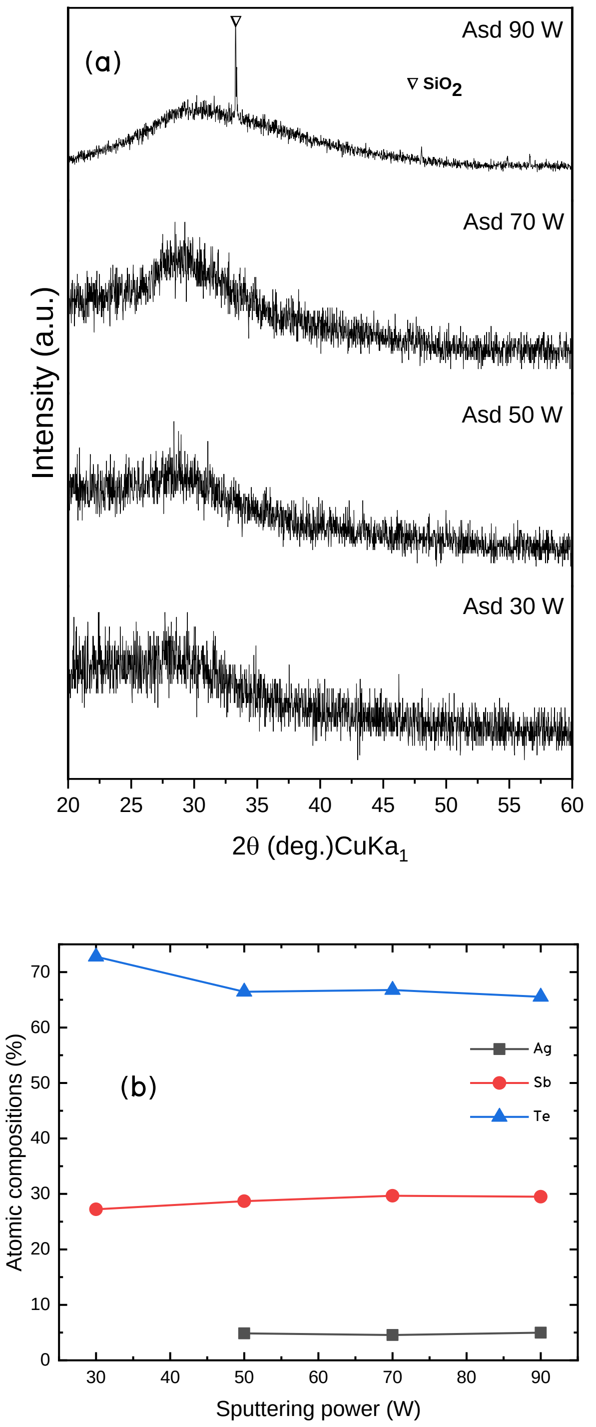

Figure 37 XRD analysis of AST thin films with RF power variation: (a) as-deposited and (b) atomic compositions.

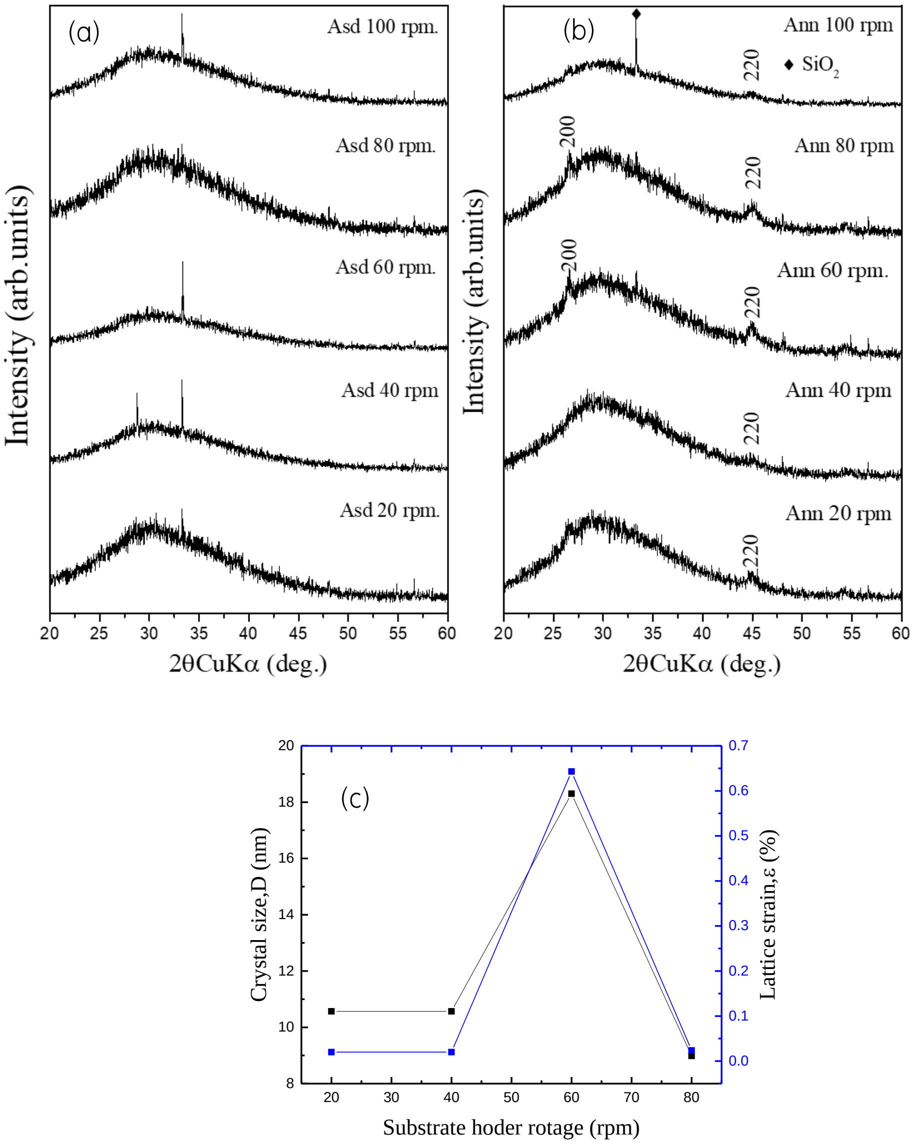

Figure 38 XRD analysis of AST thin films: (a) as deposited, (b) after annealing at 250°C for 8 min. and (c) Crystal size and Lattice strain.

Figure 38 demonstrates the findings of the X-ray diffraction (XRD) method analysis of the microstructures of AST thin films. Figure 33 (a) but when annealed rapid thermal annealed at 250°C for 8 min, X-ray diffraction of AST thin films revealed a phase transition from amorphous to crystal, which corresponded to the reference standard JCPDS 15-0540 (KIM, Jiwon, et al., 2016), indicating cubic crystallinity primarily at planes (200) and (220). The grain size of the deposited thin films was calculated using Debye-equation Scherrer's (D 14 k/B cos), and the results of 20 40 60 and 80 rpm for AST are 10.569, 10.568, 18.34, and 8.983 nm, respectively show in Figure 38 (c). The part at 100 rpm cannot be calculated, the meat from the XRD peak is very small.

Morphology and thickness of AST thin film as observed from photographs of Field Emission Scanning Electron Microscope; FESEM at 15 kV magnification Figure 39. Figure 39 show the morphology of AST thin film of 20 40 60 and 80 rpm through Annealing at 250 °C shows a smooth surface without specific morphological growth. And there are no pinholes or abnormal grain growth on the film surface that results in a tight film appearance if we look at the cross-section and film thickness obtained from the photograph (Zhao, Hai-Jing, et al., 2010). A cross-section of 170.057, 160.472, 155.58, 150.5, and 150.29 nm was measured with the Image J program. It was found that the higher the speed of the substrate holder, the lower the thickness of the thin film.

The chemical composition of the accretion thin film consisted of Ag atoms, Sb atoms, and Te atoms, with the atomic ratio Ag: Sb: Te% of 20 40 60 and 80 rpm with according to dispersive X-ray spectroscopy (EDS) Figure 40 technology. because each target material atom has a different average amount of coated target atom ejection for every single ion collision volume.

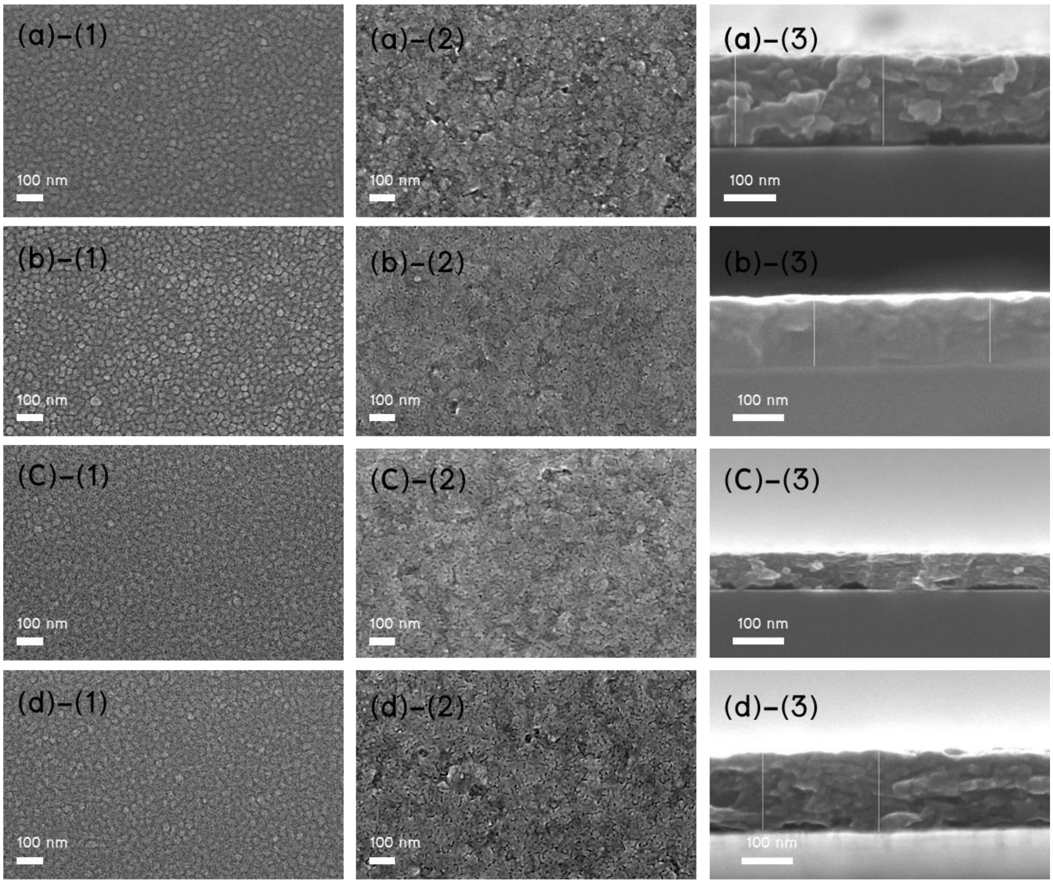

Figure 39 The SEM images AST surface morphology (1) as-deposited, (2) annealed, and (3) thin film cross sections: (a) 20 rpm (b) 40 rpm (c) 60 rpm (d) and 80 rpm.

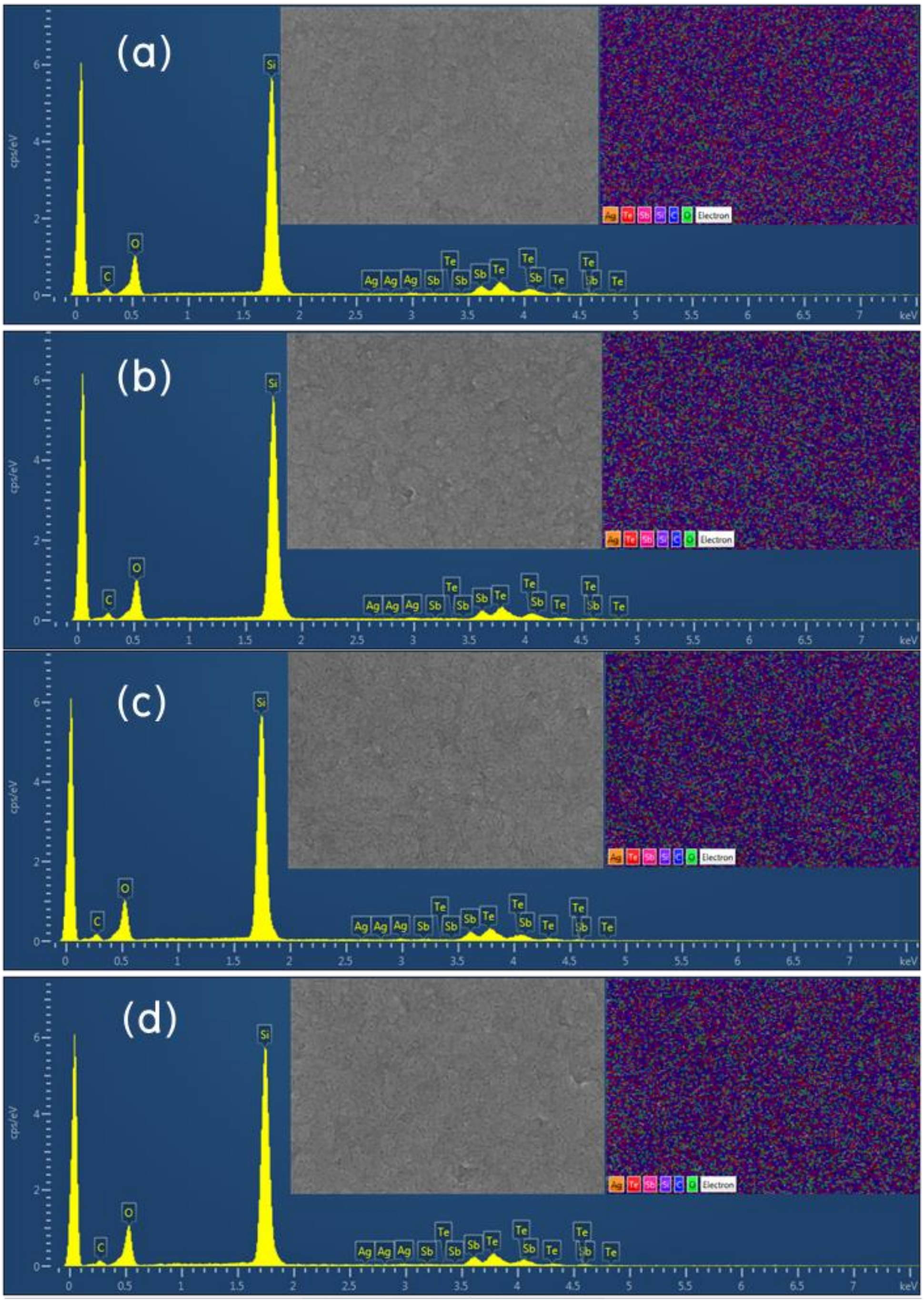

Figure 40 Atomic compositions of thin films after annealing of (a) 20 rpm., (b) 40 rpm., and (c) 80 rpm.

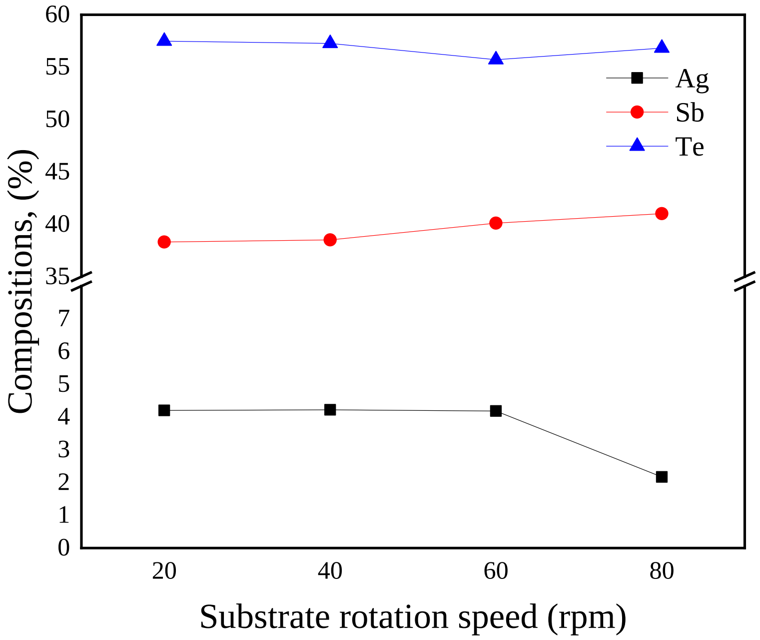

Figure 41 Atomic compositions of thin films after annealing.

## THERMOELECTRIC PROPERTIES OF AST THIN FILM

### Electrical resistivity of AST thin films

The electrical resistivity of the AST thin film is presented in Figure 42, as the rotation rate of the substrate holder at 20 rpm, 40 rpm, 60 rpm, and 80 rpm and annealed by RTA. The electrical resistivity of all the thin films increases with increasing temperature. The electrical resistivity of films at 100 °C thin film 20 rpm is less than other films at approximately $6.60 \times 10^{-6}$ Ωm, but temperature-increased samples at 60 rpm 150, 200, and 250°C have the lowest average resistivity at $7.74 \times 10^{-6}$ $8.7 \times 10^{-6}$ and $9.07 \times 10^{-6}$ Ω m respectively.

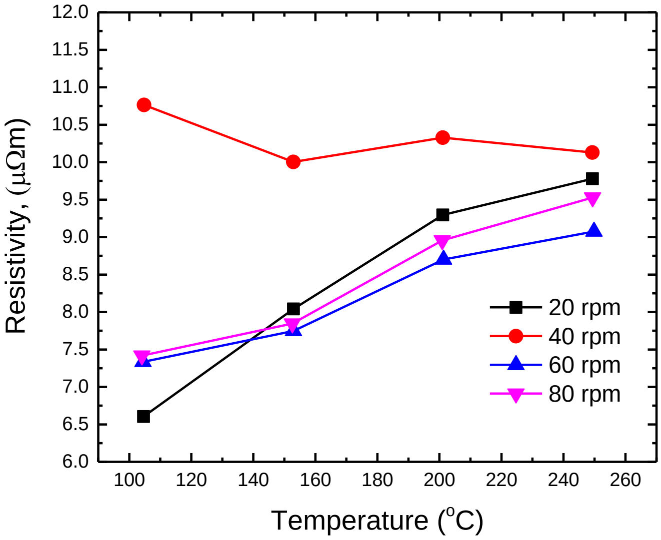

Figure 42 Measurements of Resistivity of the AST film with various temperatures.

### Seebeck coefficient of Ag Doped $Sb_2Te_3$ thin films

Figure 43 depicts the temperature dependence of the Seebeck coefficient (S) of an AST sample compared to the substrate holder rotation rate at 20, 40, 60, and 80 rpm as annealed by RTA. The Seebeck coefficient of all samples shows a positive value over the measured temperature range, indicating p-type conduction that the charge transport is dominated by defect electrons corresponding with the resultant samples (Du, Baoli, et al. 2016). The S value of the AST sample showed that it increased with increasing temperature. It was found that the highest Sebeck coefficient was 298.304 μV/K at a temperature of 100 °C for 60 rpm.

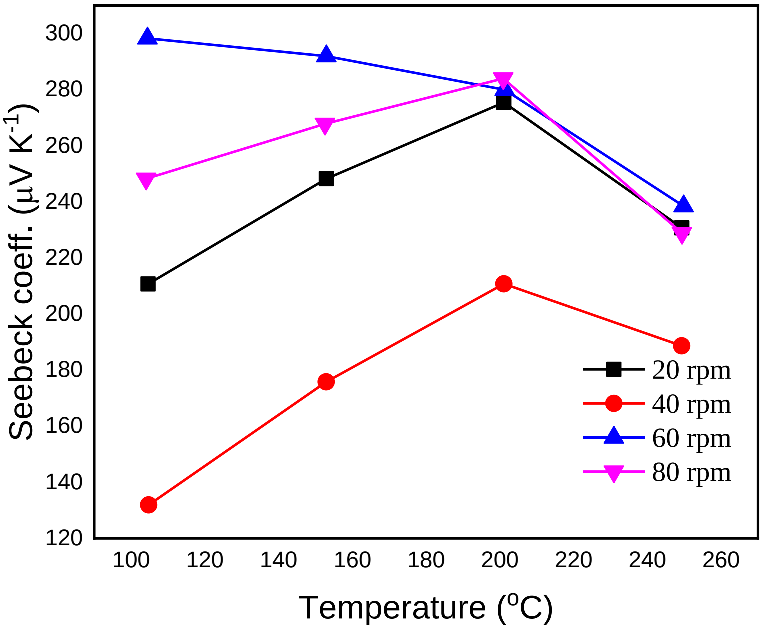

Figure 43 Measurements of Seebeck coefficient of the Ag-doped $Sb_2Te_3$ film with various temperatures.

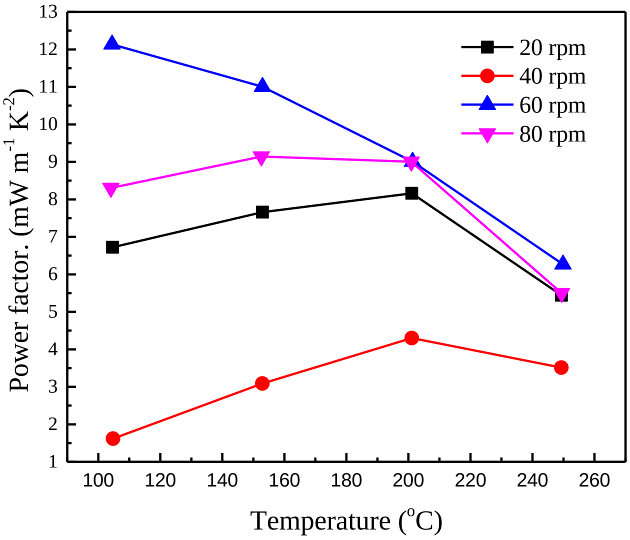

Figure 44 Measurements of power factor of the Ag-doped $Sb_2Te_3$ film with various temperatures.

### Power Factor of Ag Doped $Sb_2Te_3$ Thin Films

The power factor is one of the important thermoelectric parameters, that is defined as □□ = □$^{□}$/□. The power factor and Seebeck coefficient show a similar trend insofar as both trends show an initial increase followed by a decline in the 100-250 °C range. The power factor of the thin film substrate holder rotation rate at 40 rpm exhibited a lower power factor than other films and the maximum power factor value of 12.13 mW $m^{-1}$ $K^{-2}$ at 100 °C was 60 rpm as shown in Figure 44. Note that, the comparison of thermoelectric properties of Ag-doped $Sb_2Te_3$ thin film as optimized was presented in Figure 45. The results have been related to some noble metal doping for high performance of thermoelectric properties of thin film based.

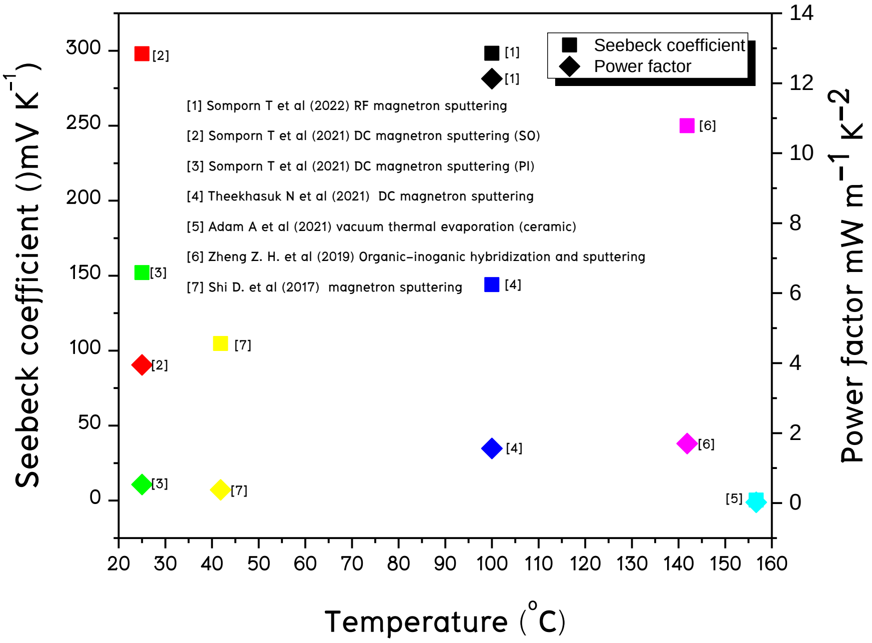

Figure 45 The comparison of thermoelectric properties of Ag-doped $Sb_2Te_3$ thin film with the literature data.

## THIN FILM THERMOELECTRIC MODULE

Development of a thin film thermoelectric module onto a generator based on two p-AST and n-BT thin films as compared between SO and PI. Then measure the electrical value of the thin film thermoelectric generator was shown in Figure 29. It was found that the open circuit electric potential difference of the thin film thermoelectric generator had a linear relationship with the increase in temperature differences. Figure 46 (a) shows the relationship between the temperature difference and the open-circuit potential difference of the thin film thermoelectric module on SO with a maximum open-circuit potential difference of 21.5 mV approximately at a temperature difference of 19.99 °C. The thin film thermoelectric module as fabricated on the PI substrate had a maximum open-circuit potential difference of 91.3 mV, approximately at a temperature difference of 80.052 °C as shown in Figure 46 (b).

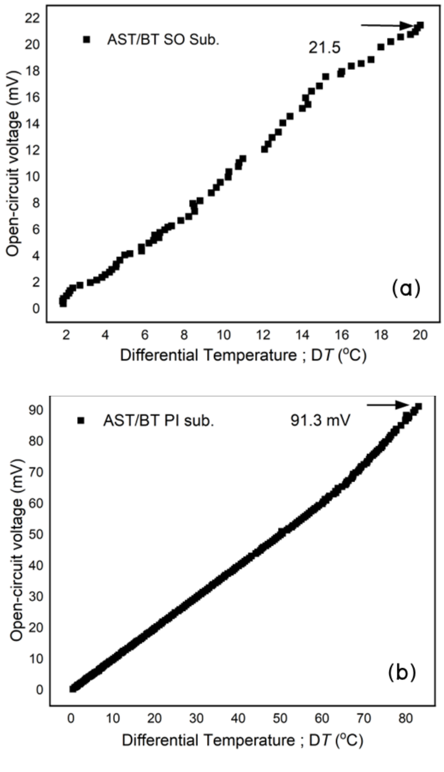

Figure 46 Results of p-AST and n-BT thin film thermoelectric generator' open-circuit potential measurements (a) SO and (b) PI.

Figure 47 (a) and (b) show the relationship between electric power, electric potential difference, and electric power of a thin film thermoelectric generator as compared between SO and PI, respectively. These results show the maximum power rating of 1.9 μW at a temperature difference of 19.99 °C for the thin film thermoelectric generator onto SO substrate and 23.647 μW at a temperature difference of 80.05 °C for the thin film thermoelectric generator onto PI substrate. From the result testing, it can be seen that the two materials have very large temperature differences, which is due to the large differences in the thermal conductivity of the substrate. Where SO has 1.4 W/mK (Clemens 2004) and PI has 0.16 W/mK (Du Pont 2022). It is evident that SO has a higher conductivity, thus allowing heat to flow through the material so that there is no temperature difference. that high, therefore resulting in less power output as well. Moreover, the comparison of thermoelectric power generation of Ag-doped $Sb_2Te_3$ thin film as optimized was presented in Figure 48. The results have been related to some devices for high-performance thermoelectric generators of thin film based.

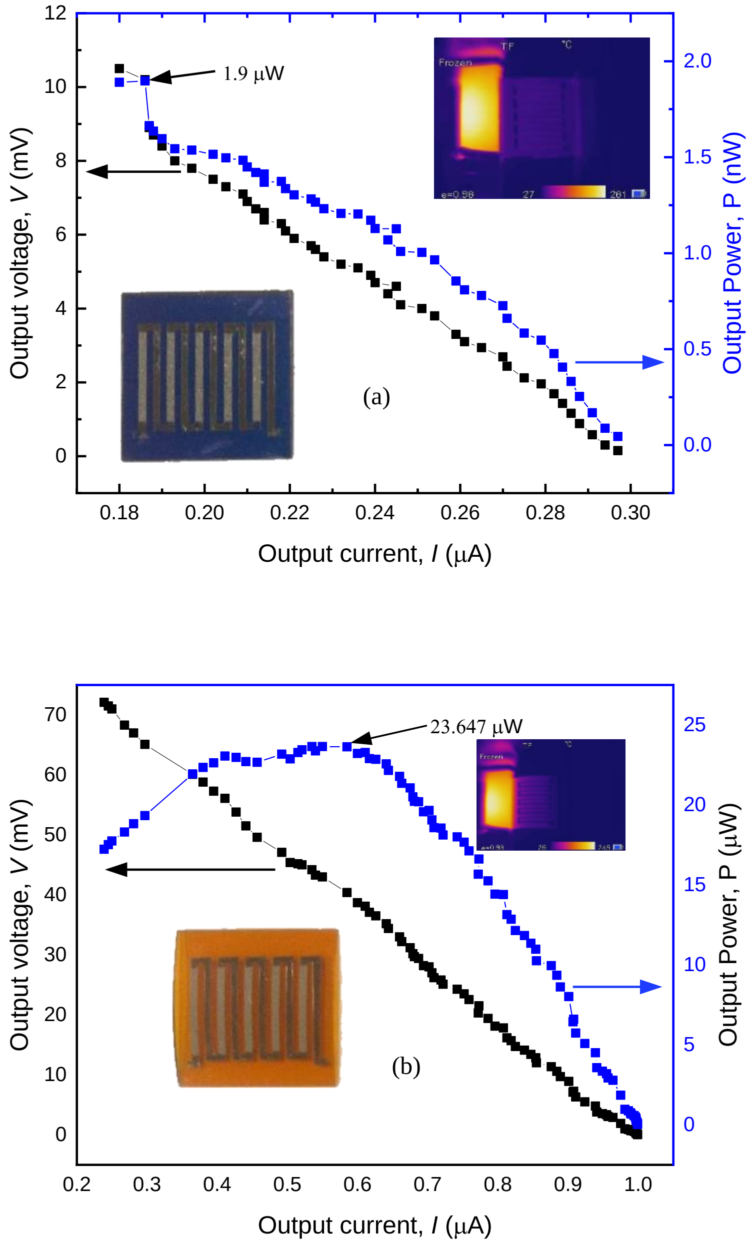

Picture 47 Results of p-AST and n-BT thin film thermoelectric generator' electrical Power measurements (a) SO and (b) PI

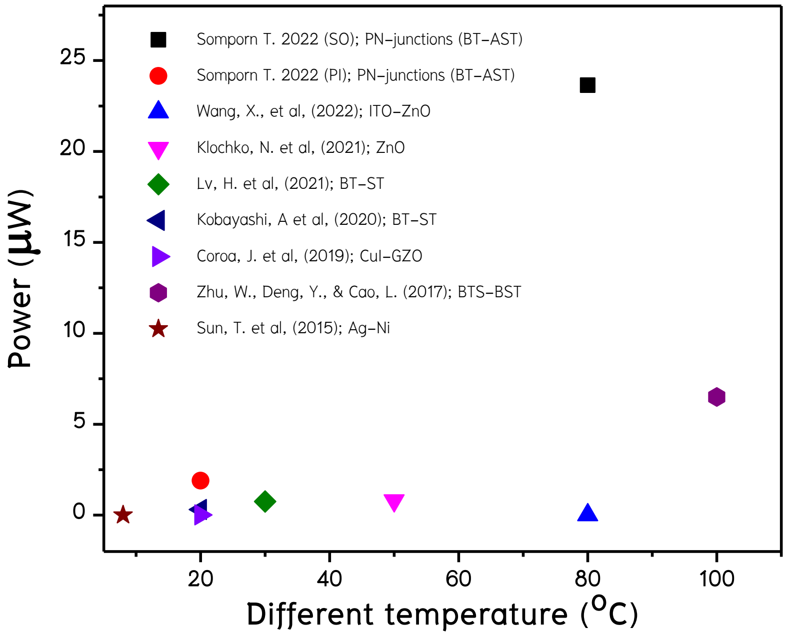

Figure 48 The comparison of thermoelectric generator of Ag-doped $Sb_2Te_3$ thin film with the literature data.

# CHAPTER 5

## CONCLUSIONS AND SUGGESTIONS

This chapter is the conclusion of the thesis on the synthesis AST thin film using the magnetron sputtering method and the fabrication thin film thermoelectric module of AST as matched with BT material. Conclusions and suggestions based on the finding of this thesis are as follow:

### CONCLUSION

Firstly, A-ST thin films were synthesized on 1-lm $SiO_2$/ Si-wafer and polyimide substrates by DC magnetron sputtering. The effect of the post-deposition RTA process on the microstructural and thermoelectric properties of the A-ST thin films was studied and presented. At room temperature, the maximum power factor of the A-ST thin film on the SO substrate (3.95 mW $m^{-1}$ $K^{-2}$) was found to be greater than that on the PI substrate (0.53 mW $m^{-1}$ $K^{-2}$), and roughly around 3.42 mW $m^{-1}$ $K^{-2}$ for RTA at 250°C.

Secondly, AST thin films were synthesized on SO substrates by RF magnetron sputtering. The effect of Substrate holder rotation rate at 20 40 60 and 80 rpm. The Crystal structure of AST film corresponded to the reference standard JCPDS 15-0540. thermoelectric properties of AST: The electrical resistivity of films at 100°C thin film 20 rpm is less than other films these were approximately $6.60 \times 10^{-6}$ Ωm, Seebeck coefficient of all samples shows a positive value over the measured temperature range, indicating the p-type conduction. it increased with increasing temperature. It was found that the highest Sebeck coefficient was 301.3 μV/K at 150°C. and maximum power factor value of 12.13 mW $m^{-1}$ $K^{-2}$ at 100 °C of 60 rpm. respectively.

Thirdly, the thermoelectric generator is fabricated of *p*- Ag Doped $Sb_2Te_3$ (A-ST) Thin films and *n*-$Bi_2Te_3$ (BT) arrays with a are deposited as *n*-type and *p*-type legs junction thermoelectric materials onto hard and soft substrate There is an open circuit electric potential difference of a thin film thermoelectric generator. The maximum open-circuit potential difference was 21.5 mV and 91.3 mV, and the power was 1.9 μW and 23.06 μW at a temperature difference of 19.99 $^{o}C$ and 80.05 $^{o}C$, respectively.

## SUGGESTION

1. For fabrication thin film thermoelectric module of AST matches with BT, a substrate should be low thermal conductivity for enhancing the efficiency of the module.

2. Measurement of the module in order not to destroy the terminal should be an Ag sheet connected to the electrode module.

# REFERENCES

# REFERENCES

Adachi, H., & Wasa, K. (2012). *Thin films and nanomaterials*. Handbook of Sputter Deposition Technology: Fundamentals and Applications for Functional Thin Films, Nano-Materials and MEMS:, 3-39.

Adam, A. M., Elsehly, E. M., Ataalla, M., El-Khouly, A., Nafady, A., & Diab, A. K. (2021). Preparation and thermoelectric power properties of highly doped p-type Sb2Te3 thin films. *Physica E: Low-dimensional Systems and Nanostructures*, 127, 114505.

Bel Hadj Tahar, R., Ban, T., Ohya, Y., & Takahashi, Y. (1998). Tin doped indium oxide thin films: Electrical properties. *Journal of Applied Physics, 83*(5), 2631-2645.

Bell, L. E. (2008). Cooling, heating, generating power, and recovering waste heat with thermoelectric systems. *Science, 321*(5895), 1457-1461.

Behrisch, R., & Wittmaack, K. (Eds.). (1981). Sputtering by particle bombardment. *Springer-Verlag, 1*, 9-64.

Bender, M., Trube, J., & Stollenwerk, J. (1999). Deposition of transparent and conducting indium-tin-oxide films by the rf-superimposed DC sputtering technology. *Thin Solid Films, 354*(1-2), 100-105.

Bunshah, R. F. (1982). *Deposition technologies for films and coatings: developments and applications*. Park Ridge, N.J., U.S.A.: Noyes Publications.

Bhansali, S. (2017). *Thermoelectric properties of oxides and related materials.* Doctoral thesis in Physics (Materials Sciences), Universitat Autonoma de Barcelona.

Bao, M. H. (2000). *Micro mechanical transducers: pressure sensors, accelerometers and gyroscopes*. New York: Elsevier.

Chapman, B., & Vossen, J. L. (1981). Glow discharge processes: sputtering and plasma etching. *Physics Today, 34*(7), 62.

Carl, K., Schmitt, H., & Friedrich, I. (1997). Optimization of sputtered ITO films with respect to the oxygen partial pressure and substrate temperature. *Thin Solid Films, 295*(1-2), 151-155.

Chen, G. (2001). Phonon transport in low dimensional. *Semicond Semimetals, 71*, 203.

Chopra, K. L. (1969). *Thin Film Phenomena.* New York: McGraw-Hill Book Company.

Denmark, T. U. o. (2014). *Introduction of Thermoelectric.* Retrieved from http://www.otepower.dk/introduction. October 1st, 2022.

Du, B., Liu, M., Xu, J., Hu, B., Liu, B., Su, T., & Wang, J. (2018). Thermodynamic, structural and thermoelectric properties of $AgSbTe_2$ thick films developed by melt spinning. *Nanomaterials, 8*(7), 474.

DuPont™ Kapton® HN / (2022)./ Kapton HN Thermal Insulating Film/ 1-10-2022 / https://uk.rs-online.com/web/p/plastic-ilm/5363968?fbclid=IwAR32x3RsRt7BI6DreAuRcRF40F-vWM4ZB-7XRQ9Rvs0nrSf3np-4fWP15sE

Macia, E. (Ed.). (2015). *Thermoelectric materials: advances and applications.* n.p.: Pan Stanford Publishing.

McKeen, L. W. (2017). Film properties of plastics and elastomers. n.p.: William Andrew.

Enescu, D. (2019). Thermoelectric energy harvesting: basic principles and applications. *Green energy advances*, 1.

Ellmer, K. (2000). Magnetron sputtering of transparent conductive zinc oxide: relation between the sputtering parameters and the electronic properties. *Journal of Physics D: Applied Physics, 33*(4), R17.

Elshabini, A., Elshabini-Riad, A., Barlow, F. D., & Barlow, F. D. (1998). Thin film technology handbook. New York: McGraw Hill.

Energy.com, C. (2013). *WASTE HEAT RECOVERY.* Retrieved from http://coolenergy.com/waste-heat-recovery/. October 1st, 2022.

Fourmont, P., Gerlein, L. F., Fortier, F. X., Cloutier, S. G., & Nechache, R. (2018). Highly efficient thermoelectric microgenerators using nearly room temperature pulsed laser deposition. *ACS applied materials & interfaces, 10*(12), 10194 - 10201.

Hamberg, I., & Granqvist, C. G. (1986). Evaporated Sn-doped In2O3 films: Basic optical properties and applications to energy-efficient windows. *Journal of Applied Physics, 60*(11), R123-R160.

Harman, T. C., Taylor, P. J., Walsh, M. P., & LaForge, B. E. (2002). Quantum dot superlattice thermoelectric materials and devices. *science, 297*(5590), 2229-2232.

Huang, B., & Kaviany, M. (2010). Filler-reduced phonon conductivity of thermoelectric skutterudites: Ab initio calculations and molecular dynamics simulations. *Acta Materialia, 58*(13), 4516-4526.

Harman, T. C., Walsh, M. P., & Turner, G. W. (2005). Nanostructured thermoelectric materials. *Journal of electronic materials, 34*(5), L19-L22.

Hass, G., Francombe, M. H., & Hoffman, R. W. (Eds.). (2013). Physics of thin films: Advances in research and development. n.p.: Academic press, Inc.

Heremans, J. P., Jovovic, V., Toberer, E. S., Saramat, A., Kurosaki, K., Charoenphakdee, A., ... & Snyder, G. J. (2008). Enhancement of thermoelectric efficiency in PbTe by distortion of the electronic density of states. *Science, 321*(5888), 554-557.

Huang, B., & Kaviany, M. (2010). Filler-reduced phonon conductivity of thermoelectric skutterudites: Ab initio calculations and molecular dynamics simulations. *Acta Materialia, 58*(13), 4516-4526.

Holland, L. (1970). *Vacuum deposition of thin films.* London: Chapman & Hall.

https://showcase.ulvac.co.jp/en/products/heat-treatment-and-thermal-properties/thermoelectric-evaluation-device/thermoelectric-properties/zem-3series.html. October 1st, 2022.

https://cipherengineers.com/shop/kapton-film-304x200x0-075mm. October 1st, 2022.

Janssen, G. J. (2015). Information on the FESEM (Field-emission Scanning Electron Microscope). Radboud University Nijmegen. microgenerators using nearly room temperature pulsed laser deposition. *ACS Appl. Mater. Interfaces 2018,* 10(12), 10194-10201.

Karthikeyan, V., Surjadi, J. U., Wong, J. C., Kannan, V., Lam, K. H., Chen, X., ... & Roy, V. A. (2020). Wearable and flexible thin film thermoelectric module for multi-scale energy harvesting. *Journal of Power Sources, 455*, 227983.

Jarzebski, A. Z. (1982). Preparation and physical properties of transparent conducting oxide films. *Physica status solidi (a), 71*(1), 13–41.

Khumtong, T., Sakulkalavek, A., & Sakdanuphab, R. (2017). Empirical modelling and optimization of pre-heat temperature and Ar flow rate using response surface methodology for stoichiometric Sb2Te3 thin films prepared by RF magnetron sputtering. *Journal of Alloys and Compounds, 715*, 65–72.

Kim, H., Kaviany, M., Thomas, J. C., Van der Ven, A., Uher, C., & Huang, B. (2010). Structural order-disorder transitions and phonon conductivity of partially filled skutterudites. *Physical review letters, 105*(26), 265901.

Kim, J., Lee, J. Y., Lim, J. H., & Myung, N. V. (2016). Optimization of thermoelectric properties of p-type $AgSbTe_2$ thin films via electrochemical synthesis. *Electrochimica Acta, 196*, 579–586.

Kim, S. J., Lee, H. E., Choi, H., Kim, Y., We, J. H., Shin, J. S., ... & Cho, B. J. (2016). High-performance flexible thermoelectric power generator using laser multiscanning lift-off process. *ACS nano, 10*(12), 10851-10857.

Kim, S. J., Choi, H., Kim, Y., We, J. H., Shin, J. S., Lee, H. E., ... & Cho, B. J. (2017). Post ionized defect engineering of the screen-printed Bi2Te2. 7Se0. 3 thick film for high performance flexible thermoelectric generator. *Nano Energy, 31*, 258–263.

KIYOTAKA W. (1992). *Handbook of sputter deposition technology: Principles, technology, and applications*, New Jersey: noyes publications.

Le, P. H.; Liao, C. N.; Luo, C. W.; Leu, J., (2014). Thermoelectric properties of nanostructured bismuth–telluride thin films grown using pulsed laser deposition. *Journal of Alloys and Compounds, 615*, 546–552.

Le, P. H.; Luo, C. W.; Leu, J., (2016). Thermoelectric properties of nanocrystalline Bi3Se2Te thin films grown using pulsed laser deposition. *Journal of Alloys and Compounds, 673*, 107–114.

Lowrie, W., & Fichtner, A. (2020). *Fundamentals of geophysics*. UK: Cambridge university press.

Li Bassi, A.; Bailini, A.; Casari, C. S.; Donati, F.; Mantegazza, A.; Passoni, M.; Russo, V.; Bottani, C. E., (2009). Thermoelectric properties of Bi–Te films with controlled structure and morphology. *J. Appl. Phys., 105*(12), 124307.

Lv, B., Hu, S., Li, W., Di, X., Feng, L., Zhang, J., ... & Lei, Z. (2010). Preparation and characterization of thin films by coevaporation. *International journal of photoenergy*, 2010, 1-4. https://doi.org/10.1155/2010/476589.

Maissel, L. I., Glang, R., & Budenstein, P. P. (1971). Handbook of thin film technology. *Journal of The Electrochemical Society, 118*(4), 114C.

Mergel, D., Schenkel, M., Ghebre, M., & Sulkowski, M. (2001). Structural and electrical properties of In2O3: Sn films prepared by radio-frequency sputtering. *Thin Solid Films, 392*(1), 91-97.

Meng, L. J., & Dos Santos, M. P. (1996). Structure effect on electrical properties of ITO films prepared by RF reactive magnetron sputtering. T*hin Solid Films, 289*(1-2), 65-69.

Movchan, B. A., & Lemkey, F. D. (2003). Some approaches to producing microporous materials and coatings by EB PVD. *Surface and Coatings Technology, 165*(1), 90-100.

Mu, E., Yang, G., Fu, X., Wang, F., & Hu, Z. (2018). Fabrication and characterization of ultrathin thermoelectric device for energy conversion. *Journal of Power Sources, 394*, 17-25.

Overview, D. D. (2013). Advanced X-ray Diffraction System for Materials Research Applications. n.p.

Paine, D. C., Whitson, T., Janiac, D., Beresford, R., Yang, C. O., & Lewis, B. (1999). A study of low temperature crystallization of amorphous thin film indium–tin–oxide. *Journal of Applied Physics, 85*(12), 8445-8450.0

Pandian, M. S. (2014). X-ray diffraction analysis: Principle, Instrument and Application. *Pondicherry University Puducherry*, INDIA, 34.

Price, S. H. (2007). *The Peltier Effect and Thermoelectric Cooling.* Retrieved from WWW-dokumentti. Saatavilla: http://ffden-2. phys. uaf. edu/212_spring2007. dir/sedona_price/phys_212_webproj_peltier. html [viitattu 20.5. 2017]. September 25th, 2022.

Qiao, Z. (2003). Fabrication and study of ITO thin films prepared by magnetron sputtering (Doctoral dissertation, Duisburg, Essen, Univ. Diss., 2003).

Ramaiah, K. S., Raja, V. S., Bhatnagar, A. K., Tomlinson, R. D., Pilkington, R. D., Hill, A. E., ... & Juang, F. S. (2000). Optical, structural and electrical properties of tin doped indium oxide thin films prepared by spray-pyrolysis technique. *Semiconductor science and technology, 15*(7), 676.

Rossnagel, S. M., Cuomo, J. J., & Westwood, W. D. (Eds.). (1990). *Handbook of plasma processing technology: fundamentals, etching, deposition, and surface interactions*. n.p.: William Andrew.

Rowe, D. M. (2005). *Thermoelectrics handbook: macro to nano*. Boca Raton: CRC press.

Seymour J, (1972). *Physical Electronics*, Pitman, pp 53–54 34.

Shakouri, A., & Zebarjadi, M. (2009). Nanoengineered materials for thermoelectric energy conversion *Thermal Nanosystems and Nanomaterials* (pp. 225-299): Springer.

Smith, D. (1972). Physical Electronics. *Students' Quarterly Journal*, *42*(169), 78.

Somdock, N., Harnwunggmoung, A., Sakulkalavek, A., & Sakdanuphab, R. (2019). Effect of real working environment/formation of oxide phase on thermoelectric properties of flexible $Sb_2Te_3$ films. *Ceramics International, 45*(13), 15860-15865.

Spies, P., Pollak, M., & Mateu, L. (Eds.). (2015). *Handbook of energy harvesting power supplies and applications*. Boca Raton: CRC Press.

Seetawan, T., Amornkitbamrung, V., Burinprakhon, T., Maensiri, S., Tongbai, P., Kurosaki, K., ... & Yamanaka, S. (2006). Effect of sintering temperature on the thermoelectric properties of NaxCo2O4. *Journal of alloys and compounds, 416*(1-2), 291-295.

Shakouri, A. (2006). Nanoscale thermal transport and microrefrigerators on a chip. *Proceedings of the IEEE, 94*(8), 1613-1638.

Somkhunthot, W., Burinprakhon, T., Seetawan, T., & Amornkitbamrung, V. (2007). Bipolar pulsed-DC power supply for magnetron sputtering and thin films synthesis. *Elektrika Journal of Electrical Engineering, 9*(2), 20-26.

Sootsman, J. R., Chung, D. Y., & Kanatzidis, M. G. (2009). New and old concepts in thermoelectric materials. *Angewandte Chemie – International Edition*, *48*(46), 8616–8639. https://doi.org/10.1002/anie.200900598.

Snyder, G. J., & Snyder, A. H. (2017). Figure of merit ZT of a thermoelectric device defined from materials properties. *Energy & Environmental Science*, *10*(11), 2280–2283.

Sun, Y., Lin, X., He, X., Zhang, J., Li, M., Song, G., ... & Zhao, Y. (2009). Effects of substrate rotation on the microstructure of metal sheet fabricated by electron beam physical vapor deposition. *Applied surface science, 255*(11), 5831 – 5836.

Tian, R., Wan, C., Wang, Y., Wei, Q., Ishida, T., Yamamoto, A., ... & Koumoto, K. (2017). A solution-processed TiS 2/organic hybrid superlattice film towards flexible thermoelectric devices. *Journal of Materials Chemistry A, 5*(2), 564–570.

Trigo, M., Bruchhausen, A., Fainstein, A., Jusserand, B., & Thierry-Mieg, V. (2002). Confinement of acoustical vibrations in a semiconductor planar phonon cavity. *Physical review letters, 89*(22), 227402.

Thornton, J. A. (1974). Influence of apparatus geometry and deposition conditions on the structure and topography of thick sputtered coatings. *Journal of Vacuum Science and Technology, 11*(4), 666–670.

Venkatasubramanian, R., Siivola, E., Colpitts, T., & O'quinn, B. (2001). Thin-film thermoelectric devices with high room-temperature figures of merit. *Nature, 413*(6856), 597–602.

Vieira, E. M., Figueira, J., Pires, A. L., Grilo, J., Silva, M. F., Pereira, A. M., & Goncalves, L. M. (2019). Enhanced thermoelectric properties of Sb2Te3 and Bi2Te3 films for flexible thermal sensors. *Journal of Alloys and Compounds, 774,* 1102–1116.

Vora-ud, A., Horprathum, M., Kumar, M., Muthitamongkol, P., Chananonnawathorn, C., Saekow, B., ... & Seetawan, T. (2019). Effect of Ag mixing in thermoelectric $Ge_2Sb_2Te_5$ thin films. *Materials Letters, 234*, 229–232.

Wasa, K., & Hayakawa, S. (1992). *Handbook of sputter deposition technology.* United States: Noyes Publications.

Wang, W., Ji, Y., Xu, H., Li, H., Visan, T., & Golgovici, F. (2013). A high packing density micro-thermoelectric power generator based on film thermoelectric materials fabricated by electrodeposition technology. *Surface and Coatings Technology, 231*, 583-589.

Yao, J. L., Hao, S., & Wilkinson, J. S. (1990). Indium tin oxide films by sequential evaporation. *Thin Solid Films, 189*(2), 227-233.

Yi, C. H., SHIGEsAo, Y., Yasui, I., & Takaki, S. (1995). Microstructure of Low-Resistivity Tin-Doped Indium Oxide Films Deposited. Jpn. J. Appl. Phys, 34(2B Pt 2).

Zhao, H. J., Yao, M., Chen, Q., Wang, D., & Wan, L. J. (2010). Theoretical understanding of adlayer structure, thermal stability and electronic property of graphene molecules. *Surface science, 604*(23-24), 2091-2097.

# APPENDICE

# APPENDICE A

# DATA OF BT THERMOELECTRIC THIN FILM

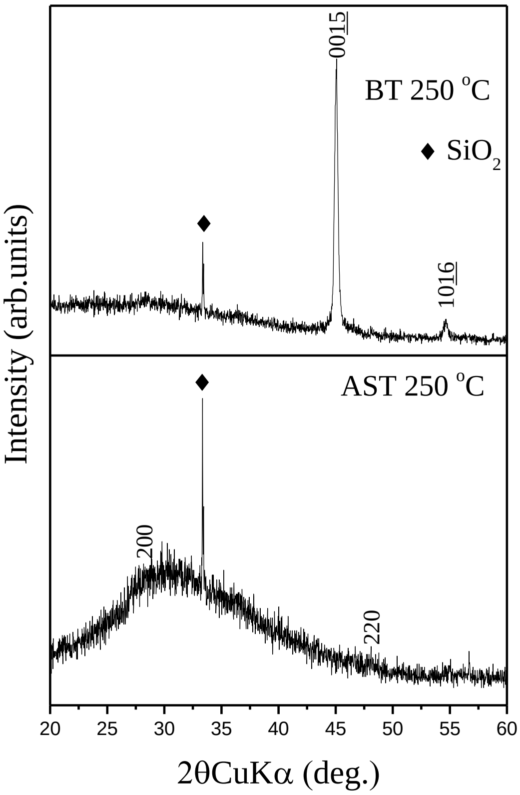

XRD patterns of thin films as grown on SO (a) BT and (b) AST

Thermoelectric properties of BT thin film.

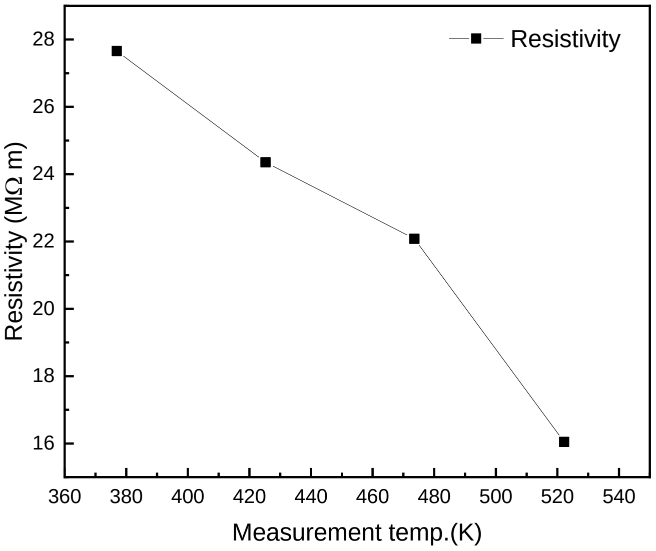

Measurements of Resistivity of the BT film with various temperatures.

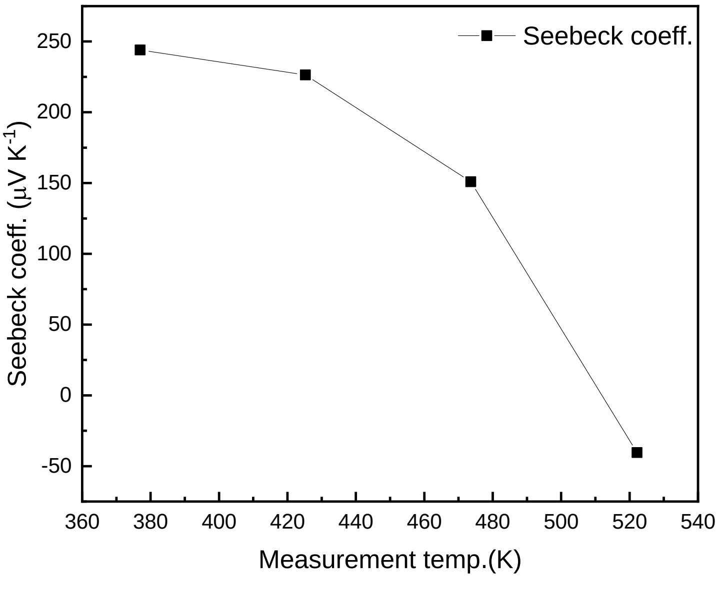

Measurements of Seebeck coeffciant of the BT film with various temperatures.

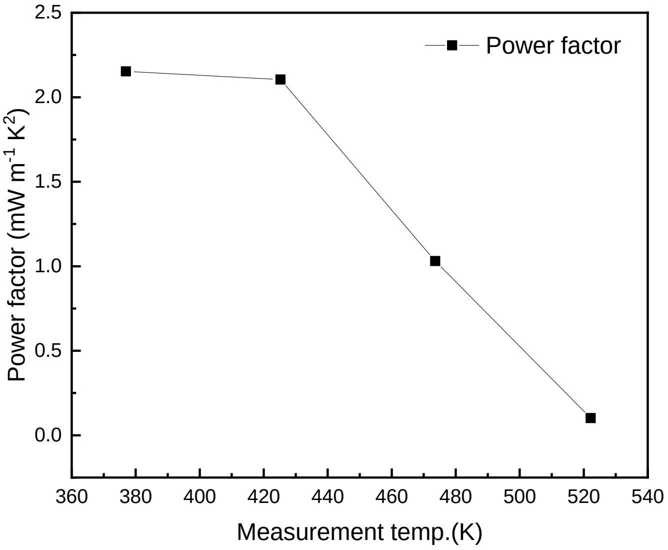

Measurements of Seebeck coeffciant of the BT film with various temperatures.

# APPENDICE B

# DATA OF THIN FILM THERMOELECTRIC MODULE

Table 1 Data of p-AST and n-BT thin film thermoelectric generator open-circuit on PI.

| I | | | | II | | | |
|---|---|---|---|---|---|---|---|
| $T_c$ ($^{o}$C) | $T_h$ ($^{o}$C) | $\Delta$T ($^{o}$C) | $V_{open}$ (mV) | $T_c$ ($^{o}$C) | $T_h$ ($^{o}$C) | $\Delta$T ($^{o}$C) | $V_{open}$ (mV) |
| 24.8 | 25.41 | 0.492 | 0.4 | 25.87 | 34.75 | 12.528 | 12.6 |
| 24.85 | 25.6 | 0.942 | 0.9 | 25.6 | 35.26 | 13.575 | 13.5 |
| 24.88 | 25.84 | 1.26 | 1.1 | 25.18 | 36.6 | 14.19 | 14 |
| 24.89 | 25.94 | 1.527 | 1.4 | 25.04 | 35.65 | 14.419 | 14.3 |
| 24.92 | 26.2 | 1.635 | 1.7 | 25.85 | 35.84 | 14.771 | 14.6 |
| 24.95 | 26.42 | 2.08 | 2 | 24.78 | 35.9 | 15.086 | 15 |
| 24.96 | 26.58 | 2.254 | 2.2 | 24.49 | 36.02 | 15.478 | 15.4 |
| 24.97 | 26.7 | 2.533 | 2.5 | 24.19 | 36.18 | 15.758 | 15.8 |
| 25.02 | 27 | 2.982 | 2.9 | 23.97 | 36.32 | 16.203 | 16.1 |
| 25.06 | 27.24 | 3.345 | 3.3 | 23.61 | 36.36 | 16.707 | 16.5 |
| 25.08 | 27.41 | 3.622 | 3.6 | 23.28 | 36.48 | 17.067 | 16.9 |
| 25.11 | 27.66 | 3.831 | 3.9 | 22.94 | 36.59 | 17.54 | 17.4 |
| 25.14 | 27.96 | 4.296 | 4.3 | 22.47 | 36.68 | 18.076 | 18 |
| 25.16 | 28.08 | 4.596 | 4.5 | 22.17 | 36.64 | 18.331 | 18.3 |
| 25.17 | 28.25 | 4.91 | 4.8 | 22 | 36.8 | 18.759 | 18.6 |
| 25.2 | 28.38 | 5.14 | 5.1 | 21.84 | 36.93 | 19.235 | 19 |
| 25.22 | 28.71 | 5.476 | 5.4 | 21.59 | 36.99 | 19.523 | 19.4 |
| 25.25 | 29.02 | 5.725 | 5.7 | 21.52 | 37 | 19.874 | 19.7 |
| 25.3 | 89.35 | 6.206 | 6 | 21.52 | 37.14 | 20.027 | 20 |
| 25.36 | 29.69 | 6.645 | 6.3 | 21.43 | 37.49 | 20.558 | 20.5 |
| 25.38 | 29.81 | 6.747 | 6.7 | 21.38 | 37.92 | 21.143 | 21 |
| 25.44 | 30.22 | 7.053 | 7 | 21.4 | 38.17 | 21.635 | 21.5 |
| 25.5 | 30.62 | 7.374 | 7.2 | 21.57 | 38.74 | 21.925 | 22 |
| 25.56 | 30.88 | 7.642 | 7.6 | 21.74 | 39.19 | 22.548 | 22.5 |
| 25.62 | 31.13 | 7.899 | 7.9 | 21.87 | 39.47 | 23.078 | 23 |
| 25.7 | 13.51 | 8.337 | 8.3 | 22.03 | 39.84 | 23.459 | 23.4 |
| 25.74 | 31.76 | 8.645 | 8.6 | 22.23 | 40.45 | 24.032 | 24 |
| 25.82 | 32.18 | 9.064 | 9 | 22.42 | 40.94 | 24.485 | 24.4 |
| 25.87 | 32.48 | 9.257 | 9.3 | 22.56 | 41.28 | 24.912 | 25 |
| 25.9 | 32.65 | 9.8 | 9.7 | 22.96 | 42.05 | 25.647 | 25.5 |
| 25.91 | 32.77 | 10.175 | 10.1 | 23.07 | 42.57 | 26.017 | 26 |
| 26.01 | 33.3 | 10.661 | 10.5 | 23.12 | 42.91 | 26.644 | 26.5 |
| 26.03 | 33.53 | 11.095 | 11 | 23.23 | 43.25 | 27.114 | 27 |
| 26.08 | 33.81 | 11.464 | 11.4 | 23.34 | 43.49 | 27.528 | 27.5 |
| 26.11 | 34.35 | 12.02 | 12 | 23.4 | 43.54 | 28.042 | 28 |
| 26 | 34.62 | 12.344 | 12.3 | 23.39 | 43.92 | 28.583 | 28.5 |

Table 1 (Continued)

| III | | | | IV | | | |
|---|---|---|---|---|---|---|---|
| $T_c$ (°C) | $T_h$ (°C) | ΔT (°C) | $V_{open}$ (mV) | $T_c$ (°C) | $T_h$ (°C) | ΔT (°C) | $V_{open}$ (mV) |
| 23.85 | 44.57 | 29.031 | 29 | 24.82 | 56.92 | 47.075 | 47 |
| 24.3 | 44.91 | 23.578 | 29.5 | 25.09 | 57.7 | 47.634 | 47.5 |
| 24.54 | 45.56 | 30.105 | 30 | 25.2 | 58.12 | 48.171 | 48 |
| 24.88 | 46.15 | 30.525 | 30.5 | 25.24 | 58.35 | 48.662 | 48.5 |
| 25.07 | 46.46 | 31.096 | 31 | 25.23 | 58.46 | 49.068 | 49 |
| 25.21 | 46.81 | 31.54 | 31.5 | 25.32 | 58.7 | 49.567 | 49.5 |
| 25.69 | 34.87 | 13.061 | 13 | 25.45 | 58.73 | 50.049 | 50 |
| 25.51 | 47.49 | 32.102 | 32 | 25.66 | 59.18 | 50.567 | 50.5 |
| 25.79 | 48.34 | 32.601 | 32.5 | 25.85 | 59.81 | 50.369 | 51.1 |
| 25.92 | 48.83 | 33.014 | 33 | 25.92 | 60.08 | 51.64 | 51.5 |
| 26.04 | 49.18 | 33.653 | 33.6 | 26.11 | 60.76 | 52.045 | 52 |
| 26.14 | 49.72 | 33.937 | 34 | 26.39 | 61.25 | 52.753 | 52.5 |
| 26.3 | 50.11 | 34.523 | 34.5 | 26.62 | 61.83 | 53.037 | 53 |
| 26.47 | 50.76 | 35.083 | 35 | 26.94 | 62.31 | 53.671 | 53.5 |
| 26.62 | 51.18 | 35.471 | 35.5 | 27.16 | 63.37 | 54.026 | 54 |
| 26.64 | 51.52 | 35.952 | 36 | 26.94 | 63.49 | 54.561 | 54.5 |
| 26.74 | 51.64 | 36.604 | 36.5 | 26.84 | 64.83 | 55.042 | 55 |
| 26.82 | 52.14 | 36.876 | 37 | 26.14 | 64.46 | 55.594 | 55.6 |
| 26.95 | 52.61 | 37.472 | 37.5 | 26.06 | 64.62 | 56.023 | 56 |
| 26.82 | 53.03 | 38.11 | 38 | 26 | 65.03 | 56.47 | 56.5 |
| 26.36 | 52.82 | 38.647 | 38.5 | 25.98 | 65.46 | 56.925 | 57 |
| 25.28 | 52.73 | 39.073 | 39 | 25.96 | 65.5 | 57.386 | 57.6 |
| 24.94 | 52.9 | 39.469 | 39.5 | 26.17 | 66.29 | 57.925 | 58 |
| 24.46 | 52.91 | 40.087 | 40 | 26.16 | 66.26 | 58.254 | 58.5 |
| 24.2 | 53.23 | 40.679 | 40.6 | 26.4 | 66.3 | 58.872 | 59 |
| 24.16 | 53.39 | 41.063 | 41 | 26.73 | 66.88 | 59.227 | 59.5 |
| 23.99 | 53.64 | 41.55 | 41.5 | 26.76 | 66.89 | 60.054 | 60 |
| 23.96 | 53.12 | 42 | 42 | 26.81 | 67.16 | 60.302 | 60.6 |
| 23.96 | 53.27 | 42.644 | 42.5 | 26.97 | 67.85 | 60.97 | 61.1 |
| 23.9 | 53.42 | 43.152 | 43.2 | 27.33 | 69.46 | 60.684 | 61.5 |
| 24.15 | 54.34 | 44.187 | 44 | 27.7 | 71.16 | 61.486 | 62 |
| 24.26 | 54.87 | 44.658 | 44.5 | 27.96 | 72.49 | 61.758 | 62.5 |
| 24.35 | 55.23 | 45.28 | 45 | 28.19 | 73.98 | 62.713 | 63.1 |
| 24.44 | 55.62 | 45.618 | 45.6 | 28.28 | 74.88 | 63.318 | 63.5 |
| 24.54 | 55.94 | 45.95 | 46 | 28.26 | 73.35 | 63.24 | 64 |
| 24.67 | 56.35 | 46.565 | 46.5 | 28.45 | 72.96 | 63.792 | 64.4 |

Table 1 (Continued)

| V | | | | VI | | | |
|---|---|---|---|---|---|---|---|
| $T_c$ ($^{o}$C) | $T_h$ ($^{o}$C) | $\Delta T$ ($^{o}$C) | $V_{open}$ (mV) | $T_c$ ($^{o}$C) | $T_h$ ($^{o}$C) | $\Delta T$ ($^{o}$C) | $V_{open}$ (mV) |
| 28.83 | 73.48 | 63.802 | 65 | 30.84 | 91.41 | 77.743 | 84 |
| 29.55 | 74.6 | 64.756 | 65.5 | 30.79 | 91.54 | 78.86 | 85.2 |
| 29.98 | 75.17 | 65.548 | 66.1 | 30.93 | 92.08 | 79.895 | 86.6 |
| 30.22 | 75.33 | 65.774 | 66.5 | 31.42 | 93.2 | 79.945 | 87 |
| 30.65 | 76.08 | 65.912 | 67 | 31.84 | 94.23 | 80.577 | 87.5 |
| 30.97 | 76.92 | 66.282 | 67.5 | 32.11 | 94.95 | 80.803 | 88.1 |
| 31.2 | 78.81 | 67.023 | 68.1 | 32.43 | 95.88 | 80.096 | 88.5 |
| 3.17 | 78.48 | 67.269 | 68.6 | 33.16 | 97.89 | 81.817 | 89.4 |
| 30.85 | 78.7 | 67.414 | 69.1 | 30.95 | 96.98 | 82.221 | 90.1 |
| 30.7 | 78.69 | 67.461 | 69.5 | 31.12 | 97.43 | 83.052 | 91.3 |
| 30.35 | 78.61 | 68.052 | 70 | | | | |
| 30.05 | 78.45 | 68.676 | 70.5 | | | | |
| 29.68 | 78.34 | 68.86 | 71 | | | | |
| 28.81 | 78.42 | 69.205 | 71.6 | | | | |
| 28.41 | 77.64 | 69.366 | 72 | | | | |
| 28.35 | 78.31 | 70.002 | 72.6 | | | | |
| 28.3 | 78.63 | 70.646 | 73.1 | | | | |
| 28.21 | 78.66 | 70.822 | 73.6 | | | | |
| 28.29 | 78.91 | 71.272 | 74.3 | | | | |
| 28.35 | 80.33 | 71.49 | 75 | | | | |
| 28.42 | 80.73 | 72.119 | 75.5 | | | | |
| 28.38 | 81.09 | 72.432 | 76 | | | | |
| 28.5 | 81.7 | 72.856 | 76.5 | | | | |
| 28.49 | 81.78 | 73.159 | 77 | | | | |
| 28.53 | 82.01 | 73.582 | 77.5 | | | | |
| 28.56 | 82.18 | 74.11 | 78 | | | | |
| 28.9 | 83.22 | 74.355 | 78.5 | | | | |
| 29.19 | 83.66 | 74.353 | 79 | | | | |
| 29.75 | 84.7 | 74.88 | 79.5 | | | | |
| 29.94 | 85.47 | 75.17 | 80 | | | | |
| 30.62 | 86.25 | 75.868 | 80.7 | | | | |
| 30.5 | 85.96 | 76.193 | 81.4 | | | | |
| 31.17 | 88.6 | 76.464 | 82 | | | | |
| 30.92 | 89.93 | 77.144 | 82.8 | | | | |
| 30.58 | 90.74 | 77.225 | 83.1 | | | | |
| 30.6 | 91.15 | 77.698 | 83.6 | | | | |

Table 2 Data of p-AST and n-BT thin film thermoelectric generator electrical power on PI.

| I | | | II | | |
|---|---|---|---|---|---|
| V (mV) | I (nA) | Power | V (mV) | I (nA) | Power |
| 0.001 | 983 | 0.983 | 20.3 | 772 | 15671.6 |
| 0.019 | 980 | 18.62 | 21.5 | 773 | 16619.5 |
| 0.099 | 989 | 97.911 | 22.56 | 759 | 17123.04 |
| 0.196 | 971 | 190.316 | 23.5 | 752 | 17672 |
| 0.288 | 960 | 276.48 | 24.26 | 742 | 18000.92 |
| 0.391 | 955 | 373.405 | 25.1 | 722 | 18122.2 |
| 0.49 | 978 | 479.22 | 25.8 | 719 | 18550.2 |
| 0.586 | 974 | 570.764 | 25.2 | 709 | 17866.8 |
| 0.679 | 975 | 662.025 | 27 | 706 | 19062 |
| 0.76 | 966 | 734.16 | 28 | 702 | 19656 |
| 0.886 | 975 | 863.85 | 28.2 | 694 | 19570.8 |
| 0.984 | 951 | 935.784 | 29.4 | 695 | 20433 |
| 1.9 | 955 | 1814.5 | 29.7 | 681 | 20225.7 |
| 2.89 | 964 | 2785.96 | 30.2 | 679 | 20505.8 |
| 3.06 | 957 | 2928.42 | 31.2 | 675 | 21060 |
| 3.34 | 955 | 3189.7 | 32.2 | 663 | 21348.6 |
| 3.53 | 949 | 3349.97 | 33 | 660 | 21780 |
| 3.8 | 941 | 3575.8 | 34.4 | 644 | 22153.6 |
| 4.8 | 939 | 4507.2 | 35.2 | 641 | 22563.2 |
| 5.5 | 924 | 5082 | 36.5 | 626 | 22849 |
| 6.3 | 911 | 5739.3 | 37.1 | 617 | 22890.7 |
| 7.27 | 908 | 6601.16 | 38.1 | 611 | 23279.1 |
| 7.1 | 907 | 6439.7 | 38.7 | 600 | 23220 |
| 8.9 | 901 | 8018.9 | 40.4 | 585 | 23634 |
| 9.7 | 889 | 8623.3 | 43 | 550 | 23650 |
| 10.58 | 884 | 9352.72 | 43.3 | 531 | 22992.3 |
| 11.36 | 876 | 9951.36 | 44.2 | 535 | 23647 |
| 12 | 855 | 10260 | 45 | 521 | 23445 |
| 12.85 | 854 | 10973.9 | 45.4 | 515 | 23381 |
| 13.4 | 847 | 11349.8 | 45.2 | 504 | 22780.8 |
| 14.12 | 838 | 11832.56 | 47.1 | 492 | 23173.2 |
| 14.72 | 813 | 11967.36 | 49.6 | 457 | 22667.2 |
| 15.691 | 819 | 12850.93 | 51.5 | 441 | 22711.5 |
| 16.166 | 813 | 13142.96 | 53.8 | 427 | 22972.6 |

Table 2 (Continued)

| I | | | II | | |
|---|---|---|---|---|---|
| V (mV) | I (nA) | Power | V (mV) | I (nA) | Power |
| 17.82 | 808 | 14398.56 | 56.1 | 411 | 23057.1 |
| 18.12 | 796 | 14423.52 | 57.3 | 395 | 22633.5 |
| 19.4 | 786 | 15248.4 | 58.8 | 380 | 22344 |
| III | | | | | |
| V (mV) | I (nA) | Power | | | |
| 65.1 | 297 | 19334.7 | | | |
| 60.1 | 365 | 21936.5 | | | |
| 67 | 281 | 18827 | | | |
| 68.3 | 268 | 18304.4 | | | |
| 71 | 250 | 17750 | | | |
| 71.5 | 245 | 17517.5 | | | |

Table 3 Data of p-AST and n-BT thin film thermoelectric generator open-circuit on SO.

| I | | | | II | | | |
|---|---|---|---|---|---|---|---|
| $T_c$ (°C) | $T_h$ (°C) | $\Delta T$ (°C) | $V_{open}$ (mV) | $T_c$ (°C) | $T_h$ (°C) | $\Delta T$ (°C) | $V_{open}$ (mV) |
| 23.09 | 24.94 | 1.85 | 0.4 | 44.06 | 52.86 | 8.8 | 8.2 |
| 22.89 | 24.74 | 1.85 | 0.5 | 45.02 | 54.4 | 9.38 | 8.8 |
| 23.14 | 24.95 | 1.81 | 0.6 | 45.78 | 55.41 | 9.63 | 9.2 |
| 23.29 | 25.15 | 1.86 | 0.8 | 46.7 | 57.33 | 10.63 | 9.6 |
| 24.09 | 26.1 | 2.01 | 1 | 48.51 | 58.74 | 10.23 | 10 |
| 24.63 | 26.76 | 2.13 | 1.2 | 49.05 | 60.32 | 11.27 | 10.4 |
| 25.58 | 27.78 | 2.2 | 1.4 | 50.01 | 60.76 | 10.75 | 10.8 |
| 26.18 | 28.51 | 2.33 | 1.6 | 51.11 | 61.9 | 10.79 | 11.1 |
| 26.09 | 28.79 | 2.7 | 1.8 | 51.48 | 62.46 | 10.98 | 11.4 |
| 25.81 | 29.04 | 3.23 | 2 | 52.31 | 64.39 | 12.08 | 12.1 |
| 25.82 | 29.37 | 3.55 | 2.2 | 54.04 | 66.31 | 12.27 | 12.5 |
| 26.06 | 29.88 | 3.82 | 2.4 | 54.91 | 68.18 | 13.27 | 13 |
| 26.43 | 30.41 | 3.98 | 2.6 | 56.14 | 68.93 | 12.79 | 13.4 |
| 27.02 | 31.22 | 4.2 | 2.8 | 57.58 | 70.59 | 13.01 | 14.1 |
| 27.62 | 31.94 | 4.32 | 3 | 59 | 72.38 | 13.38 | 14.6 |
| 28.61 | 33.14 | 4.53 | 3.2 | 60.65 | 74.66 | 14.01 | 15.2 |
| 29.53 | 34.08 | 4.55 | 3.4 | 62.32 | 76.61 | 14.29 | 15.5 |
| 29.68 | 34.41 | 4.73 | 3.7 | 62.82 | 76.99 | 14.17 | 16 |
| 31.78 | 38.76 | 6.98 | 4.1 | 62.84 | 79.01 | 16.17 | 16.5 |
| 31.97 | 38.21 | 6.24 | 4.2 | 63.61 | 78.48 | 14.87 | 16.9 |
| 32.93 | 38.76 | 5.83 | 4.4 | 64.98 | 82.17 | 17.19 | 17.6 |
| 34.68 | 40.5 | 5.82 | 4.7 | 65.73 | 81.69 | 15.96 | 17.8 |
| 34.81 | 41.02 | 6.21 | 5 | 66.12 | 82.13 | 16.01 | 18 |
| 34.62 | 41.06 | 6.44 | 5.2 | 67.96 | 86.06 | 18.1 | 18.4 |
| 34.6 | 41.32 | 6.72 | 5.4 | 69.13 | 86.1 | 16.97 | 18.6 |
| 34.8 | 41.3 | 6.5 | 5.6 | 70.62 | 88.92 | 18.3 | 18.9 |
| 35.56 | 42.32 | 6.76 | 5.8 | 70.24 | 89.57 | 19.33 | 19.2 |
| 35.88 | 42.89 | 7.01 | 6 | 70.17 | 88.91 | 18.74 | 19.3 |
| 36.29 | 43.46 | 7.17 | 6.2 | 70.65 | 89.85 | 19.2 | 19.5 |
| 36.29 | 43.46 | 7.17 | 6.2 | 71.67 | 90.49 | 18.82 | 19.7 |
| 36.82 | 44.17 | 7.35 | 6.3 | 72.34 | 92.37 | 20.03 | 19.9 |
| 38.18 | 46.01 | 7.83 | 6.7 | 74.13 | 91.95 | 17.82 | 20.3 |
| 39.24 | 47.47 | 8.23 | 7 | 74.15 | 94.1 | 19.95 | 20.7 |
| 40.5 | 49.03 | 8.53 | 7.4 | 75.38 | 96.19 | 20.81 | 21 |
| 40.55 | 49.05 | 8.5 | 7.8 | 77.68 | 97.58 | 19.9 | 21.5 |
| 42.31 | 50.75 | 8.44 | 8 | | | | |

Table 4 Data of p-AST and n-BT thin film thermoelectric generator electrical power on SO.

| I | | | II | | |
|---|---|---|---|---|---|
| V (mV) | I (nA) | Power | V (mV) | I (nA) | Power |
| 0.15 | 297 | 44.55 | 7.5 | 202 | 1515 |
| 0.3 | 294 | 88.2 | 7.8 | 197 | 1536.6 |
| 0.58 | 291 | 168.78 | 8 | 193 | 1544 |
| 0.88 | 288 | 253.44 | 8.4 | 190 | 1596 |
| 1.16 | 286 | 331.76 | 8.7 | 188 | 1635.6 |
| 1.43 | 284 | 406.12 | 8.9 | 187 | 1664.3 |
| 1.69 | 282 | 476.58 | 10.2 | 186 | 1897.2 |
| 1.96 | 279 | 546.58 | 10.5 | 180 | 1890 |
| 2.122 | 275 | 583.55 | | | |
| 2.438 | 271 | 660.698 | | | |
| 2.69 | 270 | 726.3 | | | |
| 2.94 | 265 | 779.1 | | | |
| 3.1 | 261 | 809.1 | | | |
| 3.3 | 259 | 854.7 | | | |
| 3.8 | 254 | 965.2 | | | |
| 4 | 251 | 1004 | | | |
| 4.1 | 246 | 1008.6 | | | |
| 4.4 | 243 | 1069.2 | | | |
| 4.6 | 245 | 1127 | | | |
| 4.7 | 240 | 1128 | | | |
| 4.9 | 239 | 1171.1 | | | |
| 5.1 | 236 | 1203.6 | | | |
| 5.2 | 232 | 1206.4 | | | |
| 5.4 | 228 | 1231.4 | | | |
| 5.6 | 226 | 1265.6 | | | |
| 5.7 | 225 | 1282.5 | | | |
| 5.9 | 221 | 1303.9 | | | |
| 6.1 | 219 | 1335.9 | | | |
| 6.3 | 218 | 1373.4 | | | |
| 6.4 | 214 | 1369.6 | | | |
| 6.6 | 214 | 1412.4 | | | |
| 6.7 | 212 | 1420.4 | | | |
| 6.9 | 210 | 1449 | | | |
| 7.1 | 209 | 1483.9 | | | |
| 7.3 | 205 | 1496.5 | | | |

# APPENDICE C

# INTERNATIONAL CONFERENCES PUBLICATIONS

## INTERNATIONAL CONFERENCES

1. **Somporn Thaowankaew**, Athorn Vora-ud, “Effect of Rapid Thermal Annealing on the Thermoelectric Properties of $AgSbTe_2$ Thin Films Prepare by DC Magnetron Sputtering Process”, TACT2019 International Thin Films Conference Nov.17– 20, 2019, National Taipei University of Technology, Taipei, Taiwan
2. **Somporn Thaowankaew**, Athorn Vora-ud, “Thermoelectric Properties of Ag doped $Sb_2Te_3$ Thin Films Deposited by RF Magnetron Sputtering Process”, The $5^{th}$ Asian Conference on Thermoelectrics and the 6th Southeast Asia Conference on Thermoelectrics (ACT&SACT2020) 17-18 December 2020, Online Conference, Sakon Nakhon Rajabhat University, Thailand

## PUBLICATIONS

### FIRST AUTHOR

1. **Somporn Thaowonkaew**, Kumar Manish, and Athorn Vora-Ud. "Thermoelectric Properties of Ag-Doped $Sb_2Te_3$ Thin Films on $SiO_2$ and Polyimide Substrates with Rapid Thermal Annealing." *Journal of Electronic Materials* 50.5 (2021): 2669-2673. (**ISI** Web of Knowledge ,Impact factor (2021) = 2.047,Journal of Electronic Materials Index)

2. **Somporn Thaowankaew**, Mekhala Inswang. Athorn Vora-ud, Mati Horprathum, Pennapa Muthitamongkol, Santi Maensiri, Manish Kumar, Thang Bach Phan and Tosawat Seetawan “Effect of substrate rotation and rapid thermal annealing induced the homogeneous microstructure and thermoelectric properties of Ag-doped $Sb_2Te_3$ thin films” “Vacuum” **(On process)**

## CO-AUTHOR

1. Vora-Ud, A., Kasemsin, W., Seetawan, T., **Thaowankaew, S**., & Weatchapitak, D. (2019, December). Designing and analyzing on thermoelectric cooler for turbomolecular pump cooling applications. In 2019 Research, Invention, and Innovation Congress (RI2C) (pp. 1-4). IEEE.

2. Prainetr, N., Vora-ud, A., **Thaowankaew, S.**, Horprathum, M., Muthitamongkol, P., & Seetawan, T. (2020). Effect of substrates on thermoelectric properties of Ag–Sb–Te thin films within the temperature annealing. Physica B: Condensed Matter, 582, 411977.

3. Prainetr, N., Vora-Ud, A., Horprathum, M., Muthitamongkol, P., **Thaowankaew, S.**, Santhaveesuk, T., ... & Seetawan, T. (2020). Transfer of P-type to N-type Thermoelectric Properties of Ag-Sb-Te Thin Film Through Temperature Annealing and Its Electrical Power Generation. Journal of Electronic Materials, 49(1), 572-577.

4. Prainetr, N., Vora-ud, A., **Thaowankaew, S**., Horprathum, M., & Seetawan, T. (2020). DEPOSITION AND PHASE TRANSFORMATION OF SILVER ANTIMONY TELLURIDE THIN FILMS BY DC MAGNETRON SPUTTERING. Suranaree Journal of Science & Technology, 27(1).

5. Vora-ud, A., **Thaowankaew, S**., Khajonrit, J., Singsoog, K., Muthitamongkol, P., Chananonnawathorn, C., ... & Seetawan, T. (2020). Rapid thermal annealing induced the c-axis (00 l) preferred orientation and the p-type thermoelectric properties of Bi-Sb-Te thin films. Thin Solid Films, 706, 138094.

6. Khottummee, N., Sumphao, T., & **Thaowankaew, S.** (2021). Transparent thin film of zinc zirconate deposited by DC magnetron sputtering technique. SNRU Journal of Science and Technology, 13(1), 37-45.
7. Truong, D, **Thaowankaew, S.,** Muthitamongkol, P., Horprathum, M., Kumar, M., Le,T. B. N., Pham, A. T. T., ... & Phan, T. B. (2022). Relaxation of residual stress-controlled thermopower factor in transparent-flexible Ti-doped ZnO thin films. Ceramics International, 48(2), 2605-2613.

# CONFERENCES I

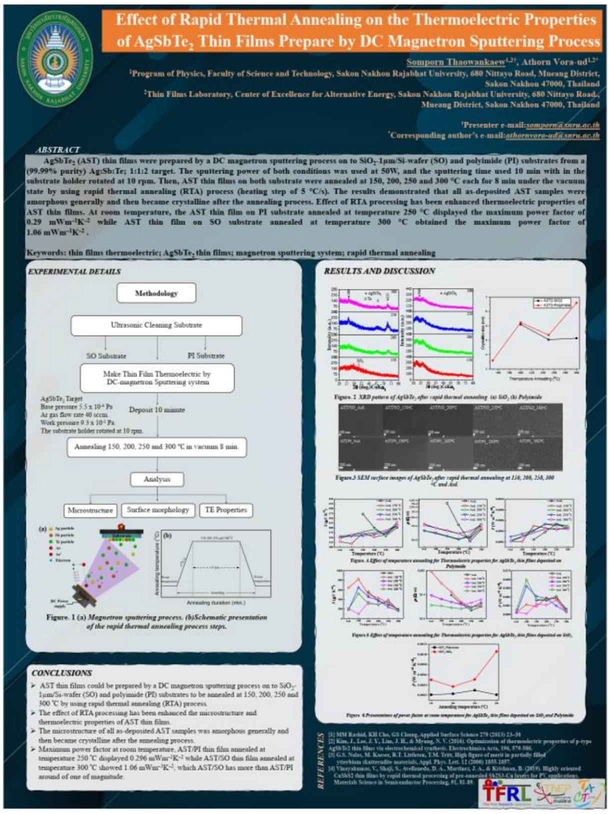

## Effect of Rapid Thermal Annealing on the Thermoelectric Properties of $AgSbTe_2$ Thin Films Prepare by DC Magnetron Sputtering Process

**Somporn Thaowankaew**[1,2†], Athorn Vora-ud[1,2*]
[1]Program of Physics, Faculty of Science and Technology, Sakon Nakhon Rajabhat University, 680 Nittayo Road, Mueang District, Sakon Nakhon 47000, Thailand
[2]Thin Films Laboratory, Center of Excellence for Alternative Energy, Sakon Nakhon Rajabhat University, 680 Nittayo Road, Mueang District, Sakon Nakhon 47000, Thailand

†Presenter e-mail:somporn@snru.ac.th
*Corresponding author's e-mail:athornvora-ud@snru.ac.th

### ABSTRACT

$AgSbTe_2$ (AST) thin films were prepared by a DC magnetron sputtering process on to $SiO_2$-1μm/Si-wafer (SO) and polyimide (PI) substrates from a (99.99% purity) Ag:Sb:Te; 1:1:2 target. The sputtering power of both conditions was used at 50W, and the sputtering time used 10 min with in the substrate holder rotated at 10 rpm. Then, AST thin films on both substrate were annealed at 150, 200, 250 and 300 °C each for 8 min under the vacuum state by using rapid thermal annealing (RTA) process (heating step of 5 °C/s). The results demonstrated that all as-deposited AST samples were amorphous generally and then became crystalline after the annealing process. Effect of RTA processing has been enhanced thermoelectric properties of AST thin films. At room temperature, the AST thin film on PI substrate annealed at temperature 250 °C displayed the maximum power factor of 0.29 $mWm^{-1}K^{-2}$ while AST thin film on SO substrate annealed at temperature 300 °C obtained the maximum power factor of 1.06 $mWm^{-1}K^{-2}$ .

Keywords: thin films thermoelectric; $AgSbTe_2$ thin films; magnetron sputtering system; rapid thermal annealing

### EXPERIMENTAL DETAILS

Methodology

Ultrasonic Cleaning Substrate

SO Substrate

PI Substrate

Make Thin Film Thermoelectric by DC-magnetron Sputtering system

$AgSbTe_2$ Target
Base pressure 5.5 x $10^{-4}$ Pa
Ar gas flow rate 40 sccm.
Work pressure 9.3 x $10^{-1}$ Pa.
The substrate holder rotated at 10 rpm.

Deposit 10 minute

Annealing 150, 200, 250 and 300 °C in vacuum 8 min.

Analysis

Microstructure

Surface morphology

TE Properties

Figure. 1 (a) *Magnetron sputtering process. (b)Schematic presentation of the rapid thermal annealing process steps.*

### RESULTS AND DISCUSSION

*Figure. 2 XRD pattern of $AgSbTe_2$ after rapid thermal annealing (a) $SiO_2$ (b) Polyimide*

*Figure.3 SEM surface images of $AgSbTe_2$ after rapid thermal annealing at 150, 200, 250, 300 °C and Asd.*

*Figure. 4 Effect of temperature annealing for Thermoelectric properties for $AgSbTe_2$ thin films deposited on Polyimide*

*Figure 5 Effect of temperature annealing for Thermoelectric properties for $AgSbTe_2$ thin films deposited on $SiO_2$*

*Figure 6 Presentation of power factor at room temperature for $AgSbTe_2$ thin films deposited on $SiO_2$ and Polyimide*

### CONCLUSIONS

- AST thin films could be prepared by a DC magnetron sputtering process on to $SiO_2$-1μm/Si-wafer (SO) and polyimide (PI) substrates to be annealed at 150, 200, 250 and 300 °C by using rapid thermal annealing (RTA) process.
- The effect of RTA processing has been enhanced the microstructure and thermoelectric properties of AST thin films.
- The microstructure of all as-deposited AST samples was amorphous generally and then became crystalline after the annealing process.
- Maximum power factor at room temperature, AST/PI thin film annealed at temperature 250 °C displayed 0.296 $mWm^{-1}K^{-2}$ while AST/SO thin film annealed at temperature 300 °C showed 1.06 $mWm^{-1}K^{-2}$, which AST/SO has more than AST/PI around of one of magnitude.

### REFERENCES

[1] MM Rashid, KH Cho, GS Chung, Applied Surface Science 279 (2013) 23–30
[2] Kim, J., Lee, J. Y., Lim, J. H., & Myung, N. V. (2016). Optimization of thermoelectric properties of p-type AgSbTe2 thin films via electrochemical synthesis. Electrochimica Acta, 196, 579-586.
[3] G.S. Nolas, M. Kaeser, R.T. Littleton, T.M. Tritt, High figure of merit in partially filled ytterbium skutterudite materials, Appl. Phys. Lett. 12 (2000) 1855-1857.
[4] Vinayakumar, V., Shaji, S., Avellaneda, D. A., Martinez, J. A., & Krishnan, B. (2019). Highly oriented CuSbS2 thin films by rapid thermal processing of pre-annealed Sb2S3-Cu layers for PV applications. Materials Science in Semiconductor Processing, 91, 81-89.

## CONFERENCES II

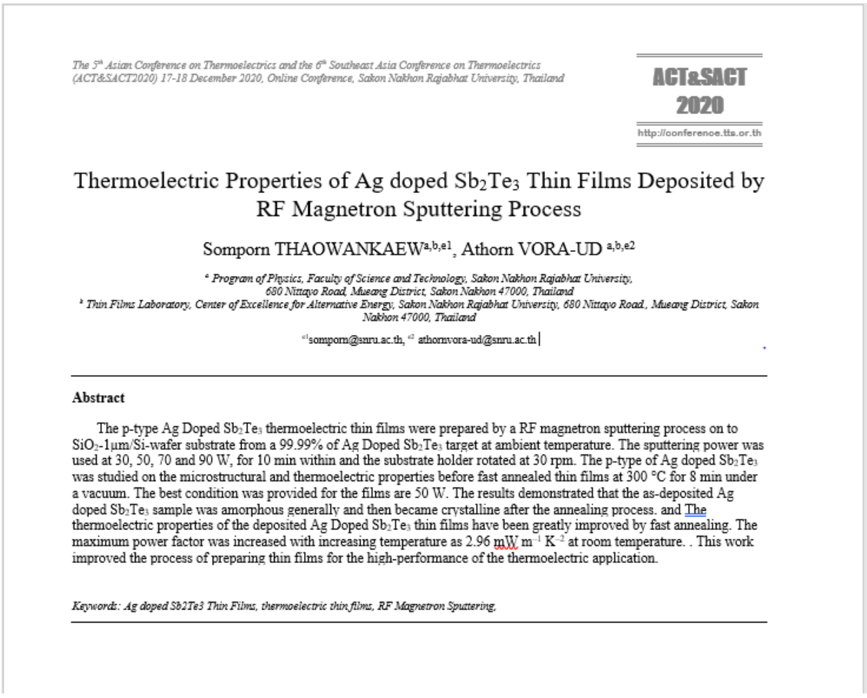

*The 5th Asian Conference on Thermoelectrics and the 6th Southeast Asia Conference on Thermoelectrics*
*(ACT&SACT2020) 17-18 December 2020, Online Conference, Sakon Nakhon Rajabhat University, Thailand*

ACT&SACT
2020
http://conference.tts.or.th

# Thermoelectric Properties of Ag doped $Sb_2Te_3$ Thin Films Deposited by RF Magnetron Sputtering Process

Somporn THAOWANKAEW[a,b,e1], Athorn VORA-UD [a,b,e2]

[a] *Program of Physics, Faculty of Science and Technology, Sakon Nakhon Rajabhat University,*
*680 Nittayo Road, Mueang District, Sakon Nakhon 47000, Thailand*
[b] *Thin Films Laboratory, Center of Excellence for Alternative Energy, Sakon Nakhon Rajabhat University, 680 Nittayo Road., Mueang District, Sakon Nakhon 47000, Thailand*

[e1]somporn@snru.ac.th, [e2] athornvora-ud@snru.ac.th

---

## Abstract

The p-type Ag Doped $Sb_2Te_3$ thermoelectric thin films were prepared by a RF magnetron sputtering process on to $SiO_2$-1µm/Si-wafer substrate from a 99.99% of Ag Doped $Sb_2Te_3$ target at ambient temperature. The sputtering power was used at 30, 50, 70 and 90 W, for 10 min within and the substrate holder rotated at 30 rpm. The p-type of Ag doped $Sb_2Te_3$ was studied on the microstructural and thermoelectric properties before fast annealed thin films at 300 °C for 8 min under a vacuum. The best condition was provided for the films are 50 W. The results demonstrated that the as-deposited Ag doped $Sb_2Te_3$ sample was amorphous generally and then became crystalline after the annealing process. and The thermoelectric properties of the deposited Ag Doped $Sb_2Te_3$ thin films have been greatly improved by fast annealing. The maximum power factor was increased with increasing temperature as 2.96 mW $m^{-1}$ $K^{-2}$ at room temperature. . This work improved the process of preparing thin films for the high-performance of the thermoelectric application.

*Keywords: Ag doped Sb2Te3 Thin Films, thermoelectric thin films, RF Magnetron Sputtering,*

---

Journal of ELECTRONIC MATERIALS, Vol. 50, No. 5, 2021
https://doi.org/10.1007/s11664-021-08788-w

ORIGINAL RESEARCH ARTICLE

# Thermoelectric Properties of Ag-Doped $Sb_2Te_3$ Thin Films on $SiO_2$ and Polyimide Substrates with Rapid Thermal Annealing

SOMPORN THAOWONKAEW,[1,2] MANISH KUMAR,[3]
and ATHORN VORA-UD[1,2,4]

1.—Program of Physics, Faculty of Science and Technology, Sakon Nakhon Rajabhat University, 680 Nittayo Road, Mueang District, Sakon Nakhon 47000, Thailand. 2.—Thailand Center of Excellence in Physics, Ministry of Higher Education, Science, Research and Innovation, 328 Si Ayutthaya Road, Bangkok 10400, Thailand. 3.—Centre for Advanced Materials, Organisation for Science Innovations and Research, RS Science Park, Bah 283104, India. 4.—e-mail: athornvora-ud@snru.ac.th

This work reports Ag-doped $Sb_2Te_3$ (A-ST) thin films synthesized by DC magnetron sputtering method onto $SiO_2$ (SO) and polyimide (PI) substrates based on atomic composition optimization. The effect of post-depositional rapid thermal annealing on the crystallinity, morphology, composition, and thermoelectric properties of thin films was investigated. It was found that thin films on crystalline SO substrate yielded higher crystallinity and eventually a higher thermoelectric power factor in comparison to those grown on a polyimide substrate. The maximum room-temperature power factors achieved were 0.53 mW $m^{-1}$ $K^{-2}$ (PI) and 3.95 mW $m^{-1}$ $K^{-2}$ (SO).

**Key words:** Ag-doped $Sb_2Te_3$ thermoelectric thin films, magnetron sputtering method, rapid thermal annealing

## INTRODUCTION

Currently, $Sb_2Te_3$ is considered for high-performance thermo-electric (TE) thin films owing to its semiconductor behavior having a narrow bandgap around 0.21 eV[1] and behaving as a topological insulator. It can be transformed into both *n*-type and *p*-type semiconductors by doping with an appropriate dopant.[2] For example, Fe-doped $Sb_2Te_3$ induced multiple Fermi pockets, causing reduced carrier density and mobility.[3] Since the carrier density and mobility control the power factor of TE materials[4] which is related to the performance of TE materials as defined with the dimensionless figure of merit ($ZT$);

$$ZT = \frac{S^2T}{\rho\kappa} = \frac{(PF)T}{\kappa}, \quad (1)$$

where $S$, $\rho$, $\kappa$, and $T$ are Seebeck coefficient, electrical resistivity, thermal conductivity, and absolute temperature, respectively. $S^2/\rho$ is defined as the power factor (PF). Traditional thin films have usually employed different substrates such as hard-rough $Al_2O_3$ and $SrTiO_3$,[5,6] hard-flat glass and $SiO_2$,[7] and flexible-very flat polyimide.[8] Considering that flexible TE thin film is one of the new generations of TE technology, it holds potential in wearable applications.[9] It has been reported that flexible $Sb_2Te_3$ thin films have demonstrated a maximum PF of $0.5\times10^{-3}$ W $m^{-1}$ $K^{-2}$ (at room temperature)[10] which can be improved to $2.3\times10^{-3}$ W $m^{-1}$ $K^{-2}$ when the measurement temperature is raised to 373 K.[11] Doped $Sb_2Te_3$ material, i.e. $AgSbTe_2$ *p*-type material, was obtained from a solid solution of $Ag_2Te$ and $Sb_2Te_3$[12–14] and demonstrated an interesting high $ZT$ around 1.59 at 673 K[15] and 1.55 at 533 K.[16]

Various magnetron sputtering methods are employed for controlling the microstructure and composition of TE thin films which eventually

(Received October 24, 2020; accepted January 27, 2021;

dictates the TE properties.[17–20] In this work, we doped Ag into $Sb_2Te_3$ (Ag-doped $Sb_2Te_3$, or A-ST) thin films grown on $SiO_2$/Si wafer and polyimide substrates through a direct-current (DC) magnetron sputtering technique. The effect of rapid thermal annealing (RTA) of thin films grown on both kinds of substrates on the crystalline structure, morphology, thickness, composition, and electrical and thermoelectric properties of thin films have been presented and correlated.

## EXPERIMENTAL DETAIL

A-ST thin films were prepared by a DC magnetron sputtering process onto 1-$\mu$m $SiO_2$/Si wafer and polyimide substrates at a target ratio of (99.99% purity) Ag:Sb:Te 1:1:2. The base pressure was below $5.5 \times 10^{-4}$ Pa, and the working pressure was about 0.93 Pa with Ar gas (99.999% UHP purity) set at a flow rate of 40 sccm. The sputtering power applied to the target was varied from 30 W, 50 W, 70 W, and 90 W, whereas the sputtering time was fixed as 10 min to optimize the atomic composition of the film on the SO substrates. For uniformity, the substrate holder was rotated at 10 rpm. After the deposition, A-ST thin films grown on both substrates with the sputtering power of 50 W were annealed by a RTA process (under the vacuum state) at temperatures of 150°C, 200°C, 250°C, and 300°C for 8 min (heating step of 5°C/s). After the RTA process, the samples were analyzed for their microstructure, morphology-thickness, and atomic composition using an x-ray diffractometer (XRD; XRD6100, Shimadzu), field emission scanning electron microscope (FE-SEM; SU8030, Hitachi), and energy-dispersive x-ray spectroscopy (EDX; SU8030, Hitachi), respectively. At room temperature, TE properties (electrical resistivity $\rho$ and Seebeck coefficient $S$) of the annealed thin films were measured by the ZEM-3 apparatus (ZEM-3, Advance Riko) under helium atmosphere.

## RESULTS AND DISCUSSION

Figure 1 shows the microstructure and atomic composition of the as-deposited film as optimized by varying sputtering power to be applied to the target at 30 W, 50 W, 70 W, and 90 W. The microstructure and atomic composition of the as-deposited film were determined by XRD and EDX techniques. Figure 1a presents the XRD results of as-deposited thin films showing amorphous behavior, which is a common feature of sputtered material. The EDX results showed that the Ag atoms consisted of the film at a sputtering power of 50 W to be configured to optimize the Ag doping into $Sb_2Te_3$ as shown in Fig. 1b. Figure 2 shows the XRD patterns of A-ST thin films grown on SO and PI substrates with a sputtering power of 50 W, as a function of annealing temperature. Figure 2a displays the $Sb_2Te_3$ phase structure of annealed A-ST thin films on SO by the diffraction peaks of (009), (00 $\underline{13}$), and (00 $\underline{16}$) planes, as confirmed with JCPDS 15-0727. Figure 2b displays the phase structure of annealed A-ST thin films grown on PI substrates. Here, a peak of the (009) plane was observed, assigned as the XRD peaks of the $TeO_2$[21] due to the partially burned surface of the polymer substrate.[22] This small hump due to $TeO_2$ phase is attributed to the partial surface oxidation of unsaturated Te atoms. It should be noted here that annealing in normal vacuum conditions (as used in present case) only minimizes the presence of oxygen atoms and does not completely restrain the oxygen atoms and subsequently

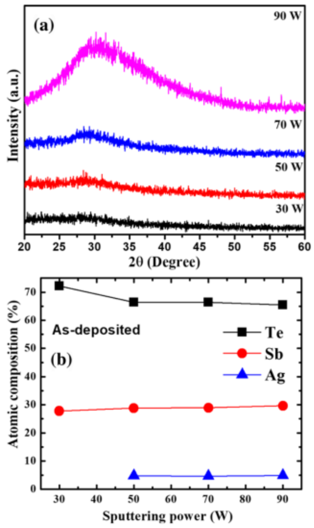

Fig 1. (a) XRD patterns and (b) atomic composition optimization of the as-deposited thin-film samples with varying sputtering power.

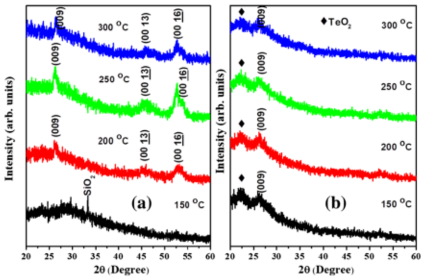

Fig 2. XRD patterns of A-ST thin films as a function of annealing temperature grown on (a) SO and (b) PI substrates.

the chance of surface oxidation. It should be further noted that polymer substrate could also be thermally unstable during the vacuum annealing, as reported in an earlier study of Ref. 22. Such condition might lead to the diffusion of Ti atoms underneath towards the surface and therefore resulting in partial oxidation of Te. This result shows that in the case of the PI substrate, similar annealing conditions induce oxidation of thin film surface.

SEM images show the surface morphology and thickness of the A-ST thin films grown on SO and PI substrates, as shown in Fig. 3. The SEM images of as-deposited and annealed thin films correspond to (1) SO and (2) PI substrates (a) as-deposited, and annealed at (b) 150°C, (c) 200°C, (d) 250°C, and (e) 300°C. Cross-section images of thin films are inserted in corresponding SEM images. The as-deposited films demonstrate an exceptionally smooth and uniform surface morphology. It is observed that the thickness of the films decreased slightly from 260 nm (as deposited) to 173 nm (RTA at 300°C). The thickness of films decreases upon annealing due to the crystallization of material and partial re-evaporation of loosely bonded surface atoms at high annealing temperature. Also, when the temperature of RTA increases, there is an evolution of flake-like surface morphology. The surface morphology of as-deposited film illustrated a smooth surface, homogeneous morphology, and perfect adherence to the substrates. After the RTA, the morphologies of the thin films were different from that of the as-deposited sample with the grain growth and surface roughness increasing. These results confirmed that the as-deposited thin films were amorphous and then became crystalline after the temperature annealing, corresponding to the XRD results. The EDX spectra for the composition of A-ST thin films on both substrates are shown in Fig. 4, corresponding to (1) SO and (2) PI substrates (a) as-deposited, and annealed (b) 150°C, (c) 200°C, (d) 250°C and (e) 300°C. EDX results demonstrate significant contributions from the film composed of elements Ag, Sb, and Te, along with minor contributions from C, Si, and O elements for the SO substrate and C and O elements for the PI substrate.

The room-temperature thermoelectric properties ($S$, $\rho$, and $P$) of the A-ST thin films on SO and PI substrates are shown in Fig. 5 as a function of RTA temperatures. The annealed A-ST thin films grown on both substrates exhibited $p$-type thermoelectricity. The films on SO substrates had higher $S$ values than those of the films on PI substrates at annealing temperatures of 150°C to 250°C, and then decreased slightly to exhibit similar values (of corresponding films grown on PI substrate) at an annealing temperature of 300°C. The $\rho$ values of annealed thin films grown on SO substrates were lower than those of films grown on PI substrates for the entire range of annealing temperature. At an annealing temperature of 250°C, the lowest $\rho$ values obtained for the thin films were $1.40 \times 10^{-5}$ Ω m and $4.65 \times 10^{-5}$ Ω m for the SO and PI substrates, respectively. At the same lowest electrical resistivity and annealing temperature, the A-ST thin films obtained a maximum power factor of 3.95 mW $m^{-1}$ $K^{-2}$ for the SO substrate and 0.53 mW $m^{-1}$ $K^{-2}$ for the PI substrate. The obtained power factor values of the A-ST thin films grown on the PI substrate are found comparable to the reported power factor of flexible ST thin films.[11] Moreover, the A-ST thin film on the SO substrate yielded power factors comparable to those reported for Ag-doped $Ge_2Sb_2Te_5$ thin film.[23] Such interesting power factor values suggest that these films may be used in flexible thermoelectric devices. The thermoelectric properties of films deposited on the SO substrate are better than those on the PI substrate because they yield better phase quality (purity) in comparison to the case of the PI

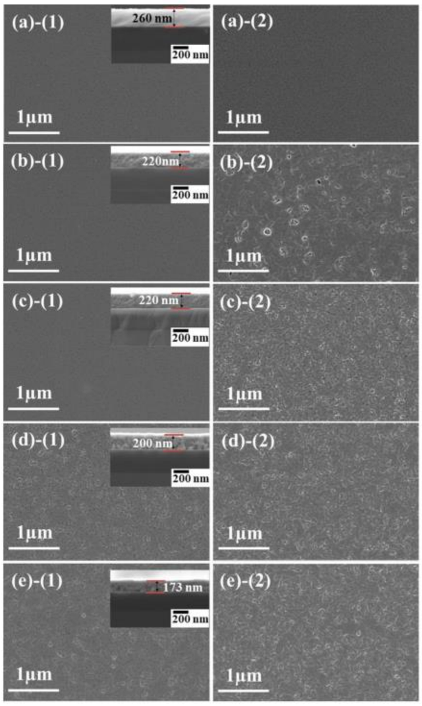

Fig 3. SEM images for surface morphology of A-ST thin films grown on (1) SO and (2) PI substrates: (a) as-deposited and annealed at (b) 150°C, (c) 200°C, (d) 250°C, and (e) 300°C. Cross sections of thin films are inserted in the corresponding SEM images.

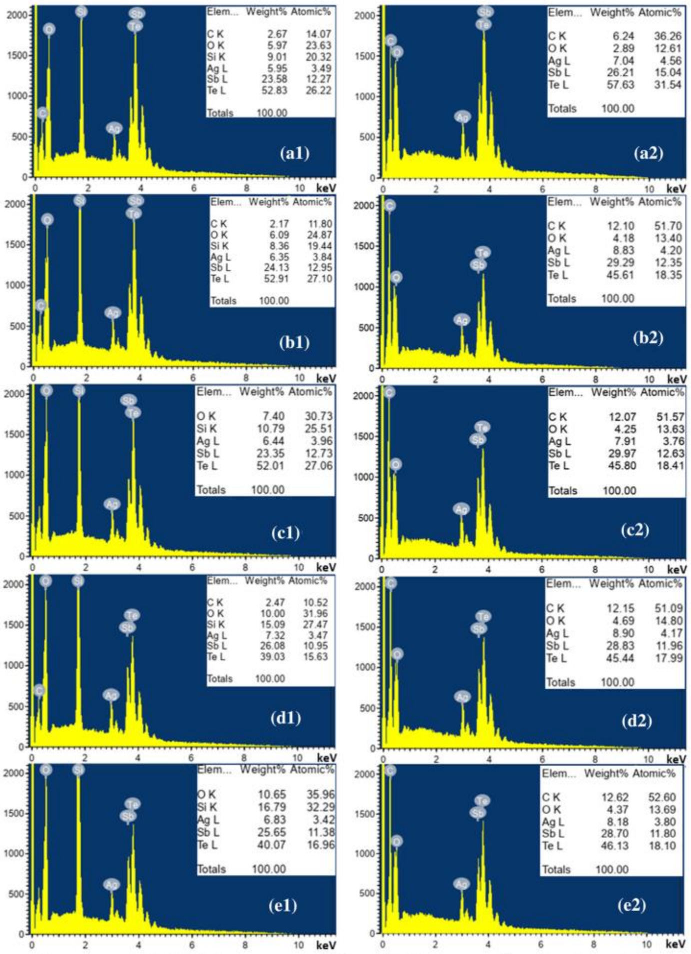

(a1)

| Elem... | Weight% | Atomic% |
|---|---|---|
| C K | 2.67 | 14.07 |
| O K | 5.97 | 23.63 |
| Si K | 9.01 | 20.32 |
| Ag L | 5.95 | 3.49 |
| Sb L | 23.58 | 12.27 |
| Te L | 52.83 | 26.22 |
| Totals | 100.00 | |

(a2)

| Elem... | Weight% | Atomic% |
|---|---|---|
| C K | 6.24 | 36.26 |
| O K | 2.89 | 12.61 |
| Ag L | 7.04 | 4.56 |
| Sb L | 26.21 | 15.04 |
| Te L | 57.63 | 31.54 |
| Totals | 100.00 | |

(b1)

| Elem... | Weight% | Atomic% |
|---|---|---|
| C K | 2.17 | 11.80 |
| O K | 6.09 | 24.87 |
| Si K | 8.36 | 19.44 |
| Ag L | 6.35 | 3.84 |
| Sb L | 24.13 | 12.95 |
| Te L | 52.91 | 27.10 |
| Totals | 100.00 | |

(b2)

| Elem... | Weight% | Atomic% |
|---|---|---|
| C K | 12.10 | 51.70 |
| O K | 4.18 | 13.40 |
| Ag L | 8.83 | 4.20 |
| Sb L | 29.29 | 12.35 |
| Te L | 45.61 | 18.35 |
| Totals | 100.00 | |

(c1)

| Elem... | Weight% | Atomic% |
|---|---|---|
| O K | 7.40 | 30.73 |
| Si K | 10.79 | 25.51 |
| Ag L | 6.44 | 3.96 |
| Sb L | 23.35 | 12.73 |
| Te L | 52.01 | 27.06 |
| Totals | 100.00 | |

(c2)

| Elem... | Weight% | Atomic% |
|---|---|---|
| C K | 12.07 | 51.57 |
| O K | 4.25 | 13.63 |
| Ag L | 7.91 | 3.76 |
| Sb L | 29.97 | 12.63 |
| Te L | 45.80 | 18.41 |
| Totals | 100.00 | |

(d1)

| Elem... | Weight% | Atomic% |
|---|---|---|
| C K | 2.47 | 10.52 |
| O K | 10.00 | 31.96 |
| Si K | 15.09 | 27.47 |
| Ag L | 7.32 | 3.47 |
| Sb L | 26.08 | 10.95 |
| Te L | 39.03 | 15.63 |
| Totals | 100.00 | |

(d2)

| Elem... | Weight% | Atomic% |
|---|---|---|
| C K | 12.15 | 51.09 |
| O K | 4.69 | 14.80 |
| Ag L | 8.90 | 4.17 |
| Sb L | 28.83 | 11.96 |
| Te L | 45.44 | 17.99 |
| Totals | 100.00 | |

(e1)

| Elem... | Weight% | Atomic% |
|---|---|---|
| O K | 10.65 | 35.96 |
| Si K | 16.79 | 32.29 |
| Ag L | 6.83 | 3.42 |
| Sb L | 25.65 | 11.38 |
| Te L | 40.07 | 16.96 |
| Totals | 100.00 | |

(e2)

| Elem... | Weight% | Atomic% |
|---|---|---|
| C K | 12.62 | 52.60 |
| O K | 4.37 | 13.69 |
| Ag L | 8.18 | 3.80 |
| Sb L | 28.70 | 11.80 |
| Te L | 46.13 | 18.10 |
| Totals | 100.00 | |

Fig 4. Atomic compositions of annealed A-ST thin films grown on (1) SO and (2) PI substrates: (a) as-deposited and annealed at (b) 150°C, (c) 200°C, (d) 250°C, and (e) 300°C.

substrate, where the thermally unstable substrate induces the surface oxidation of Te atoms.

## CONCLUSION

A-ST thin films were synthesized on 1-$\mu$m $SiO_2$/Si-wafer and polyimide substrates by DC magnetron sputtering. The effect of the post-deposition RTA process on the microstructural and thermoelectric properties of the A-ST thin films was studied and presented. At room temperature, the maximum power factor of the A-ST thin film on the SO substrate (3.95 mW $m^{-1}$ $K^{-2}$) was found to be greater than that on the PI substrate (0.53 mW $m^{-1}$ $K^{-2}$), and roughly around 3.42 mW $m^{-1}$ $K^{-2}$ for RTA at 250°C.

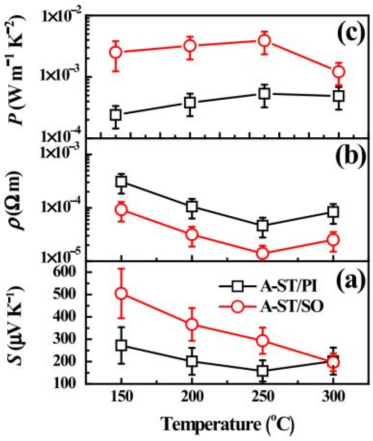

Fig 5. Thermoelectric properties: (a) $S$, (b) $\rho$, and (c) $P$ values of A-ST thin films on SO and PI substrates as a function of the annealing temperature.

## ACKNOWLEDGMENTS

This work was financially supported by the Thailand Center of Excellence in Physics.

## CONFLICT OF INTEREST

On behalf of all authors, the corresponding author declares that there is no conflict of interest.

## REFERENCES

1. A. Lawal, A. Shaari, R. Ahmed, and N. Jarkoni, *Results Phys.*, 2017, 7, p 2302.
2. N.N. Greenwood, and E. Alan, *Chemistry of the Elements*, 2nd edn. Butterworth-Heinemann, Oxford, 1997.
3. W. Zhao, D. Cortie, L. Chen, Z. Li, Z. Yue, and X. Wang, *Phys. Rev. B*, 2019, 99, p 165133.
4. H. Alam, and S. Ramakrishna, *Nano Enrg.*, 2013, 2, p 190.
5. A. Vora-ud, T. Seetawan, and M. Kumar, *Mater. Sci. Eng. B*, 2019, 250, p 114439.
6. P. Mele, S. Saini, H. Honda, K. Matsumoto, K. Miyazaki, H. Hagino, and A. Ichinose, Effect of substrate on thermoelectric properties of Al-doped ZnO thin films *Appl. Phys. Lett.*, 2013, 102, p 253903.
7. N. Prainetr, A. Vora-ud, S. Thaowonkaew, M. Horprathum, P. Muthitamongkol, and T. Seetawan, *Phys. B*, 2020, 582, p 411977.
8. N. Prainetr, A. Vora-ud, M. Horprathum, P. Muthitamongkol, S. Thaowonkaew, T. Santhaveesuk, T.B. Phan, and T. Seetawan, *J. Electron. Mater.*, 2020, 49, p 572.
9. S. Han, Wearable thermoelectric devices, in *Thermoelectric Thin Films*. P. Mele, D. Narducci, M. Ohta, K. Biswas, J. Morante, S. Saini, and T. Endo Eds., Springer Nature, Cham, 2019.
10. S. Shen, W. Zhu, Y. Deng, H. Zhao, Y. Peng, and C. Wang, *Appl. Surf. Sci.*, 2017, 414, p 197.
11. E.M.F. Vieira, J. Figueira, A.L. Pires, J. Grilo, M.F. Silva, A.M. Pereira, and L.M. Goncalves, *J. Alloys Compd.*, 2019, 774, p 1102.
12. H. Matsushita, E. Hagiwara, and A. Katsui, *J. Mater. Sci.*, 2004, 39, p 6299.
13. R.G. Maier, *Z. Metallkd.*, 1963, 54, p 311.
14. R.M. Marin, G. Brun, and J.C. Tedenac, *J. Mater. Sci.*, 1985, 20, p 730.
15. D.S. Song, J.O. Choi, and S.H. Ahn, *J. Electron. Mater.*, 2016, 45, p 2286.
16. J.J. Xu, H. Li, B.L. Du, X.F. Tang, Q.J. Zhang, and C. Uher, *J. Mater. Chem.*, 2010, 20, p 6138.
17. M. Kumar, A. Vora-ud, T. Seetawan, and J.G. Han, *ACS Appl. Energy Mater.*, 2018, 1, p 4025.
18. M. Kumar, A. Vora-ud, T. Seetawan, and J.G. Han, *Energy Tech.*, 2016, 4, p 375.
19. M. Kumar, A. Vora-ud, T. Seetawan, and J.G. Han, *Mater. Des.*, 2016, 98, p 254.
20. A. Vora-ud, M. Kumar, S. Jin, P. Muthitamongkol, M. Horprathum, S. Thaowonkaew, W. Chao-moo, C. Thanachayanont, P.B. Thang, T. Seetawana, and J.G. Han, *J. Alloys Compd.*, 2018, 760, p 430.
21. B. Lv, S. Hu, W. Li, X. Di, L. Feng, J. Zhang, L. Wu, Y. Cai, B. Li, and Z. Lei, *Int. J. Photoenergy*, 2010, 2010, p 1.
22. N. Somdock, A. Harnwunggmoung, A. Sakulkalavek, and R. Sakdanuphab, *Ceram. Int.*, 2019, 45, p 15860.
23. A. Vora-ud, M. Horprathum, M. Kumar, P. Muthitamongkol, C. Chananonnawathorn, B. Saekow, I. Nualkham, S. Thaowonkaew, C. Thanachayanont, and T. Seetawan, *Mater. Lett.*, 2019, 234, p 229.

# APPENDICE D

## A BRIEF HISTORY OF RESEARCHER

# A BRIEF HISTORY OF RESEARCHER

**PERSONAL DATA:**

| | |
|---|---|
| Name | Somporn Thaowankaew |
| Academic Position | Ph.D. student |
| Date of Birth | September 30, 1991 |
| Place of Birth | Sakon Nakhon, Thailand |
| Nationality | Thai |
| Marital Status | Single |
| Address | |
| 1. Home: | 81 Moo.10, Dong ma fai, Muang, Sakon Nakhon 47000,<br>Thailand<br>Tel. +695-569-3144 |
| 2. Office: | Center of Excellence on Alternative Energy,<br>680/31 Nittayo Road, Sakon Nakhon Rajabhat University,<br>Sakon Nakhon 47000, Thailand<br>Tel. +66-42-744319<br>Fax. +66-42-744319<br>somporn@snru.ac.th |

**EDUCATION:**

| | |
|---|---|
| 2001-2006 | Primary School: Tet-sa-baan 1 Choeng Chum Prachanukul School, Sakon Nakhon, |
| 2005-2010 | Secondary School:1-6, Sakonnakhon Pattanasuksa School, Sakon Nakhon, |

**College:**

| | |
|---|---|
| 2010–2013 | B.S. Major: Physics<br>Sakon Nakhon Rajabhat University, Thailand,<br>Research Title: Synthesis of $Ca_{1-x}Bi_xMnO_3$ (x=0.01–0.03) Compounds by Solid Sate Reaction Method in Ar Atmosphere |

**Graduate Schools:**

| | |
|---|---|
| 2014–2017 | M.S. Major: Physics<br>Sakon Nakhon Rajabhat University, Thailand,<br>Thesis Title: INVESTIGATION ON PHYSICAL PROPERTIES OF $CaCuO_2$ SPUTTERING TARGET FOR FABRICATING THERMOELECTRIC THIN FILM GENERATOR |
| 2018–present | Ph.D Major: Physics<br>Sakon Nakhon Rajabhat University, Thailand,<br>Thesis Title: Thermoelectric Multilayer Generator of Nano Oxide Thermoelectric Materials |